Investigation of doped cuprous halides for photovoltaic and display applications

Thesis submitted for the degree of
Doctor of Philosophy
by

Rajani K. Vijayaraghavan, M.Sc.

School of Electronic Engineering

Dublin City University

Supervised by

Dr. Stephen Daniels

July 2011

Declaration

I hereby certify that this material, which I now submit for assessment on the programme of study leading to the award of Doctor of Philosophy is entirely my own work, that I have exercised reasonable care to ensure that the work is original, and does not to the best of my knowledge breach any law of copyright, and has not been taken from the work of others save and to the extent that such work has been cited and acknowledged within the text of my work.

Signed: ____________

(Candidate) ID No.: ___________ Date: _______

Dedicated to.........

My parents and brothers

Acknowledgements

I owe my heartfelt gratefulness to each and every person whom have made this thesis possible and helped me directly or indirectly throughout my research career. I know it cannot be sufficient to express my thanks to them with words, but I believe they know my mind.

First and the foremost, I would like to express my deepest gratitude to my supervisor Dr. Stephen Daniels and Prof. Patrick. J. McNally for their endless support, guidance, patience, encouragement, care and affection throughout my studies. They have always made themselves available for help whenever I had needed it. The freedom they gave to me to work in my own research interest was really great and enjoyable. Without their blessings, this thesis would have been a distant dream.

My sincere thanks to Dr. Enda McGlynn for allowing me to use the Hall measurement set-up and for the valuable advices and comments during the course of my work.

I would like to thank Dr. Satheesh Krishnamurthy for helping me to carry out the XPS measurements and analysis to make one chapter of this thesis possible.

I am thankful to Billy Roarty for his technical and moral support for the past three years. He was always there to sort out the problems with my cryo-pump and sputtering chamber. I would like to acknowledge Robert, Michael, Liam, Conor Murphy, James and Paul from electronic engineering and Pat and Barry from Physics for their technical help at various stages of my work, on various instruments. Thanks to all staff in electronic Engineering and NCPST.

Thanks to Dr. Francis Lucas and Dr. Lisa O'Reilly for their inputs during the course of my work at DCU. I am grateful to Aidan and Monjarul from the CuX group for their support. Sincere thanks to Jen for the Raman instrument training and for all other helps throughout my stay at DCU. Thanks Chiu, for reading my thesis.

Heartfelt thanks to all my friends in DCU and abroad, without their encouragement and friendship this achievement wouldn't be possible. Thanks to my friends, Jen, Chiu, Ken, Ram, Dave, Jithin, Rajesh , Stuart, Nick, Ameera, Yang, Evgueni, Tomo, Declan, Anita, Karthika, Anitha, Lalit, Chanel, Anila, Suraj, Vinod, Justin, Claudio, Dominik, Remia, Rob, Anthony, Renu and Shija.

Sincere thanks to Dr. R. Ratheesh and Dr. R. Jayaprakash for their constant encouragement and prayers throughout my career. Thanks to Dr. Vladimir for helping me on OES.

I would like to express my deepest gratitude to my flatmates and good friends Bincy and Sithara for their great support and encouragements throughout all difficult situations and for their critical comments and advices. I am indebted to them for making a nice friendly atmosphere at home which was essential for the fulfilment of my work. Thanks to my friends and relatives in India.

Lastly but most importantly, I am thankful to god for giving me my mom, brothers and great dad (late). Their immense love, support and prayer are the key factors for the creation of the positive energy that spread though out my thoughts and my mind, that keeps me always enthusiastic towards research and life.

Abstract

The thesis mainly focuses on the growth and optoelectronic characterisation of the doped cuprous halides (CuX) with high UV/blue emission properties and the light harvesting in the CuBr/Si based heterojunction photovoltaic (PV) cells. Since cuprous halides are short wavelength emitters with high excitonic binding energies, growth of lower resistivity, highly luminescent p and n-type films are essential for the development of the future excitonic based light emitting devices with these materials. We describe the deposition and characterisation of the Zn doped n-type CuCl and oxygen doped p-type CuBr with higher carrier concentration using pulsed dc magnetron sputtering and thermal evaporation followed by oxygen plasma exposure, respectively.

The structural and morphological properties of the n-type Zn doped CuCl films are investigated using XRD, SEM and AFM measurements. Our findings show that, the crystallinity of CuCl increases with doping of Zn and the maximum is obtained for the 3 % doped film, beyond which crystallinity decreases. The Zn doping has no deleterious impact on the structural and luminescent properties of CuCl up to a doping percentage of 5. An order of magnitude reduction in the resistivity of the CuCl films is obtained as a result of Zn doping. The resistivity, n-type carrier concentration and carrier mobility corresponding to the 3 % Zn doped films were, respectively 6 Ωcm, ~ 9.8×10^{18} cm^{-3} and 0.1 $cm^2V^{-1}s^{-1}$.

The influence of Zn doping on the electronic structure of CuCl is investigated using photoemission spectroscopic studies. Our studies on the Cu and Cl core level spectra show the presence of trace amounts of Cu^{2+} species in the undoped CuCl sample along with the major Cu^{+} species. This is verified by the observation of the satellite and shoulder peaks in the Cu 2*p* core level and a higher binding energy tail in the Cl 2*p* core level spectra. The disappearance of the cupric species with doping of Zn (3 %) is also observed. Furthermore, the shifting of the valence band towards the higher binding energy confirms the filling of the conduction band owing to the Zn doping, which explains the improvement of the conductivity of the doped films.

We have successfully deposited p-type CuBr films by doping of oxygen. Our findings show that, there is no significant influence on the structural properties of the CuBr up to an oxygen plasma exposure time of 5 min. The investigation of the optical properties confirms good luminescence of the CuBr films up to a plasma exposure time of 3 min. The electrical characterisations of the oxygen plasma exposed films reveal that, oxygen act as a good acceptor for CuBr. The resistivity of the 3 min oxygen plasma exposed samples reduces to the order of ~ 1 Ωcm. SIMS analysis shows that, the diffusion of oxygen is quite good in the CuBr films.

The realization of the heterojunction PV cell based on p-CuBr/n-Si is investigated. The I-V characteristics confirm the rectification behaviour of the p-n diode with a turn on voltage of ~ 1 V. The photoresponse properties of the heterojunction are studied by measuring the I-V characteristics under illumination. The photogenerated carrier formation is confirmed by the increased reverse current under illumination of the heterojunction. The wavelength dependence of the photo current was also studied using LED illumination.

Development of ultrathin transparent Cr contacts, useful for the electroluminescent device fabrication was also discussed. This can be used as an alternative to well-known Indium Tin Oxide films for the future fabrication of the CuX-based display devices.

Table of contents

Declaration..ii

Acknowledgements...iv

Abstract.. vi

Table of contents..viii

List of tables and figures...xii

Abbreviations..xix

List of publications... xx

1. Introduction

1.1 Short wavelength optoelectronics..1

1.2 p-n junctions for optoelectronics..2

1.3 Photovoltaic (PV) applications of p-n junctions..........................3

1.4 Short wavelength emitting materials...4

1.5 Introduction of cuprous halides in to UV- optoelectronics..........6

1.6 Electronic structure and optical properties of CuX.....................9

1.7 Conductivity of CuX...12

1.8 Thesis scientific questions...13

1.9 Thesis overview...14

2. Processing and characterisation techniques

2.1 Introduction..17

2.2 Film deposition methods...17

2.2.1 Sputtering...17

2.2.2 Pulsed dc magnetron sputtering......................................20

2.2.3 Vacuum Evaporation..24

2.3 Characterisation techniques...25

2.3.1 X- Ray diffraction analysis...25

2.3.2 Scanning Electron Microscopy……………………........27

2.3.3 Energy Dispersive X-ray analysis……………………........30

2.3.4 Photoluminescence...30

2.3.5 UV –Vis Absorption spectroscopy.................................32

2.3.6 Atomic force microscopy……………………………....33

2.3.7 Four-point probe technique: Resistivity……………….....35

2.3.8 Hall Effect experiment…………………………………...37

2.3.9 X-ray Photoelectron Spectroscopy (XPS)……………........40

2.3.10 Secondary ion mass spectroscopy (SIMS)………………43

3. Growth and characterization of n-type CuCl

3.1 Introduction..45

3.2 Experimental methods..46

3.3 Results and discussion..48

3.3.1 Pulsed dc magnetron sputtered CuCl...............................48

3.3.2 Structure and morphology of undoped and doped CuCl....52

3.3.3 Optical characteristics of doped films..............................59

3.3.4 Electrical properties of doped films..................................63

3.4 Summary..67

4. Photoemission spectroscopic study of Zn doped n-type CuCl.

4.1 Introduction……………………………………………………………68

4.2 Experimental details…………………………………………...70

4.3 Results and discussion. ………………………………………..71

4.3.1 Effect of Zn doping- An overview………………………..71

4.3.2 Zn *2p* core level spectra in the doped films………………71

4.3.3 Effect of Zn doping on the Cu *2p* core level spectra……..73

4.3.4 Effect of Zn doping on the Cl *2p* core level spectra……...76

4.3.5 Influence of Zn doping on the valence band of CuCl…….78

4.4 Summary...80

5. Growth and characterisation of p-type CuBr

5.1 Introduction..81

5.2 Experimental details...82

5.3 Results and discussion..84

5.3.1 Structural and morphological properties...............................84

5.3.2 Oxygen diffusion studies of the films using SIMS.............91

5.3.3 Optical properties...95

5.3.4 Electrical Properties...99

5.4 Summary...103

6. CuBr/Si heterojunction for photovoltaic applications

6.1 Introduction..104

6.2 Experimental methods..105

6.3 Theory of heterojunction diode and photovoltaic cells..................106

6.4 Results and discussion...115

6.4.1 I-V characteristics of the CuBr/Si heterojunction..............115

6.4.2 I-V characteristics under illumination..............................120

6.4.3 Stability of the device...126

6.5 Summary...127

7. Development of ultra thin chromium transparent contacts

7.1 Introduction...128

7.2 Experimental details...129

7.3 Results and discussion...131

7.3.1 Variation of resistivity with thickness..............................131

7.3.2 Variation of transmittance with thickness.........................134

7.3.3 Effect of target power on resistivity.................................137

7.3.4 Influence of pulse duty cycle on resistivity.......................139

7.4 Summary...141

8. Conclusions and future works

8.1 Conclusions...142

8.2 Future directions...145

References...147

List of tables and figures

Tables

1.1 Important features of CuX for the suitability of the short-Wavelength applications. 7

3.1 Sputtering process conditions used for the deposition of the undoped and Zn-doped CuCl films. The substrates used were Si and glass slides. 52

3.2 ICDD powder diffraction data for CuCl. Intensities of different peaks are shown here corresponding to the values of their 2θ and (hkl) parameters. 54

5.1 Values of the Plasma parameters used for the oxygen doping of the CuBr films. 84

5.2 Powder diffraction data file for CuBr according to the JCPDS card number 06-0292. 86

Figures

1.1 Band gap of various optoelectronic semiconductors plotted against lattice constant. The positions of CuCl and CuBr are marked in the figure. 5

1.2 Zinc blende structure of γ- CuX. 8

1.3 Schematic of the development of valence states due to *s*, *p* and *d* electrons at the Brillouin Zone centre Γ in the cubic crystal field of the Zinc blende structure (not to scale). The numbers in the brackets give the degeneracy of the corresponding states. 10

1.4 (a) Schematic of the CuX- based electroluminescent device structure using stacked layers of transparent electrode coated on glass, n-type CuX, p-type CuX and a top metal contact. The top and bottom electrodes will be connected to the battery. (b) Schematic of the PV cell structure using CuX. The various layers consist of a bottom electrode, p or n- absorbing semiconductor layer followed by p or n- CuX layer and then a top contact, with top and bottom contacts connected to a battery. The device will be illuminated from the top. 15

2.1 Schematic of the magnetron cathode and the sputtering deposition process. 19

2.2 Photograph of the sputtering system used for the experiment: A-magnetron, B- sputtering chamber, C- Loading chamber and D- Transfer valve. 21

2.3 Photograph of the asymmetric bipolar pulsed power supply (ENI RPG-100) used for the deposition. 22

2.4 Schematic of the asymmetric bipolar pulse dc signal used for the deposition. Sputtering of the target and the deposition on the substrates take place during the pulse on time of the pulse. 23

2.5 Schematic diagram of the vacuum evaporator system. The bell jar is pumped down to ~10^{-6} mbar using the vacuum pump. 25

2.6 Photograph of Bruker AXS Advance D8 XRD system. 26

2.7 Illustration of the Bragg's law. The figure indicates the conditions for the occurrence of Bragg's diffraction. Planes of atoms are indicated using the black soild lines. 26

2.8 Photograph of the Zeiss EVO LS-15 SEM system. 28

2.9 Schematic of the SEM system. The electron gun and the lensing system to focus the electron beam on to the sample surface are illustrated. 28

2.10 Illustratioin of the different signals generated by the electron beam-specimen interaction in SEM and the regions from which the signals can be detected. 29

2.11 Schematic of the PL experimental set-up. 31

2.12 Photograph of the Perkin Elmer Lambda 40 UV-VIS spectrometer. 32

2.13 Image of the AFM scanning set-up. 34

2.14 Schematic of the AFM measurement set-up. 34

2.15 (a) Photograph of the Four point probe measurement setup and (b) schematic of the collinear four point probe. 35

2.16 Visualisation of the Hall effect measurement setup. 39

2.17 Photograph of the HL 5500 PC Hall measurement set-up. 40

2.18 (a) Schematic diagram of the photoemission process, which shows the photo ionization of an atom by the ejection of a 1s electron, (b) demonstration of the formation of the photoemission spectrum. 42

2.19 Schematic of the SIMS analysis. 44

3.1 A typical EDX spectrum of a CuCl film deposited at a target Substrate separation of 6 cm, with a sputtering pressure and power density of 5×10^{-3} mbar and 1.73 W/cm^2 respectively. The accelerating voltage used in the EDX analysis was 13 kV. 50

3.2 XRD spectrum and AFM image of a typical CuCl film deposited using optimized conditions of power (40 W), pressure (5.5x10^{-3} mb), target substrate distance (6 cm) and pulse duty cycle (40 %). 51

3.3 Schematic of the expected CuCl lattice after Zn doping. Zn substitute Cu, and donate an extra electron in to the lattice to make it n-type. 52

3.4 X-Ray powder diffraction pattern for (a) 0 %, (b) 1 %, (c) 5 % and (d) 3 % Zn doped CuCl films deposited on Si (100) substrate. The patterns were recorded under identical conditions. 54

3.5 Variation of (111) peak intensity to the total intensity of all orientations as a function of the % of Zn in the film. This plot is according to the XRD data in the fig.3.4 55

3.6 Variation of FWHM of CuCl (111) peak and average crystal size of the CuCl: Zn film as a function of the percentage of Zn in the film. The crystal sizes were calculated using Scherrer equation. 56

3.7 SEM images of CuCl: Zn films with (a) 0 %, (b) 1 %, (c) 3 %, and (d) 5 % Zn in the film. All the films were deposited on Si substrate, and images were taken under identical conditions using 13 kV accelerating voltage. 58

3.8 EDX spectrum of a typical 3 % Zn doped CuCl film deposited on Si substrate. The accelerating voltage used for the EDX analysis was 13 kV. 59

3.9 Room temperature UV-Vis absorption spectra of (a) 3 % Zn doped CuCl and (b) undoped CuCl deposited on glass substrates. 60

3.10 PL spectrum of a typical 3 % Zn doped film at 80 K. The film was deposited on Si (100) substrate. 61

3.11 Temperature dependant PL spectrum of a typical 3 % Zn doped CuCl films deposited on Si (100) substrate. 62

3.12 Room temperature PL of the typical 3 % Zn doped CuCl sample. 63

3.13 Variation of carrier concentration and mobility as a function of the % of Zn in the target measured using Hall measurement set-up. Films deposited on glass substrates with gold electrodes on top of it were used for the measurements. 64

3.14 Variation of the resistivity of the CuCl:Zn films as a function of the % of Zn in the film. 67

4.1 Zn *2p* core level spectra of the CuCl as a function of the Zn doping. The peak around 1022 eV represents Zn $2p_{3/2}$ and that around 1045 eV represents Zn $2p_{1/2}$. 73

4.2 Cu *2p* core level spectra of the undoped and 1- 5 % Zn doped CuCl films. Cu $2p_{3/2}$ (A_1), Cu $2p_{1/2}$ (A_2), shoulder (B_1 and B_2) and the satellite spectral lines (C) are illustrated here. 75

4.3 The variation of the full width half maximum of the Cu $2p_{3/2}$ line as a function of the percentage of Zn in the film. 75

4.4 Cl 2*p* spectra of the undoped CuCl and the 1, 3 and 5 % Zn doped samples. The lower binding energy peak corresponds to the $2p_{3/2}$ line and the higher binding energy one corresponds to the $2p_{1/2}$ spectral line. 78

4.5 Valence band spectra of CuCl as a function of the percentage of Zn doping. The zero binding energy point correspond to the Fermi energy, E_f. 80

5.1 XRD pattern of the as-deposited and the 1 min, 3 min and 5 min oxygen plasma treated CuBr films deposied on Si (100) substrates. All the scans were performed under the same experimental conditions. 86

5.2 Variation of FWHM of (111) peak and crystal size as a function of the oxygen plasma exposure time. The crystal sizes were calculated using Scherrer equation. 87

5.3 SEM image of the as deposited CuBr film on Si substrate. An accelerating voltage of 13 kV was used for the imaging. 89

5.4 SEM image of the 5 min oxygen plasma treated CuBr film deposited on Si (100) substrate. 90

5.5 AFM image of the (a) as deposited and (b) 5 min oxygen plasma exposed films deposited on Si (100) substrate. The imaging was performed under the identical conditions and the size of the image in both cases is equal to 0.71 μm×0.71μm. 90

5.6 EDX spectrum of a typical as-deposited CuBr film on Si substrate. The experiment was carried out at an accelerating voltage of 13 kV. 91

5.7 SIMS depth profile of the as-deposited CuBr film deposited on Si substrate. 93

5.8 SIMS depth profile of the 1 min oxygen plasma exposed CuBr film deposited on Si substrate. 93

5.9 SIMS depth profile of the 5 min oxygen plasma exposed CuBr film deposited on Si substrate. 94

5.10 Variation of the oxygen count rate at two different depth ~37 nm, ~ 75 nm and ~150 nm as a function of the oxygen plasma exposure time. This graph is plotted using the SIMS depth profile data of different samples. 95

5.11 Absorption spectra of the as deposited and the 1 min, 3 min and 5 min oxygen plasma exposed CuBr samples deposited on glass substrate taken under identical conditions. 96

5.12 UV-Vis transmittance spectra of the as-deposited and oxygen plasma exposed CuBr films for 1 min and 5 min deposited on glass substrate. The spectra were recorded under identical experimental conditions. 97

5.13 Room temperature PL of as-deposited and 1 min and 5 min oxygen plasma exposed CuBr films. 99

5.14 Variation of Carrier concentration and carrier mobility as a function of the time of oxygen plasma exposure. 101

5.15 Resistivity of the CuBr film as a function of the time of oxygen exposure. 103

6.1 Schematic of the (a) p-n junction, energy band diagram (b) without an applied voltage and (c) with an applied voltage of V across the junction. 109

6.2 Schematic of an ideal PV cell equivalent circuit. A constant current source is connected in parallel with the junction. The current source I_L results from the excitation of excess carriers by illumination, I_s is the diode saturation current and R_L is the load resistance. 111

6.3 Demonstration of J-V characteristics of a PV cell under illumination. (V_m, I_m) is the maximum power point. V_{oc} and J_{sc} are the open circuit voltage and the short circuit 113

current respectively.

6.4 Solar energy distribution corresponding to AM 1.5 illumination. Intensity profile of sunlight at the surface of the earth. 114

6.5 Schematic of an energy band diagram of a p-n heterojunction. 115

6.6 (a) Schematic of the structure of the P-CuBr/N-Si heterojunction device, (b) photograph of the top view of the device. The yellow dots are the circular gold electrode on the top of the device. 117

6.7 Photograph of the probe station used for the I-V measurements. 117

6.8 I-V characteristics measured between two gold contacts on p-CuBr. 118

6.9 I-V characteristics of the p-CuBr / N-Si heterojunction. 119

6.10 Schematic of the band diagram of the p- CuBr/n-Si heterojunction diode at (a) thermal equilibrium and (b) under forward bias. 121

6.11 (a) Photograph and (b) Transmittance spectra of a typical p- CuBr film deposited on glass substrate. Both the figures confirm the high transparency of the film in the major part of the visible spectrum. 121

6.12 I-V characteristics of the CuBr/Si heterojunction measured Under dark and illumination conditions (incandescent bulb). The device structure used is Au/p- CuBr/n-Si/Al. 123

6.13 Absorption coefficient of pure Si [160] and absorbance of CuBr on glass substrate (inset) at 300 K. 124

6.14 (a) Spectral response from the blue and red LEDs. The plots show spectral width of above 20 nm for both LEDs. (b) Illumination effect due to red and blue LEDs on the I-V characteristics of the heterojunction plotted with the dark curve. 126

6.15 The efficiency calculation of the CuBr/Si PV cell using 85 mW/cm^2 illumination. The maximum power point, J_{sc}, V_{oc} and FF are indicated in the figure. 127

6.16 Effect of illumination time on the I-V characteristics of the heterojunction device. The slight changes in the short circuit current as a function of the illumination time are shown in the inset. 129

6.17 Influence of the aging on the I-V characteristics of the heterojunction. 130

7.1 Variation of resistivity of Cr- films as a function of thickness. All the films were deposited under identical experimental conditions (target power = 100 W and pulse duty cycle = 10%). 135

7.2 Optical transmittance plotted against wavelength for Cr films of various thicknesses. The measurements were performed under identical conditions. 137

7.3 (a) The variation of average transmittance of the Cr films as a function of thickness measured under identical conditions, (b) Photograph of ultrathin Cr film deposited on glass substrate (thickness=2.8 nm). 138

7.4 Variation of average transmittance plotted against resistivity of the films. The corresponding thicknesses are also indicated in the figure. 139

7.5 AFM image of a typical chromium film of thickness 5 nm (maximum z- height is 3.5 nm). 140

7.6 Variation of resistivity of the Cr film as a function of target power used for deposition. All experiments were carried out at identical conditions. (duty cycle = 10% and pulse frequency = 100 KHz). 141

7.7 The variation of the resistivity of the film as a function of pulse duty cycle used for deposition. All experiments were performed at a target power of 100 W and a pulse frequency of 100 KHz. 143

List of Abbreviations

AFM	Atomic force microscopy
CuX	Cuprous halides
CuCl	Cuprous chloride
CuBr	Cuprous bromide
EDX	energy dispersive X-ray spectroscopy
LED	Light emitting diode
ITO	Indium tin oxide
PL	Photoluminescence
PV	Photovoltaics
SEM	Scanning electron microscopy
SIMS	Secondary ion mass spectroscopy
UV-Vis	Ultraviolet-Visible
XRD	X-ray diffraction
XPS	X-ray photoelectron spectroscopy
V_{oc}	Open circuit voltage
I_{sc}	Short circuit current
FF	Fill factor

List of publications

1. "Growth of n-type γ-CuCl with improved carrier concentration by pulsed DC sputtering: Structural, electronic and UV emission properties"
   K.V. Rajani, F. Olabanji Lucas, S. Daniels, D. Danieluk, A. L. Bradley, A. Cowley, M. M. Alam, P. J. McNally
   Thin Solid Films 519 (2011) 6064–6068
2. "Ultrathin chromium transparent metal contacts by pulsed dc magnetron sputtering"
   K. V. Rajani, S. Daniels, P. J. McNally, F. Olabanji Lucas and M. M. Alam
   *Phys. Status Solidi A **207**, 1586 (2010)*
3. Zn Doped Nanocrystalline CuCl Thin Films for Optoelctronic Applications
   K. V. Rajani, F. Olabanji Lucas, M. M. Alam, S. Daniels and P. J. McNally
   *Mater. Res. Soc. Symp. Proc., **1260**, 1260-T10-07 (2010)*
4. "Hybrid organic–inorganic spin-on-glass CuCl films for optoelectronic applications"
   M M Alam, F. O. Lucas, D. Danieluk, A. L. Bradley, **K. V. Rajani**, S. Daniels and P. J. McNally
   J. Phys. D: Appl. Phys., ***42,*** *225307 (2009).*
5. "Synthesis and characterisation of copper (I) chloride nanocrystalas in conductive polymer for UV light emitters"
   M. M. Alam, F. O. Lucas, A. Cowley, K. Crowley, S. Daniels, **K. V. Rajani** and P. J. McNally
   Mater. Res. Soc. Symp. Proc., *2010*
6. "Evaluation of conduction mechanisms and electronic parameters for Au/organic-inorganic CuCl hybrid film/ITO structures"
   M. M. Alam, A. Cowley, **K. V. Rajani**, S. Daniels and P. J. McNally
   Semicond. Sci. Tech. (under review)
7. "Cuprous oxide thin films grown by oxygen plasma exposure of Cu layers: structural and optoelectronic properties"
   K. V. Rajani, S. Daniels, E. McGlynn, P. J. McNally
   Manuscript under preparation

8. “Electronic structure of Zn doped copper chloride probed by soft x-ray spectroscopies”
   K.V. Rajani, S. Daniels, P. J. McNally and S. Krishnamurthy
   Manuscript under preparation
9. “Growth of p-type CuBr: Realization of p-CuBr/n-Si heterojunction diode”
   K.V. Rajani, S. Daniels and P. J. McNally
   Manuscript under preparation
10. Light harvesting in CuBr/Si heterojunction: CuBr based solar cells
   K.V. Rajani, S. Daniels and P. J. McNally
   Manuscript under preparation

Conference Presentations

1. “Zn Doped Nanocrystalline CuCl Thin Films for Optoelectronic Applications”
   K. V. Rajani, F. O. Lucas, S. Daniels and P. J. McNally
   Material research Society (MRS) Symposium, 2010, San Francisco, CA, USA.
2. “Ultra Thin Chromium Transparent Metal Contacts by Pulsed DC Magnetron Sputtering”
   K.V. Rajani, S. Daniels, P. J. McNally, F. O. Lucas, M. M. Alam
   European Materials Research Society (EMRS), 2009, Strasbourg, France
3. “Transparent Electrodes for Optoelectronics Industry based on Ultrathin Chromium Films”
   K.V. Rajani, S. Daniels, F. O. Lucas, M. M. Alam, P. J. McNally
   Photonics Ireland, 2009, Cork, Ireland
4. “Synthesis, Structural and optical properties of γ-CuCl hyrid films”
   M. M. Alam, O. F. Lucas, S. Daniels**, K.V. Rajani** and P. J. McNally
   European Materials Research Society (EMRS), 2009, Strasbourg, France
5. “Hybrid Organic–Inorganic Spin-on- Glass CuCl Films for Optoelectronic Applications”
   M. M. Alam, F. O. Lucas, **K.V. Rajani**, D. Danieluk, A. L. Bradley, Barry Foy, S. Daniels, P. J. McNally
   Photonics Ireland 2009, Cork, Ireland.

Chapter 1

Introduction

1.1 Short wavelength optoelectronics

Optoelectronics is one of the most exhilarating and active industries of the information age. As a strategic enabling technology, it has a lot of applications in our daily lives. Among the optoelectronic materials, short wavelength (wide band gap) emitting materials are well known for their potential commercial applications for displays, energy efficient lighting, solar cells, biomedical research, sterilization, printing, optical storage and communications. Full-colour displays require the use of the aforementioned materials to produce visible colours. Furthermore, short wavelength emitters are important for the manufacturing of efficient white light emitting devices with the advantages of improved life span and less power consumption in comparison with conventional incandescent and fluorescent lamps.

The storage density of an optical memory device is inversely proportional to the square of the laser wavelength. Thus, the shorter the wavelength of the laser diodes used for reading and writing the information, the higher the capacity of the optical data storage media e.g. magneto-optical disks and DVDs [1]. Hence, a 4-8 fold increase in storage capacity could be realized with short wavelength lasers in comparison with relatively longer ones.

Moreover, wide band gap materials perform an important role in contemporary photovoltaic (PV) research. Heterojunctions based on these material compounds present great potential in the modern photovoltaic technology.

1.2 p-n junctions for optoelectronics

p-n junctions can be considered as the basic building blocks of most semiconductor devices, such as LEDs, transistors, diodes and solar cells. The p-n junction theory acts as the basis of semiconductor device physics. They can be normally classified in to two families, homojunctions and heterojunctions. A p-n homojunction is formed by introducing different dopants in the same semiconductor while a p-n heterojunction can be considered as a junction formed between two dissimilar semiconductors. Initially, the development of solid state electronics was mainly associated with the use of homo p-n junctions, which has been based on the controlled inclusion of different impurities in to the semiconductor crystal. More recently, the realization of single crystal heterojunctions was facilitated by the progress in the epitaxial growth of semiconductors [2]. The advances in the heterojunctions enabled a substantial improvement in the major parameters of most of the semiconductor devices.

However, the inherent drawback associated with the homojunction over heterojunction is about the fact that, there are many materials (most of the materials with energy gap greater than 2.5 eV) that can only be doped either p-type or n-type. This is one of the reasons for the difficulty in the fabrication of blue emitting LEDs using the homojunction of these materials, apart from the GaN one.

Heterojunctions have been widely used for a variety of device applications and can be considered as the key building blocks of photonics devices. Visualization of this type of structure was first made by Preston [3]. A variety of models have been proposed by researchers in order to explain current conduction in heterojunctions. Later, the use of a heterojunction as a wide-gap emitter to increase the injection efficiency of transistors was proposed by Kroemer [4]. It is well known that the most

serious problem associated with the fabrication of useful heterojunctions is the presence of interfacial defects arising due to lattice parameter mismatch between the semiconductors [5]. Two materials having similar lattice constants with different band gaps can be considered as a good combination for heterojunction devices. However, a model for the ideal heterojunctions, which neglects interfacial defect states, was proposed by Anderson in 1960, by analysing the Ge-GaAs heterojunctions [6]. This model is used as the basic model for heterojunction analysis.

1.3 Photovoltaic (PV) applications of p-n junctions

PV represents one of the most promising methods of energy production without contributing much towards global warming and environmental pollution. The most important example of a homojunction PV cell is based on crystalline silicon, in which one side is dominated by positive holes (p-type) and the other side by negative electrons (n-type). The position of the p-n junction is adjusted to maximise light absorption close to it, in order to minimize the recombination possibilities. Light illumination causes the production of free carriers in Si, which diffuse to the p-n junction and separate, leading to the formation of a current, provided the quality of Si used is adequate. The innate problem associated with the formation of homojunctions is that, several PV materials are impossible to dope to both p and n-type, but instead to only one type. Moreover, there is a possibility for interface recombination at metal contacts in the case of homojunctions [7].

Normally, the top and bottom layers of the heterojunction PV cell structure have different purposes. The top layer (window layer) is usually a higher band gap material, which allows the passage of light through it towards the bottom layer made

up of lower band gap material that rapidly absorbs light. The light illumination produces free carriers (electrons and holes) close to the junction, which can help the effective separation of the carriers before recombination happens. It was reported by Sreedhar *et al.* that, relatively higher carrier generation near and in the depletion region is possible in an abrupt heterojunction than that in the homojunction [8].

Thin films Photovoltaics is a fascinating technology owing to the light weight and flexible fabrication, which allows the construction of the arrays onto non-rigid or uniform structures for novel power systems. It consumes considerably less material and has the benefit of large area and economical manufacturing [9-11]. One of the first thin film solar cells, which was developed for space applications was the Cu_2S/CdS cell [7].

1.4 Short wavelength emitting materials

Group III nitride materials are one of the most promising candidates for short wavelength applications [12-15]. The III–V nitrides such as aluminium nitride (AlN), gallium nitride (GaN) and indium nitride (InN), are candidate materials for optoelectrical applications at these short wavelengths, because they form a continuous alloy system (InGaN, InAlN, and AlGaN) whose direct optical bandgaps for the hexagonal wurtzite phase range from 1.9 eV for InN and 3.4 eV for GaN to 6.2 eV for AlN [16]. Ultraviolet laser diodes and LEDs with GaN, AlGaN or AlGaInN active layers can provide light emission at a wavelength shorter than 365 nm corresponding to the GaN band gap of 3.4 eV [17]. These III-V nitrides are wide direct band gap materials with high thermal conductivity and chemical stability. The bandgap energy of AlInGaN varies depending on its composition, at room

temperature. Therefore, III–V nitride semiconductors are particularly useful for light-emitting devices in the short wavelength region [18-20].

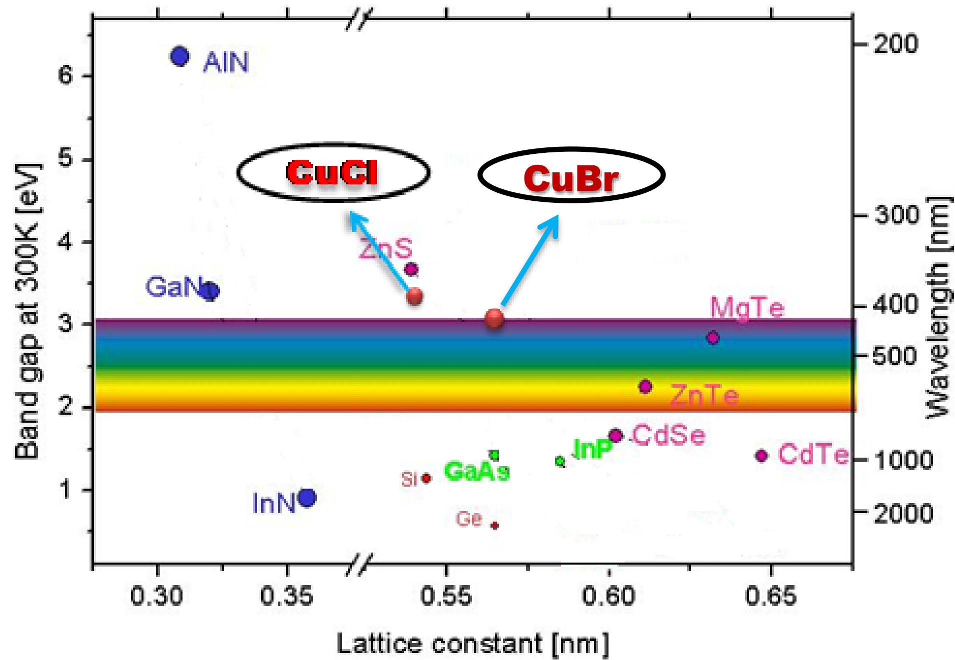

Fig. 1.1**:** Band gap of various optoelectronic semiconductors plotted against lattice constant. The positions of CuCl and CuBr are marked in the figure.

The first report on GaN LED was in 1971 by Pankove *et al.* [21], and the first GaN pn junction LED was demonstrated by Akasaki *et al.* in 1989 [22]. Diode lasers emitting radiation of wavelength shorter than 500 nm were initiated by Nakamura *et al.* in 1996, by the introduction of the first blue emitting InGaN/GaN diode lasers based on III-V semiconductors. A. Kuramata *et al.* have reported on the application of GaN based blue laser diodes for optical data storage applications [1].

Due to the intricacy of growing on to single wafers, GaN and its alloys are typically grown on suitable substrates like Al_2O_3 and SiC. But the crucial problem

associated with this is the lattice mismatch between the epilayers and the substrate. In the case of GaN/Al_2O_3 structures, the lattice mismatch is 13.6%, this can yield dislocation densities as high as 10^{10} cm^{-2}, which is detrimental to the performance of light emitting devices [23]. The lattice mismatch of GaN with Si substrate is nearly 17%. Efforts to reduce the dislocation densities led to the introduction of epitaxial lateral overgrowth techniques (ELOG), that can reduce the dislocation densities by orders of magnitude compared to the conventional MOCVD (metal organic chemical vapour deposition) techniques on SiC and Al_2O_3 substrates [24, 25]. The exciton binding energy of GaN is nearly 25 meV [26].

Another material extensively used in the short wavelength optoelectronic industry is ZnO, which is a II-VI, wurtzite, direct band gap semiconductor material with a band gap of 3.37 eV. It has significant advantages including large exciton binding energy (60 meV), as demonstrated by efficient excitonic lasing on optical excitation [27, 28]. However, the choice of dopant and growth technique remains controversial and the reliability of p-type ZnO is still under debate [29], due to the strong self compensation effect arising from the presence of native defects or hydrogen impurities [30, 31]. The lattice mismatch of ZnO with Si substrates is approximately 18 %.

1.5 Introduction of cuprous halides (CuX, X=Cl,Br) in to UV- optoelectronics

Cuprous halides are wide band gap (CuCl ~3.4 eV and CuBr ~3.1 eV) compound semiconductors (I-VII) with a zinc blende structure at room temperature [32]. The lattice constants of CuCl and CuBr are 5.42 Å and 5.69 Å, respectively [33]. They undergo a phase transition from gamma phase (Zinc blende) to beta phase (Wurtzite)

at higher temperatures before the melting point [34, 35]. The Zinc blende structure consists of two interpenetrating FCC sublattices occupied by Cu^+ and Cl^- ions respectively, and shifted relatively to each other by ¼ of the space diagonal. Some of the important features of CuX are illustrated in table 1.1. The lattice-mismatch between the CuX and Si substrate, which is a model platform for optoelectronic device fabrication, is relatively low (especially for CuCl), compared to that of the other established short wavelength candidates (GaN and ZnO). The interfacial defects resulting from this lattice parameter mismatch between the semiconductors are considered as one of the major issues associated with many of the existing materials. Furthermore, the excitonic binding energies of CuX are very high compared to GaN and ZnO, which again underlines the necessity of the exploration of this material as a future optoelectronic candidate. Even if CuX exhibit higher excitonic stability, they are very sensitive to moist air. Prolonged exposure of these materials to moist air causes the formation of oxyhalides [36]. But this issue can be solved by the use of suitable capping layers like cyclo olyfin co polymer (COC) and polysilsesquioxane (PSSQ) [37]. Again, it is well known that the stability sequence of halide complexes of Cu^+ is of the order I >Br>Cl>F [38].

Table 1.1: Important features of CuX for the suitability of the short-wavelength applications.

Material	Lattice constant	Lattice mismatch with Si (%)	Excitonic binding Enegy (meV)	γ-phase up to temperature (K)
CuCl	5.42	0.5	190	680
CuBr	5.69	4.6	108	664

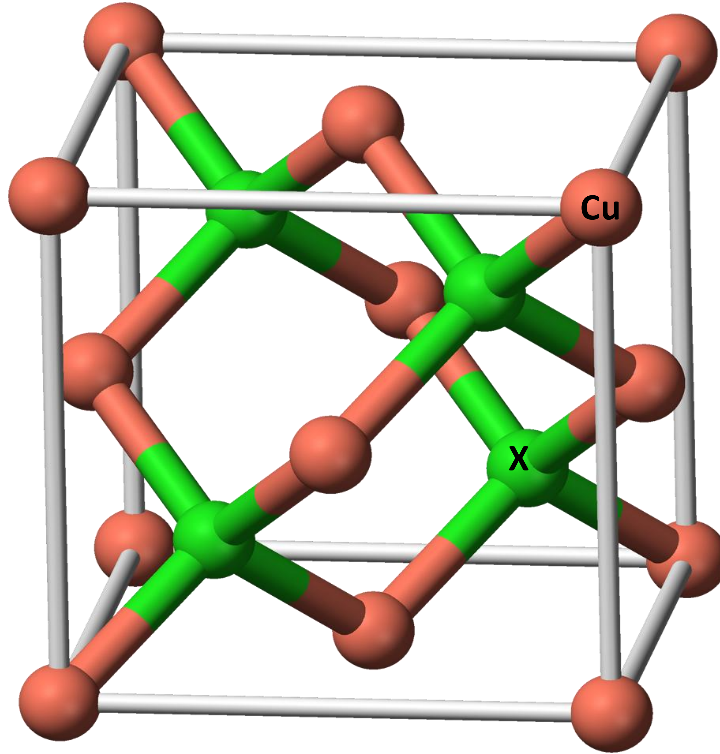

Fig. 1.2**:** Zinc blende structure of γ- CuX [40].

Hence, CuBr is expected to be more stable than CuCl [39]. It is a matter of great interest to explore the utility of these halides in the optoelectronic and photovoltaic device applications. Since these materials have very high excitonic binding energies, and the excitonic luminescence is the extremely efficient emission mechanism in solids, the research towards the application of these materials for the development of LEDs and laser diodes (LDs) is particularly important.

There have been numerous reports on growth techniques for CuCl starting from the early work in the 1960s. The heteroepitaxial growth of CuCl and CuBr on (001) surfaces of MgO with rock-salt structure has been studied by Yanase *et al*. [41]. Thin

film deposition of CuX on different substrates using RF sputtering has also been reported [42, 43]. Study of the heteroepitaxial growth kinetics has been published in the case of the molecular beam epitaxial growth of CuCl on CaF_2 (111) using AFM [44]. There are reports on the growth of polycrystalline CuCl thin films by vacuum evaporation as well [45]. Takami *et al.* reported the development of CuCl microcrystals doped SiO_2 glass by the co-sputtering of CuCl and SiO_2 [46]. Moreover, CuX nanoparticle-dispersed glasses were prepared by means of a conventional copper staining by Kadono *et al.* [47]. CuCl micro crystals were fabricated using RF magnetron sputtering with a composite target embedded with CuCl pellets [48, 49].

1.6 Electronic structure and optical properties of CuX

The electronic band structure of CuX has been of interest to several researchers and there are numerous reports on the experimental and theoretical investigation of the same [50-52]. The first report on the energy band calculation of I-VII semiconductors was made by Song using the tight binding method [52]. He concluded that the upper five valence bands were mainly *d*-like. Later, Khan calculated the conduction band of CuCl based on Song's work [53]. Afterwards, photoemission experiments were carried out to identify the positioning of the *d*-levels [54, 55] and to derive approximate partial *p* and *d* densities of states curves in the valence band region [56].

The outer electronic configuration of the isolated metal and the halogen atoms in CuX are respectively $d^{10}s^1$ and s^2p^5. During the compound formation, the copper ion and halogen ion would have a completely filled outer *d* shell and a rare gas configuration respectively, due to the transference of the loosely bound metal *s*

electron towards the more electro-negative halogen atom [56]. Unlike other zincblende type semiconductors, the energies of the metal 3*d* levels are close to the halogen *p*- levels in CuX, hence strong *p*-*d* hybridization occurs, which can alter its physical properties [57]. This hybridization is responsible for the small spin orbit splitting at the top of the valence band (Γ_{15}), which is negative in the case of CuCl [35, 58]. Hence, the highest Γ_{15} valence state is only two fold degenerate (Γ_7) while the second highest state is four fold degenerate (Γ_8) [59] (Schematic shown in figure 1.3).

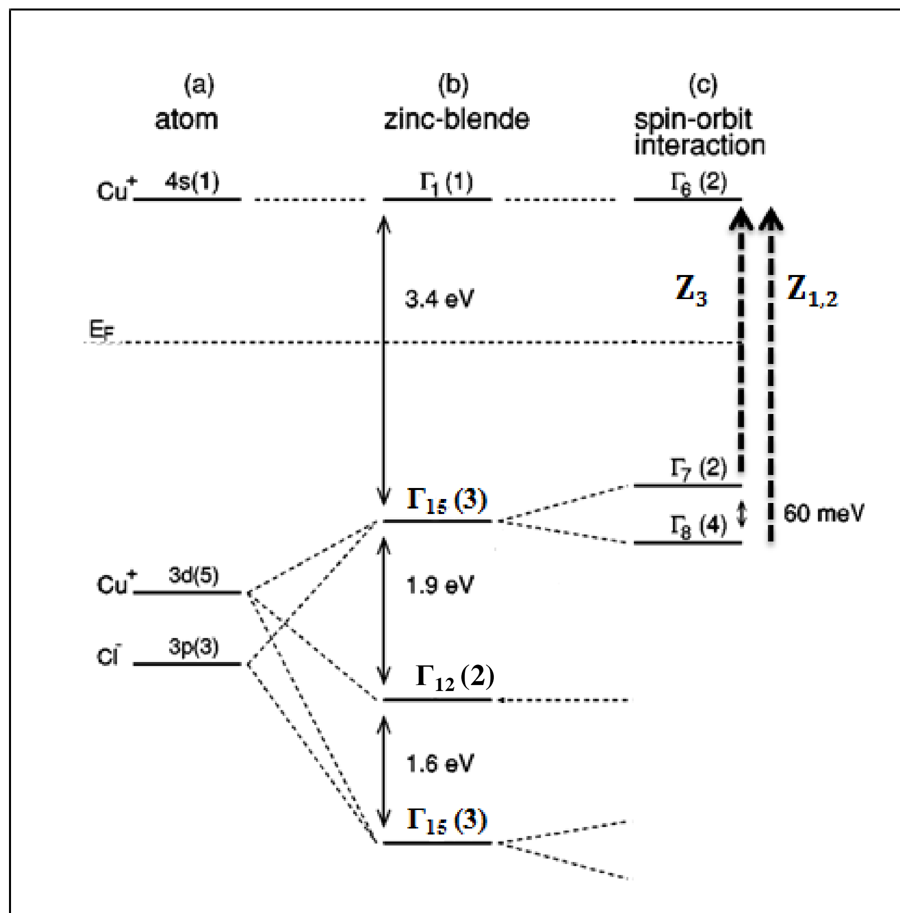

Fig. 1.3: Schematic of the development of valence states due to *s*, *p* and *d* electrons at the Brillouin Zone centre Γ in the cubic crystal field of the Zinc blende structure (not to scale) [62]. The numbers in the brackets give the degeneracy of the corresponding states.

The coupling of the lowest conduction band state Γ_6 to both the uppermost valence band holes Γ_7 and Γ_8 give rise to Z_3 and $Z_{1,2}$ edge excitons respectively in the case of CuCl. An exciton is the bound state resulting from the Coulomb attraction of an optically excited electron hole pair; it can be considered as the semiconductor analogue of the hydrogen atom [60]. The band structure of CuBr is qualitatively analogous to that of CuCl except for the ordering of the uppermost spin orbit split Γ_8 and Γ_7 valence band states. This leads to the appearance of the Z_3 exciton at a higher energy than the $Z_{1,2}$ exciton [61].

CuCl is a well-known model material to explore the basic features of excitons. The existence of exciton peaks at the absorption edge of CuX has been reported by several authors [63]. The CuCl crystal is the first known case where the creation of an excitonic molecule through an exciton- exciton collision process has been found [64]. The excitonic based luminescence in CuX has been studied by numerous researchers for the past four decades [35, 65-68], due to the much larger excitonic binding energies (E_b) compared to the III-V and II-VI semiconductors. The free excitonic binding energy and biexcitonic binding energy of CuCl and CuBr are 190 meV [68], 33 meV [69] and 108 meV [68], 25 meV [64] respectively. As the E_b is much larger than the thermal energy at room temperature (kT= 25 meV), CuX can exhibit stable excitonic properties over a wide temperature range. The luminescent properties of CuCl and CuBr thin films with layer thickness of 3.5–100 nm have been studied from the viewpoint of hot excitons [65]. The experimental evidence for the existence of an exciton molecule in CuCl using the absorption spectrum studies was reported by G.M. Gale *et al.* [70], and this is responsible for the nonlinear optical properties of this material. Furthermore, it has been found that the energy of

the free-exciton luminescence in the CuBr thin films has an oscillatory dependence on the excitation energy [65].

So far, there are several reports on the optical properties of CuX and their mixed crystals [1, 12-15, 35, 39, 65, 66, 68]. The fluorescence emission was investigated in single crystal CuCl at low temperatures by Y. Kaifu *et al.* [71]. Luminescence properties of the vacuum evaporated and sputtered CuCl thin films have previously been reported [72-74]. Again 10^2 or 10^3 times higher efficiency of free-exciton photoluminescence (PL) have also been reported in the case of CuBr films grown on KBr crystals than those grown on conventional substrates such as Al_2O_3 or silica glass [75].

1.7 Conductivity of CuX

Researchers have examined the electrical conductivities of CuX for more than half a century [75-79]. It was found that, the conductivity of CuX depends on the stoichiometry of the material [79]. Predominant ionic conduction through copper ions has been reported for samples without excess halogen [80] and electron hole conduction in addition to ionic conduction has been revealed for samples having deficit of copper [77]. Moreover, the dc voltage dependent resistivity of CuCl powder compacts under pressure has also been reported [81]. Wagner *et al.* studied the total electrical conductivity and hole conductivity of bulk copper halides (CuCl and CuBr) between 523 and 723 K using ac voltages at 1 KHz and dc polarization methods; and concluded that these materials are p-type semiconductors owing to Cu vacancies in the crystals [79]. Furthermore, measurement of conductivity, mobility and electron hole concentrations were carried out on single crystal CuCl by A. V. Joshi *et al.* [80]. They reported a hole carrier concentration and a mobility of

8.8×10^{12} cm^{-3} and 6.1×10^{-2} $cm^2V^{-1}s^{-1}$, respectively at 605 K for CuCl using electrochemical techniques. In a related development, Knauth *et al.* have performed room temperature Hall effect measurements on CuBr, and demonstrated a p-type conductivity due to metal deficiency [82].

The summary of various studies on the electrical characteristics of the CuX reveals that, these are naturally p-type mixed ionic–electronic semiconducting materials with a very low electronic conductivity at room temperature and above. Hence, some kind of doping methods have to be developed for the maximum exploitation of the interesting properties of these materials for future optoelectronic application and for the realization of a cuprous halide based UV/blue emitting device.

1.8 Thesis scientific questions

With the brief introduction about the importance of the short wavelength materials and the great potential of cuprous halides for the future optoelectronics in mind, the thesis has sought to address several scientific questions. Firstly, how can we develop an n-type cuprous halide and what are the properties of these n-type materials? Second, how does the n-type doping affect the electronic structure of cuprous halide material? Third, how can we develop a p-type doped cuprous halide material? Fourth, is it possible to realize a heterojunction diode using these doped materials? Fifth, does the heterojunction exhibit any photovoltaic properties? Lastly, as part of the CuX-based electroluminescence device development, how can we develop a transparent conducting electrode using some simple techniques? This thesis discusses and emphasizes the methods of doping of CuX and the characteristics of the doped films and also the realisation of the CuX based photovoltaic structures,

which are absolutely essential for the future research and applications based on these materials.

1.9 Thesis overview

The work that we are going to address in the thesis is the part of a broader project; its ultimate goal is the development of CuX-based light emitting devices and solar cells. The thesis addresses most of the issues required to step towards the realization of those final goals (Figure 1.4 (a) and (b)). A schematic structure of the electro luminescent device based on CuX is demonstrated in figure 1.4 (a). We present the development, characterisations and optimization of various layers (shown in fig.1.4 (a)) required for the fabrication of the light emitting devices, in different chapters of the thesis. Figure 1.4 (b) indicate the schematic structure of the CuX-based PV cell. The thesis describes the realization of one of the possible structures of the PV cell, using CuX material.

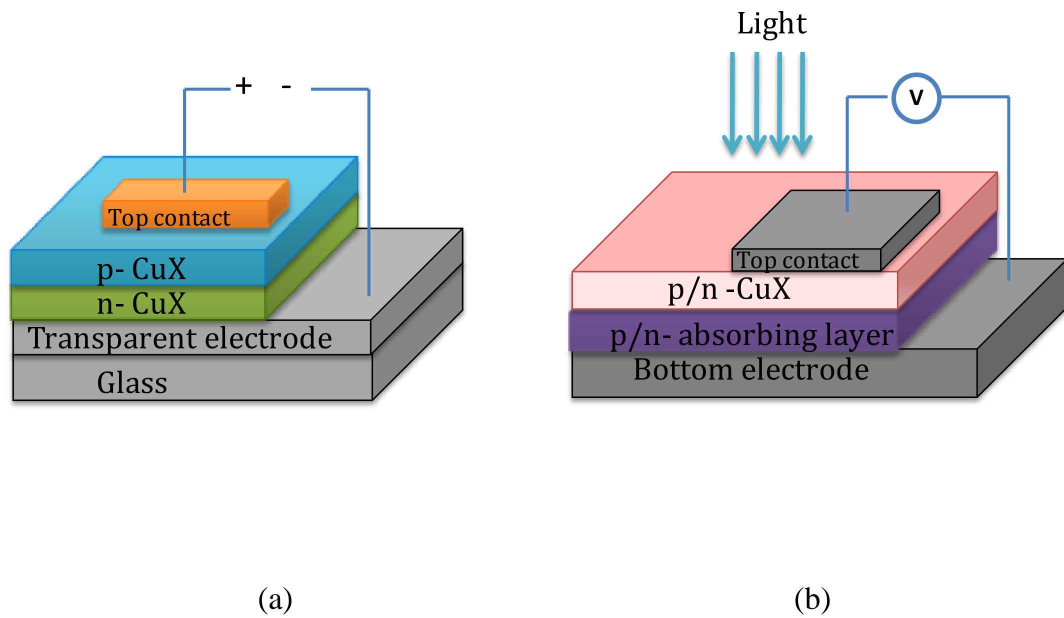

(a) (b)

Fig. 1.4: (a) Schematic of the CuX- based electroluminescent device structure using stacked layers of transparent electrode coated on glass, n-type CuX, p-type CuX and a top metal contact. The top and bottom electrodes will be connected to the battery. (b) Schematic of the PV cell structure using CuX. The various layers consist of a bottom electrode, p or n- absorbing semiconductor layer followed by p or n- CuX layer and then a top contact, with top and bottom contacts connected to a battery. The device will be illuminated from the top.

The following is an overview of the thesis.

Chapter 1 gives a brief introduction to the short wavelength materials based optoelectronics structures and the characteristics of CuX material systems.

Chapter 2 provides a description of the various experimental techniques used for the deposition of the thin films and the characterisation techniques used for their analysis.

Chapter 3 addresses the development of the n-type CuCl films and the structural, morphological and optoelectronic characterisation of the films.

Chapter 4 deals with results on the photoemission studies on the n-type CuCl, to understand the effect of doping on the electronic structure of CuCl.

Chapter 5 concentrates on the growth of the p-type CuBr films and their structural and optoelectronic characterisation and doping profiles.

Chapter 6 describes the development of the CuBr/Si based heterojunction diodes and photovoltaic cells and their characterisation.

Chapter 7 explains the deposition of transparent conducting ultrathin Cr-film, which can be used as an alternative for the well known ITO during the EL device development.

Chapter 8 concludes the thesis with the proposition of some future directions.

Chapter 2

Processing and characterisation techniques

2.1 Introduction

Several different techniques are available for the deposition of thin films. Among these, pulsed dc magnetron sputtering is a recently developed one, with great potential in the deposition of dielectric films and in reactive sputtering of insulating films. It actually broadens the demand of sputtered films into new markets by the deposition of reproducible high quality dielectric films. This thesis explores the development of doped and undoped CuCl and Cr films deposited by pulsed dc magnetron sputtering. The structural, morphological, optical and electrical characterisation of the deposited films is investigated using a number of different techniques. The details of the growth processes and characterisation methods of the samples are explained briefly in this chapter.

2.2 Film deposition methods

2.2.1 Sputtering

Sputtering is one of the most extensively used physical vapour deposition (PVD) techniques for the fabrication of thin films of materials on different substrates. It involves the ejection of atoms or molecules of a material from the target (cathode) followed by the deposition on to a substrate, by the energetic bombardment of ions from plasma. In order to start sputtering process, inert gas like Ar has to be

introduced in to the vacuum chamber (sputtering chamber) to get a pressure of the order of milli Torrs and then apply high voltage to the cathode, sufficient to ionize the gas. The positive ions created by this process are accelerated towards the cathode. The energy transfer from the bombarding ions to the material surface creates collision cascade in the target material that causes the ejection of atoms, ions, molecules, photons and secondary electrons. These secondary electrons play an important role in maintaining stable plasma discharge for the sputtering process. Due to the lower collision cross-section for electrons at lower gas pressures, the probability for escaping electrons without making collisions with gas increases. In order to use sputtering for the deposition of required thin film coatings, the bombarding ions should have sufficient energy to knock off the atoms from the target surface and the ejected atoms should move with minimal gas collisions towards the substrate. These can be achieved by producing efficient ionisation at lower pressures by using magnetron designs. In fact the low pressure sputtering is highly promising for the development of thin films with minimum contamination as well [83].

In order to confine the escaping electrons in the vicinity of the cathode and to enhance the ionization of the inert gas in the chamber even at lower pressures, an external magnetic field can be applied. This technique is termed as magnetron sputtering, which can be used to overcome the limitations such as lower deposition rate and gas ionization efficiencies associated with the basic sputtering process. To obtain this, usually the magnets are placed behind the target and the field is configured parallel to the target surface. The magnets are arranged in such a way that one pole is positioned at the central axis of the target and the second pole is formed by a ring of magnets around the outer edge of the target, which makes crossed

electric and magnetic field [84]. The schematic of the arrangement of the magnetron cathode and the sputtering deposition process is illustrated in figure 2.1.

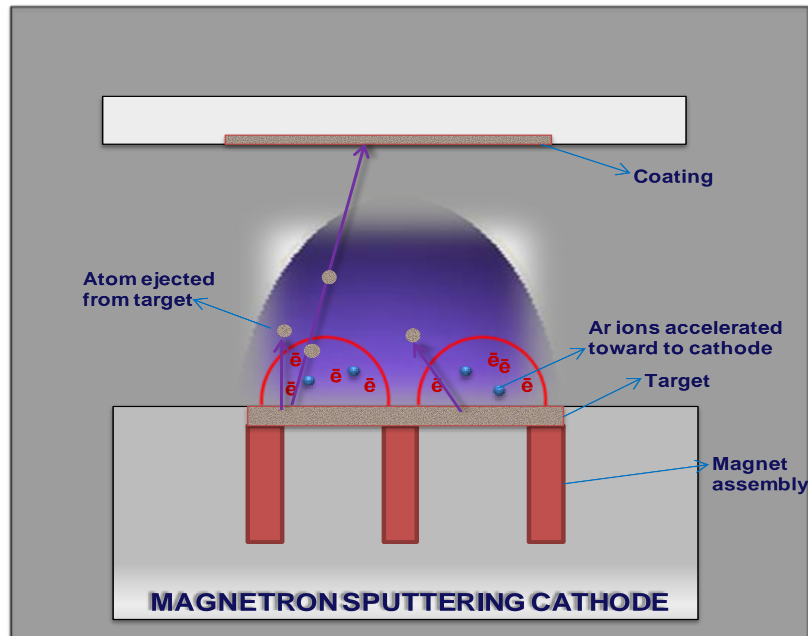

Fig. 2.1: Schematic of the magnetron cathode and the sputtering deposition process.

If the electrons have a velocity component perpendicular to the magnetic field, they can spiral around the magnetic field (i.e. electrons become trapped) with a frequency and radius, which is a function of the strength of the magnetic field [85]. The increased ionisation efficiency by this method leads to increased ion bombardment on the target and thereby increased sputtering rate. This also causes decrease of impedance of plasma which can help magnetron to operate at much lower voltages than diode systems. Permanent magnets are commonly used in magnetrons, with several different possible geometries. In addition to the conventional (balanced) type of magnetron assembly, there is another configuration available, termed as

unbalanced magnetrons. In balanced magnetrons, the plasma is closely confined to the target, up to ~ 60 mm from the target surface. Hence, films developed within this region will undergo ion bombardment, which can strongly influence the structure and properties of the growing film. Substrates placed out of this portion will be in the lower plasma density region, and hence not affected by sufficient ion bombardment. Contrary to the conventional type, some of the electrons are deliberately allowed to escape from the target surface, by adjusting the magnetic field in the case of unbalanced magnetron configuration. Hence these electrons create plasma closer to the substrate, which will help the reactive gases to reach near the substrate surface for reactive sputtering or for ion plating [85]. Depending on the nature of the power supply that is used to drive the magnetron, sputtering are of different types, like DC sputtering, RF sputtering, pulsed dc sputtering etc.

2.2.2 Pulsed dc magnetron sputtering

Pulsed dc magnetron sputtering has found increasing attention among researchers for the last decades [86, 87]. This has developed by combining the benefits of both DC and RF magnetron sputtering. Even if RF sputtering can make good quality films, the deposition rate is very low (~ µm/h range). Besides that RF sputtering systems are complex and difficult to scale up for industrial applications. The problems associated with the dc sputtering are (1) intricacy of the deposition of insulating layer and (2) poor long term stability of non metallic processes [84]. Furthermore, during the dc reactive sputtering of an insulating material using a metal target and a reactive gas in argon plasma, a film of the insulating material will deposit on the surface of the metallic target itself. As the deposition progress, this insulating layer will charge up in to high positive charge by the accumulation of positive ions from

plasma until a breakdown occurs in the form of an arc. These arc events can create ejection of droplets of materials from the target, which is detrimental to the required properties of the growing film.

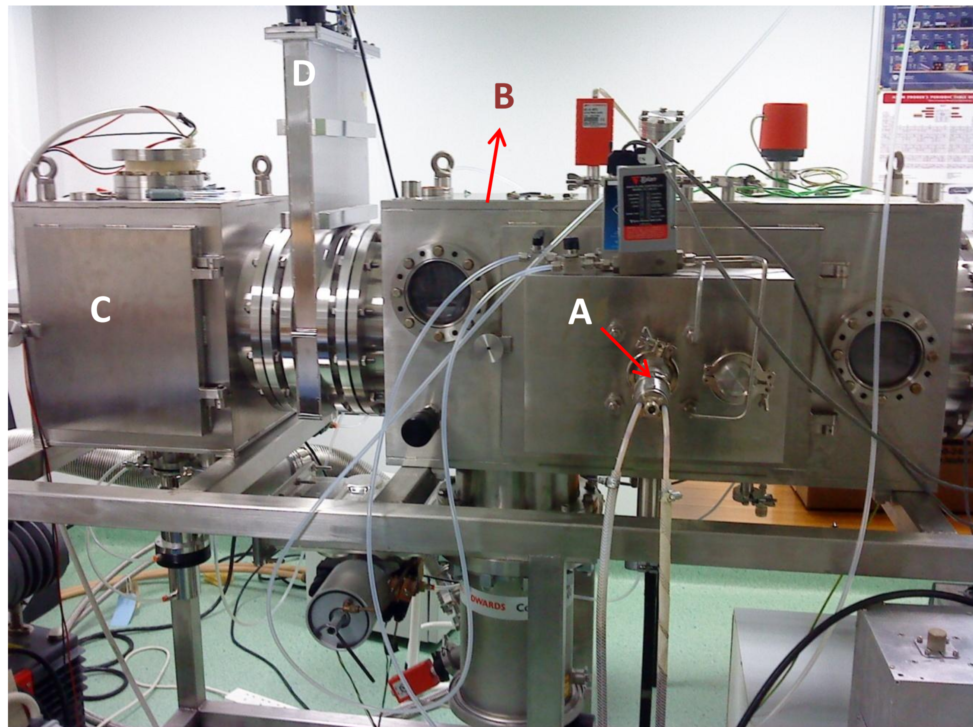

Fig. 2.2**:** Photograph of the sputtering system used for the experiment: A-magnetron, B- sputtering chamber, C- Loading chamber and D- Transfer valve.

Besides that, arcing can make rapid changes to the deposition parameters, and thereby change the stoichiometry of the film; it can even damage the magnetron power supply. The problem due to the accumulation of the charges can happen in the case of the dc sputtering of insulating targets as well. A photograph of the sputtering system used for the deposition process in this study is presented in figure 2.2. It consists of a magnetron (A) connected to the sputtering chamber B, which is separated from a loading chamber (C) by a transfer valve D. Pulsed magnetron

sputtering can be a better choice to overcome many of the problems one comes across with the deposition of the insulating films. It has been reported that pulsing the magnetron discharge in the medium frequency range (20-250 kHz) can significantly reduce the arcing and hence reduce the formation of defects in the film. In addition to that, it can increase the deposition rate to an order of tens of microns per hour; which is similar to that of the pure metal films.

Pulsed magnetron sputtering process usually employs a pulsed dc power. It can generate a condition by applying a short positive pulse in between; by disrupting the negative voltage to the target to eliminate the chances of arcing. An ENI RPG-100 asymmetric bipolar pulsed power supply was used for the film deposition in this work (figure 2.3).

Fig. 2.3: Photograph of the asymmetric bipolar pulsed power supply (ENI RPG-100) used for the deposition.

It is possible to dissipate the accumulated charges on the insulating layer on the target, completely or partially through the plasma during the pulse off period by

switching the target voltage to a more positive value. There are 2 modes of operation; unipolar pulsed sputtering and bipolar pulsed sputtering. In the former one, the target is operated between the normal voltage and ground and in the latter; the target voltage is reversed and becomes positive during the pulse off period. As the mobility of the electrons in the plasma is much higher than the ions, it is usually only essential to reverse the target voltage to between 10 and 20 % of the negative operating voltage in order to fully dissipate the charged regions and avoid arcing [84].

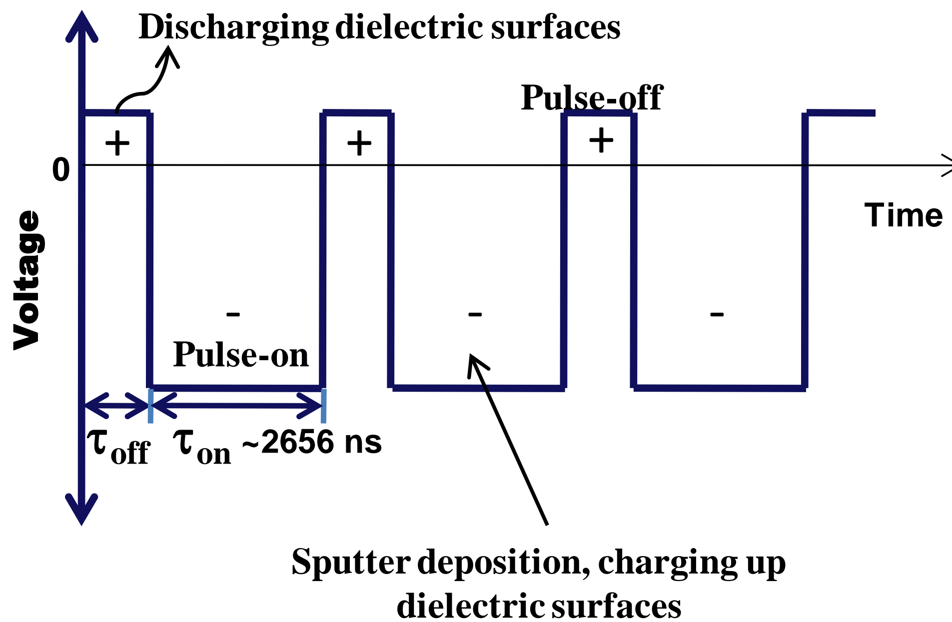

Fig. 2.4: Schematic of the asymmetric bipolar pulse dc signal used for the deposition. Sputtering of the target and the deposition on the substrates take place during the pulse on time of the pulse.

The bipolar pulsed dc power generates either a bipolar symmetric or a bipolar asymmetric pulse. The schematic of the illustration of the target voltage waveform for a pulsed dc power supply operating in the asymmetric bipolar pulse mode is as

shown in figure 2.4. The pulse parameters like pulse frequency and pulse duty cycle have significant influence on the properties of the deposited films.

The pulse duty cycle (δ) can be defined as the relative duration of the pulse on time,

$$\delta = \frac{\tau_{on}}{\tau_{on} + \tau_{off}} \qquad (2.1)$$

The duration of the negative polarity to the cathode is represented as the pulse-on time (τ_{on}) and that of the positive polarity is indicated as pulse-off time (τ_{off}). Thus, sputtering of the target material occurs during the pulse-on time and the discharging of the accumulated charge through the plasma takes place during pulse-off time.

2.2.3 Vacuum Evaporation

Vacuum evaporation technique is an example for physical vapour deposition technique. CuBr thin films required for present studies were deposited using an Auto 306 Edwards thermal resistor evaporation system. It is an automated system possible to work at a base pressure of 1×10^{-6} mbar by the operation of rotary and oil diffusion pumps. The evaporation pressure was around 3×10^{-6} mbar. An FTM6 thickness monitor connected with a water-cooled crystal holder is attached into the evaporation system. This is used to monitor the thickness of the deposited films. The commercially available CuBr powder taken in a Tungsten boat is evaporated by the resistive heating of the crucible and the evaporation rate can be controlled by adjusting the current flow through the crucible. The substrates are placed on a substrate holder about 10 cm away from the heated crucible.

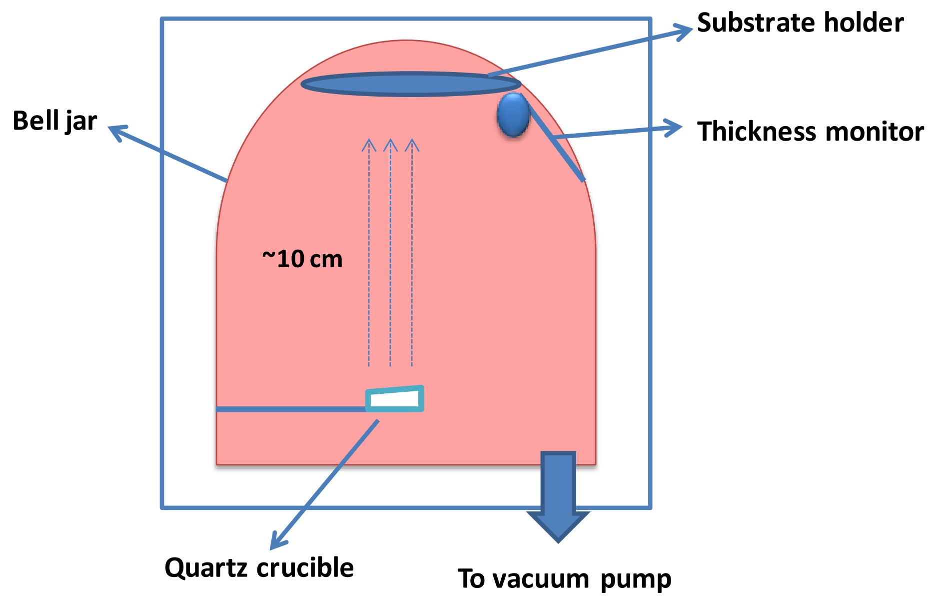

Fig. 2.5: Schematic diagram of the vacuum evaporator system. The bell jar is pumped down to ~10^{-6} mbar using the vacuum pump.

2.3 Characterisation techniques

2.3.1 X- ray diffraction (XRD) analysis

X-ray diffraction analysis is a non-destructive method extensively used to characterize the structure of crystalline materials. Besides the crystal structure analysis, the important applications comprise of phase analysis, texture analysis, and grain size measurement. The rapid deceleration of electrically charged particles with adequate energy can result in the formation of X-rays.

Fig. 2.6: Photograph of Bruker AXS Advance D8 XRD system.

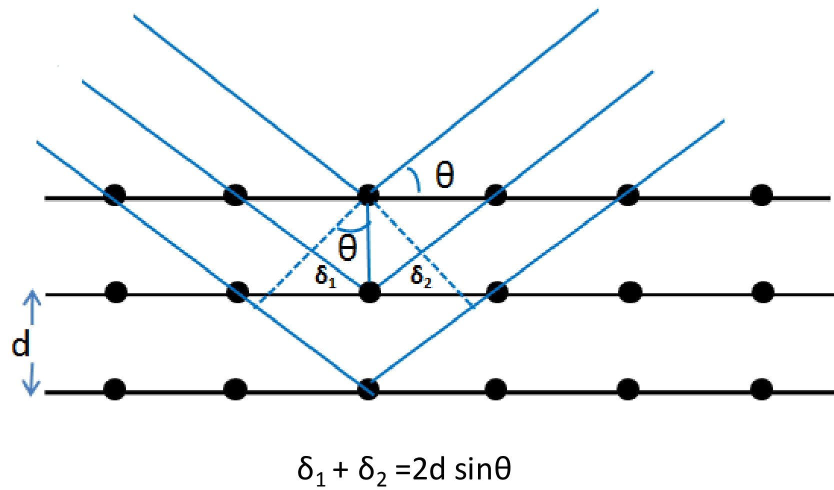

Fig. 2.7: Illustration of the Bragg's law. The figure indicates the conditions for the occurrence of Bragg's diffraction. Planes of atoms are indicated using the black soild lines.

A beam of X-rays when incident on a sample get scattered by the atomic electrons in to different directions. If these scattering centers of the sample are arranged in a periodic manner with a distance of separation analogous to the wavelength of X-rays, diffraction patterns are obtained. Hence this diffraction pattern can be considered as a finger print of the particular material under observation. The three dimensional lattice of a crystalline material consists of repeated planes of atoms arranged in a regular manner. Inter atomic distances in crystalline solids are of the order of few angstroms and the wavelength of the X-rays is also of the same order. When a focused beam of X-rays interact with these atomic planes, it gets scattered.
The essential condition for the occurrence of diffraction pattern was developed by English physicists Sir W.H. Bragg and his son Sir W.L. Bragg. It is given by,

$$n\lambda = 2dsin\theta \qquad (2.2)$$

Where n is the order of reflection, λ is the wavelength of X-rays used, d is inter planar distance and θ is the angle of reflection of X-rays. The structure of the CuCl based thin films were studied using a Bruker D8 Advance instrument using copper K_α radiation of wavelength 1.54 Å.

2.3.2 Scanning electron microscopy (SEM)

Scanning Electron Microscopy (SEM) is one of the most versatile instruments available for the investigation of microstructure and chemical composition of materials. The vital advantage of SEM over the ordinary optical microscope is its extremely higher magnification (~>100,000X). SEM uses electron beam for imaging, instead of the visible light in the optical microscopes.

Fig. 2.8: Photograph of the Zeiss EVO LS-15 SEM system.

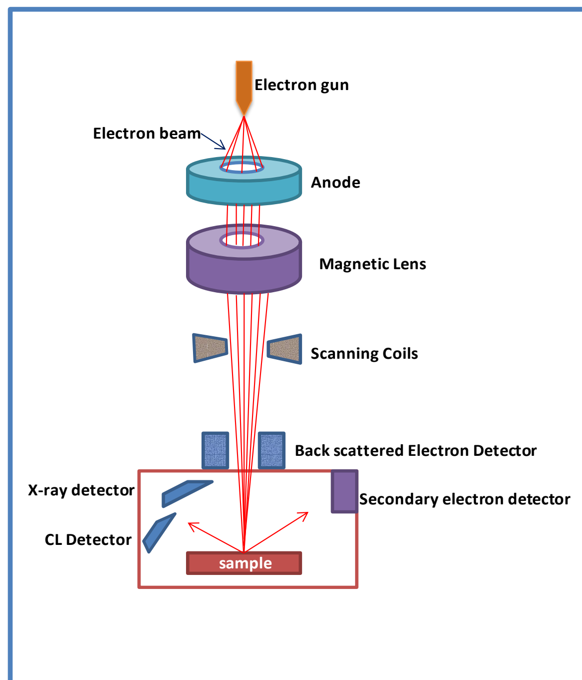

Fig. 2.9: Schematic of the SEM system. The electron gun and the lensing system to focus the electron beam on to the sample surface are illustrated.

The precise characterisation using highly energetic electron beams can yield information about the topography, composition and crystallography of the materials under investigation using SEM. The SEM was developed to overcome the limitations of the optical microscope such as lower resolution of ~ 2000 Å. In the SEM, electron beam is produced in high vacuum by electron gun, and this beam is then accelerated towards the sample with the help of positive electric field, and then focussed on to the sample with the help of magnetic lenses. This focussed electron beam interacts with the sample surface, and this interactions is transformed in to an image of the sample. The resolution of the SEM image varies as a function of the electron spot produced by the magnetic lenses. The electron beam interacts with certain volume of the sample under investigation, and the depth of this interaction volume is a function of the composition of the sample, energy and angle of the incident electron beam [88].

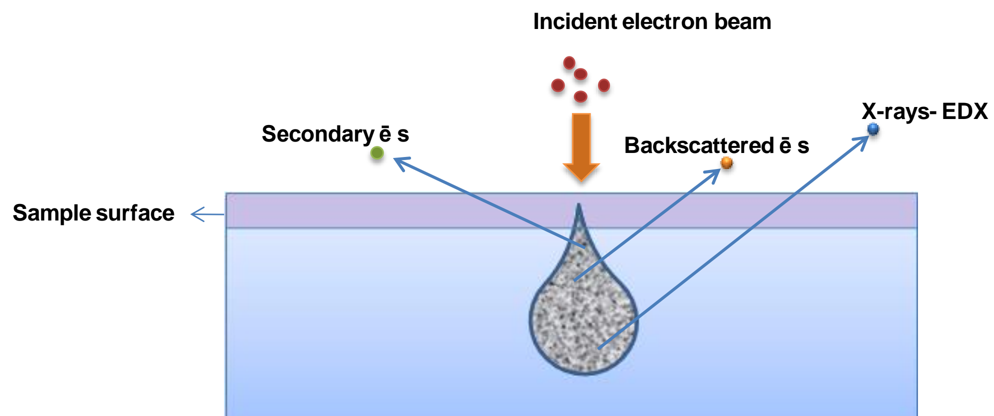

Fig. 2.10: Illustratioin of the different signals generated by the electron beam-specimen interaction in SEM and the regions from which the signals can be detected.

The figure 2.9 shows the generation of various signals as a result of the interaction of the sample atoms with the incoming electron beam, consists of secondary electrons, back scattered electrons, transmitted electrons (all these are for imaging), X-rays, heat, photons etc. The creation of secondary electrons are highly related to the topography of the sample. Similarly, the creation of the backscattered electrons varies with samples's atomic number. ZEISS EVO LS-15 SEM system was used for the analysis of the CuCl films in this study.

2.3.3 Energy dispersive X-ray analysis

The X-ray signals produced due to the interaction of the electron beam with the sample during the SEM analysis are used for the energy dispersive X-ray spectroscopic (EDX or EDS) studies, which is generally called micro analysis. The bombardment of the primary electons on the sample surface gives rise to the ejection of the inner shell electrons of the sample, and the transition of the outer electrons to fill up the vaccancy in the inner shell causes the production of x- rays: the finger prints of the elements present in the sample. The EDX spectrometer collects these x-rays and the elemental analysis is possible using the x-ray peak intensity and position informations with the help of the software associated with the system .

The elemental analysis of the CuCl samples is investigated using an INCAx-act detector attached to a Zeiss EVO LS-15 SEM.

2.3.4 Photoluminescence (PL)

The emission of radiation from a solid by providing some form of energy for excitation is generally termed as luminescence. Luminescence spectroscopy is an influential technique to characterise optoelectronic semiconductor materials.

Photoluminescence (PL) is the most extensively used method, in which the luminescence happens due to excitation produced by the absorption of photons. PL measurement is an efficient method to examine the electronic structure, photochemical and optical properties of semiconductor materials. PL involves the impingement on the sample by photons of energy greater than the band gap of that sample material. The irradiation of photons with sufficient energy can create electrons in the conduction band and holes in the valence band. If the relaxation of these excited electrons is radiative, then the process is called photoluminescence.

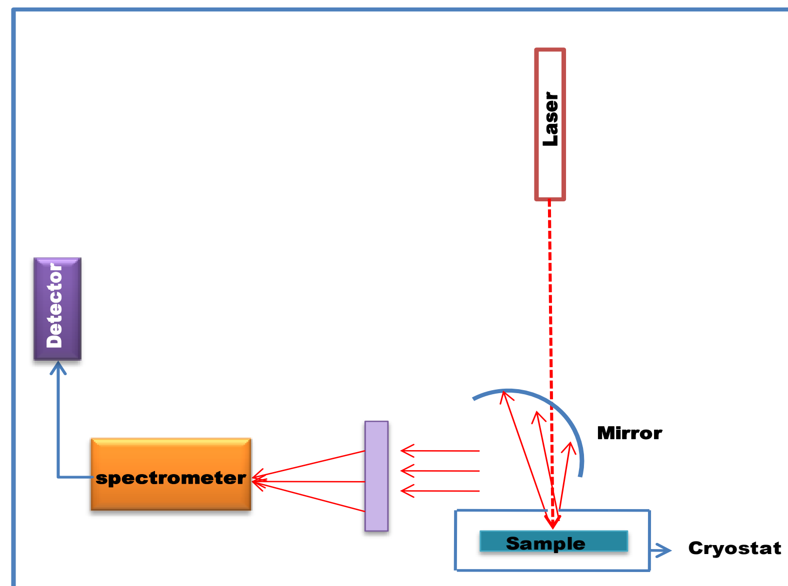

Fig. 2.11: Schematic of the PL experimental set-up.

PL can be used to determine the band gap, native and intrinsic defect levels. In the case of the indirect band gap semiconductors, photon emission takes place along with the emission of phonons to conserve the momentum within the lattice. Temperature dependent PL measurements were also performed.

In this study, temperature dependent PL measurements were carried out on CuCl samples using a 244 nm (~ 5.1 eV) excitation produced by an Ar ion Innova laser form 20K to room temperature. The Luminescence was recorded using TRIAX 190 Jobin Yvon-Horiba spectrometer with a resolution of 0.3 nm.

2.3.5 UV –Vis absorption spectroscopy

Absorption spectroscopy is a technique for examining the optical absorption of energy radiations as a function of wavelength due to its interaction with a material. Absorption spectrum is the variation of absorbed radiations as a function of wavelength.

Fig. 2.12: Photograph of the Perkin Elmer Lambda 40 UV-Vis spectrometer.

Ultraviolet and visible (UV-Vis) absorption spectroscopy is one of the common methods for investigating the energy level structure of materials. In the semiconductor point of view, it is a simple method for the determination of the band gap of the material. The UV-Vis absorption spectra of the CuCl samples are investigated using a Perkin Elmer Lambda 40 spectrometer.

2.3.6 Atomic force microscopy

Atomic force microscopy (AFM) is a technique used for the imaging of the surface topography of variety of materials in the atomic scale. It is a Scanning Probe Microscopic system, which consists of a very sharp probe (tip) connected to the free end of a candilever having length ~ 100-200 μm. In a typical AFM equipment, a constant force is kept in between the probe and the sample surface during the scanning of the probe. AFM tips are commonly made from silicon or silicon nitride. A three dimensional image of the surface is created by monitoring the movement of the probe, using an optical lever detection system, in which a laser beam is reflected from the catilever tip onto a position-sensitive photodiode, while it scans across the surface. An extremely precise scanning across the sample can be realized using positioning devices made from piezo electric materials. There are three commonly used imaging modes; contact mode, non contact mode and tapping mode, to image the topography of a sample. In the contact mode the tip is basically in contact with the sample surface, that may damage the sample surface. It is mainly used for the imaging of smaller areas of the sample with high resolution. Non contact mode is less damaging, in which, the tip floats over the sample surface, and measures the van der Waals forces between the tip and the sample.

In tapping mode, the probe taps the sample surface rather than pull in to it. During the tapping mode operation, the tip oscillates at 50- 100 kHz with an amplitude 20-200 nm with the help of a piezoelectric crystal.

Fig. 2.13: Image of the AFM scanning set-up.

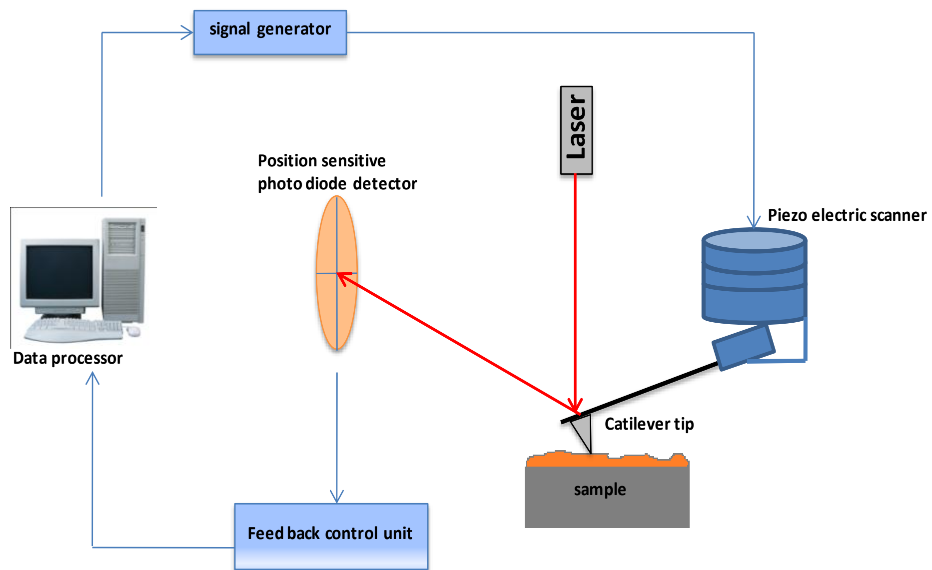

Fig. 2.14: Schematic of the AFM measurement set-up

The AFM technique has the following advantages. Unlike other conventional microscopic systems, it can explore the sample and perform measurements in the x, y and z directions along the surface and hence can provide the three dimensional image of the sample surface. It can be used to image most of the materials including glasses, ceramics, polymers and biological samples. It can work in ambient without the assistance of special sample preparation method. A Pacific Nanotechnology Nano-R AFM was used for this study.

2.3.7 Four-point probe technique: Resistivity

Four point probe technique is one of the most common methods for measuring resisitivity. It consists of four linearly arranged needle-like electrodes, in which, current is injected in to the material by the two outer electrods.

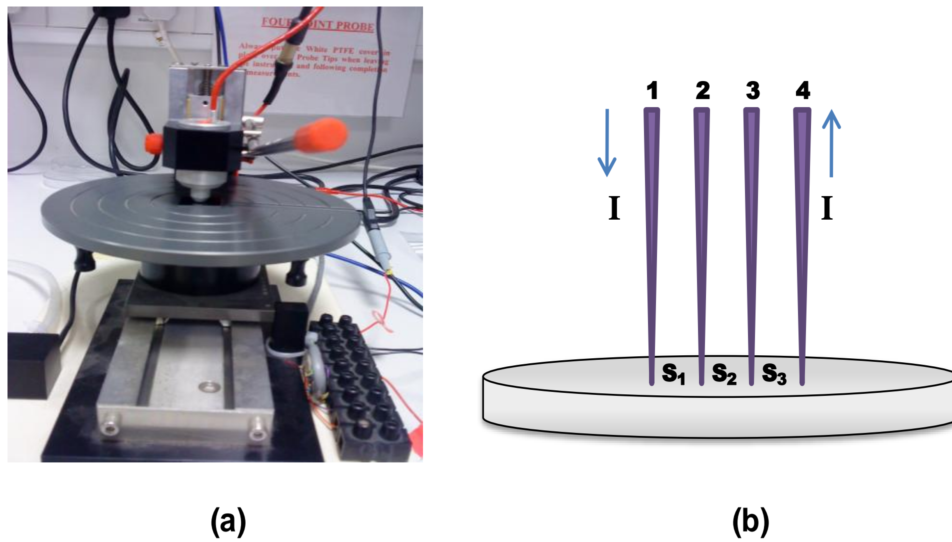

Fig. 2.15: (a) Photograph of the Four point probe measurement setup and (b) schematic of the collinear four point probe.

The resultant electric voltage is measured beteen the two inner electrodes. The influence of the contact resistance between the metal electrode and the material surface can be minimized by using seperate electrode pairs for the current injection and the voltage measurement. Nowadays the four point probe technique is extensively used for observing the fabrication process in the semiconductor technology. The resisitivity ρ of the semiconductor material can be expressed as,

$$\rho = \frac{1}{q(n\mu_n + p\mu_p)} \tag{2.3}$$

Where, n and p are free electron and hole densities and μ_n and μ_p are electron and hole mobilities respectively. Hence four point resistivity can be used to get primary information about the doping effect in semiconductors.

The voltage at probe 2 can be written as,

$$V_2 = \frac{I\rho}{2\pi}\left(\frac{1}{s_1} - \frac{1}{s_2 + s_3}\right) \tag{2.4}$$

Similarly, the voltage at probe 3 can be written as,

$$V_3 = \frac{I\rho}{2\pi}\left(\frac{1}{s_1 + s_2} - \frac{1}{s_3}\right) \tag{2.5}$$

The total measured voltage can be expressed as,

$$V = V_2 - V_3 = \frac{I\rho}{2\pi}\left(\frac{1}{s_1} - \frac{1}{s_2 + s_3} - \frac{1}{s_1 + s_2} + \frac{1}{s_3}\right) \tag{2.6}$$

Hence, with equal probe spacing i.e., $s_1=s_2=s_3=s$, the resistivity ρ is given by,

$$\rho = 2\pi s \frac{V}{I} \tag{2.7}$$

The resistivity ρ is usually expressed in ohm cm (Ω cm). The equation corrected for finite geometries of the semiconductor wafers can be written as,

$$\rho = 2\pi s F \frac{V}{I} \tag{2.8}$$

Where F is a correction factor which depends on the sample geometry, and it can be expressed as a function of various independent correction factors, $F=F_1F_2F_3$. F_1 corrects for the thickness of the film used. For a non-conducting wafer surface boundary, F_1 can be expressed as,

$$F_1 = \frac{t/s}{2ln\{[sinh(t/s)]/[sinh(t/2s)]\}} \tag{2.9}$$

Where, t is the layer thickness. For thin samples ($t \leq s/2$), equation (2.9) reduces to

$$F_1 = \frac{t/s}{2ln2} \tag{2.10}$$

From equations (2.8) and (2.10), ρ can be written as,

$$\rho = 4.532t(V/I)F_2F_3 \tag{2.11}$$

F_2 corrects for the lateral sample dimensions,

$$F_2 = \frac{ln(2)}{ln(2) + ln\left\{\left[(D/s)^2 + 3\right]/\left[(D/s)^2 - 3\right]\right\}} \tag{2.12}$$

Where, D is the dimension of the sample along the parallel direction of the pins.

For D ~ 50 mm, from equation (2.12) (s=1 mm), F_2 =0.9965.

Again the third correction factor, F_3 corrects for the closeness of the sample boundary to the probes. This turns to unity, when the normalised distance from the boundary to the probes, d ≥ 4 mm. This condition is satisfied in our case.

Applying correction factors F_2 and F_3 in equation (2.11), the resistivity can be expressed as,

$$\rho = 4.516\, t \frac{V}{I} \tag{2.13}$$

Thin layers are generally characterized by their sheet resistance R_s expressed in units of ohms per square (Ω/□). Sheet resistance of uniformly doped sample is given by,

$$R_s = \frac{\rho}{t} = 4.516 \frac{V}{I} \tag{2.14}$$

2.3.8 Hall Effect experiment

Hall effect measurement technique is a method extensively used for the characterisation of semiconductor materials, as it gives resistivity, carrier density, carrier type and the mobility of materials. Hall effect was discovered by E. H. Hall in 1879. When a magnetic field B_z is applied in a direction perpendicular to the direction of applied electric field E_x in a semiconductor material, a transverse field develop perpendicular to both E_x and B_z ie, along the y-direction. Figure 2.15 shows the applied electric field along x-axis and the magnetic field along z- axis. Consider a p-type semiconductor material. The holes moving along the x-axis are affected by a Lorentz force [q $(v \times B)$ $=qv_xB_z$] in the upward direction due the presence of the magnetic field. This causes an accumulation of holes in the top surface of the sample.

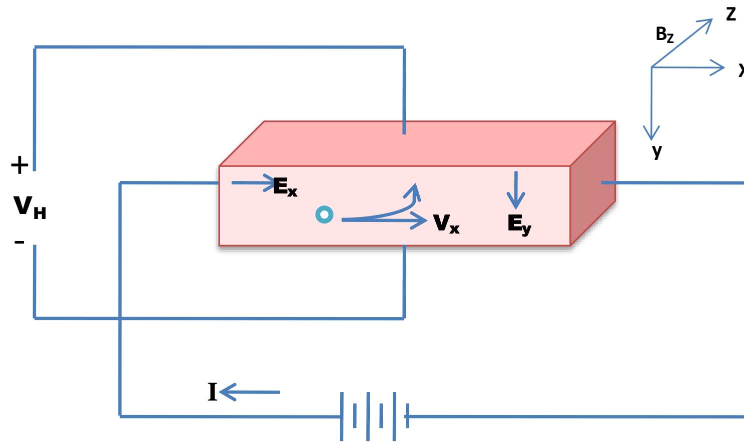

Fig. 2.16: Visualisation of the Hall effect measurement set-up.

The upward directed hole current produces an electric field E_y in the downward direction. In the steady state, there is no current flow along the y-direction, Lorentz force and the electric field along the y direction exactly matches i.e.

$$qE_y = qV_xB_z \tag{2.15}$$

When substitute for the Hall drift velocity V_x ($J_p = V_x qp$, where J_p is the hole current density, q is the charge and p is the hole concentration), the equation becomes, Hall field,

$$E_y = R_H J_P B_Z \tag{2.16}$$

Where R_H is the Hall coefficient given by,

$$R_H = \frac{1}{qp} \tag{2.17}$$

Similarly for the n-type semiconductor, the Hall coefficient can be written as,

$$R_H = -\frac{1}{qn} \tag{2.18}$$

The conductivity (σ) of the semiconductor material (p-type) can be expressed as,

$$\sigma = q\mu_p p \tag{2.19}$$

Where, q is the charge, μ_p is the hole mobility and p is the hole concentration. Hence,

$$\mu_p = R_H \sigma \tag{2.20}$$

Fig. 2.17: Photograph of the HL 5500 PC Hall measurement set-up.

The Hall coefficient and Hall mobility are usually expressed in units of cm^3C^{-1} and $cm^2V^{-1}s^{-1}$. The carrier concentration is written as,

$$p = \frac{1}{qR_H} \tag{2.21}$$

Thus the carrier concentration and the carrier type can be obtained directly from the Hall measurement.

An HL 5500 PC Hall effect measurement system was used to investigate the carrier concentration, resistivity and mobility of the doped samples.

2.3.9 X-ray photoelectron spectroscopy (XPS)

Photoelectron spectroscopy (photoemission spectroscopy) is a well-known method used for the investigation of the electronic structure of atoms and molecules. It is an extensively used technique based on the photoelectric effect, for the investigation of the chemical composition of the surfaces, developed by Kai Siegbahn and his group in the 1960's. Surface analysis using XPS can be realised by the irradiation of the samples with mono-energetic soft X-rays followed by the analysis of the kinetic energy of the electrons ejected as a result of the photoelectric effect. In this, the ejection of a core level electron occurs by an x-ray photon of energy hυ. The analysis of the energy of the emitted photoelectron is carried out by an electron spectrometer and the result is presented as the x-ray induced photoelectron spectrum, which is a graph of intensity versus electron energy. Core electrons are those electrons which are tightly bound to the nucleus with higher binding energies. They do not participate in the chemical reactions like valence electrons.

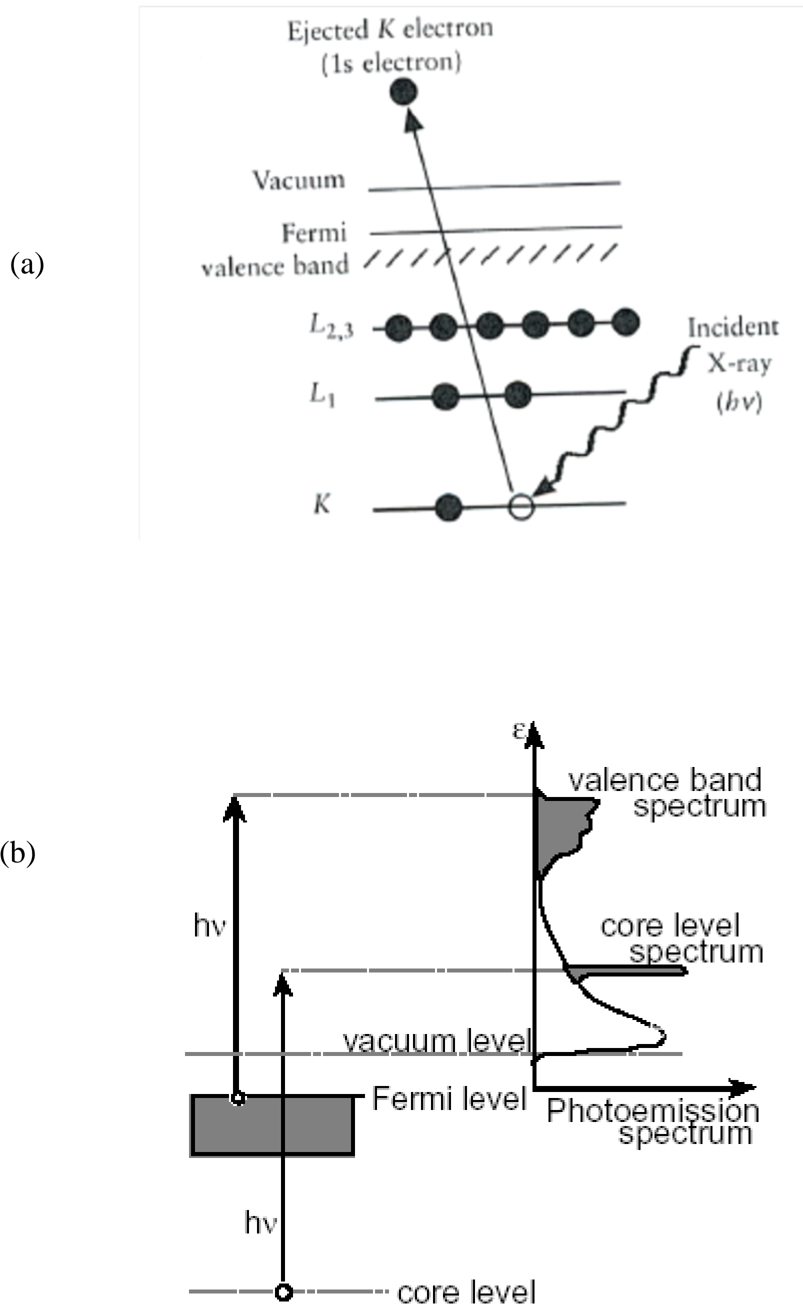

Fig. 2.18: (a) Schematic diagram of the photoemission process, which shows the photo ionization of an atom by the ejection of a 1s electron [89], (b) demonstration of the formation of the photoemission spectrum [90, 91].

The binding energy data can be used for the qualitative analysis of a sample, since various atoms in the sample have their own core electron binding energy values. The shift in the binding energy occurs according to the chemical state of the atom under observation and its chemical environment. The photoemission process can be approximated to a model consists of three different processes [90]. It consists of (1) excitation of photoelectron followed by (2) its movement to the surface and then (3) its penetration through the surface to the vacuum, where it is collected by the detector. The expression for the binding energy of the electron (E_b) can be written as,

$$E_b = h\nu - E_K - W \tag{2.22}$$

here, hυ is the photon energy, E_K is the kinetic energy of the electron and W is the work function of the spectrometer. It is found that there is a possibility for the variation of the kinetic energy of the ejected electrons due to the atomic collisions and phonon interactions happened inside the sample, before it escapes from the sample surface. The probability of such effects can be determined using a term called the inelastic mean free path of the material- the characteristics length through which the electron can travel without having energy loss. The demonstration of the process of photoemission and the formation of the photoemission spectrum is shown in the schematic diagram in figure 2.18 (a) and (b). The electrons, which are excited without any energy loss due to scattering, will contribute to the characteristic peaks in the spectrum. The electrons, which lose energy due to the scattering during the transportation process, can be detected as the secondary electrons. Hence useful information from the photoemission studies can be observed from the first 5-10 nm from the surface of the sample.

2.3.10 Secondary ion mass spectroscopy (SIMS)

SIMS is the most important physical method used in the material science field for the quantitative analysis of the solid surfaces and thin films. The surface of the samples is bombarded using high energy focused ion beam, which causes sputtering of the sample. The ejected secondary ions are then collected and analyzed using mass spectrometer. The composition of the sample can be extracted from the information on the count rate of different secondary ions species ejected from the sample. It is a very sensitive technique and allows the measurements of trace elements at very low concentration (ppb). SIMS needs high vacuum of the order of 10^{-6} mbar in order to minimize both the collision of the ejected secondary ions with the background gas and surface contamination of the samples due to the adsorption of the background gas during the measurements. SIMS has the capability of depth profiling, since the sample is sputtered away layer by layer as the measurements proceeds.

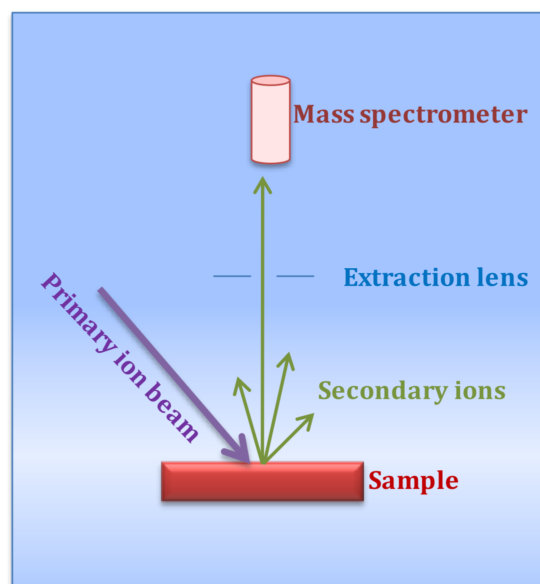

Fig. 2.19: Schematic of the SIMS analysis.

The depth profile of a particular element can be obtained by the observation of the count rate of the element as a function of time. SIMS measurements on the undoped and oxygen doped CuBr samples were carried out with the help of Dr. Richard Morris, Department of Physics, University of Warwick. The equipment used for the studies was an ultra low energy, Atomika 4500 Ultra-Shallow SIMS, capable of doing depth profiling at very high resolution ~ 0.9 nm.

Chapter 3

Growth and characterisation of n-type CuCl

3.1 Introduction

The investigation of materials for solid-state lighting has a fundamental role in the development of cost-effective and environmentally friendly light sources. Wide band gap materials like GaN and ZnO are being studied extensively by many researchers [27, 92, 93]. But as discussed in chapter 1, a crucial problem associated with these materials is the presence of threading dislocations due to the lattice mismatch with non-parental substrates [23, 94]. Furthermore, ZnO suffers from difficulties in producing a consistent p-type material [95-97]. The wide band gap, zincblende, I-VII compound semiconductor, γ-CuCl, could be a worthwhile candidate due to its small lattice mismatch with Si (< 0.4 %). The exciton stability could see this material system develop into an efficient candidate for UV LEDs and diode lasers operable at room temperature. To make use of the advantages of CuCl in real devices, there should be a reliable technique for doping this material system.

There have been several reports on the electrical properties of cuprous chloride and related halides by many authors: Brendahan *et al.* [98] investigated the total conductivity and the electronic conductivity of CuBr thin films between 186 K and 350 K using impedance spectroscopy and DC polarization methods; Knauth *et al.* [82, 99] performed room temperature Hall effect measurements and Mott-Schottky

analysis on CuBr thick films, while Lucas *et al.* [74, 100] probed the total conductivity and the electronic conductivity of CuCl thin films between 160 and 400 K using impedance/admittance spectroscopy and DC polarization methods. The summary of all these experiments is that cuprous halides are naturally p-type mixed ionic–electronic semiconducting materials with a very low electronic conductivity at room temperature and above. The hole conductivity arises from a Cu deficiency δ, in the copper halide crystals ($Cu_{1-\delta}X$: where X = Cl, Br or I). As part of the effort for the realization of exciton related light emitting devices using CuCl, O'Reilly e*t al.* [101] co-evaporated $CuCl/ZnCl_2$ thin films and demonstrated the first n-type CuCl based films. However, the carrier concentration in these doped films was very low ($n \sim 1 \times 10^{16}/cm^3$) probably due to compensation effects caused by the simultaneous introduction of excessive Cl atoms from the co-evaporation of $ZnCl_2$.

The optoelectronic properties of n-type CuCl:Zn thin films with improved carrier concentrations grown by pulsed dc magnetron sputtering on glass and Si substrates is presented in this chapter. Unlike the vacuum evaporation technique, sputtering is capable of depositing thin films of repeatable stoichiometry [102] which is crucial for the reliable performance of a compound semiconductor material like CuCl:Zn [43]. In addition to this, the use of Zn powder instead of $ZnCl_2$ will prevent the problems of additional Cl inclusion during film deposition as was experienced in the co-evaporation of $CuCl/ZnCl_2$ films [101].

3.2 Experimental methods

Thin films of CuCl:Zn were prepared by pulsed dc magnetron sputtering of a CuCl/Zn target, with the weight percentage of Zn in the target varying from approximately 0-5% (where 0 % signifies the undoped CuCl target), onto glass and

Si substrates. Sputtering targets were prepared by compressing a mixture of required weight percentages of Zn powder and CuCl powder in a copper backing plate using a hydraulic press. Prior to deposition the substrates were ultrasonically cleaned using acetone, trychloroethane and methanol followed by de-ionised water. An ENI RPG-100 pulse generator was used to drive a planar magnetron fitted with the target in the power regulation mode. The chamber was first pumped down to a base pressure of $2x10^{-7}$ mbar by cryogenic pumping. The target was pre-sputtered for about 10 minutes prior to deposition in order to reduce the contamination and to obtain a stable plasma density. Sputtering was carried out in pure argon atmosphere and the working pressure was adjusted to 5.5×10^{-3} mbar. The target to substrate distance was adjusted in between 3 and 6 cm. The power density at the target and duty cycle of the pulse were optimized from a number of iterations to be 1.73 W/cm^2 and 40%, respectively. The substrates were held at floating potential and the sputtering time was adjusted to 10-15 minutes to obtain a uniform film thickness of 350 ± 20 nm for all the deposited samples (the thickness was measured using Profilometer and then verified by AFM, later on inferred from the sputter deposition rate ~35 nm/min).

X-Ray diffraction (XRD) analysis was carried out using Copper K_α radiation of wavelength 1.54 Å to determine the crystallinity of the CuCl:Zn films. The morphology of the thin films was investigated using Scanning Electron Microscopy (SEM). Circular gold ohmic contacts of 1mm diameter were evaporated on the films deposited on glass substrates. Hall effect measurements were carried out in the van der Pauw configuration. UV/Vis absorption spectra of the films were explored in a range of wavelengths from 320-420 nm. Temperature dependent photoluminescence (PL) measurements were carried out from room temperature down to 17 K by employing a closed helium cryostat system and a 355 nm excitation laser.

3.3 Results and discussion

3.3.1 Pulsed dc magnetron sputtered CuCl

As discussed in chapter 2, the freedom to play around with sputtering parameters to improve the quality of the deposited films becomes broad in the case of pulsed dc magnetron sputtering compared to other types of sputtering methods. The selection of suitable sputtering parameters for the development of good quality CuCl films were performed after several repetitions of the experiments, with varying conditions of sputtering parameters. The optimization of the process conditions was established by observing the structural, morphological and optical properties of the films. The pulse duty cycle and other variables such as sputtering pressure, target power and target substrate distance etc. have to be optimized. A pulsed power of 35 W (target power density=1.73 W/cm^2) was used for the preparation of the films, due to the fact that, as the power increases to a range of 40-45 W, the deposition rate increases, but there is significant target heating. This can even cause the CuCl target to dislodge out of the Cu backing plate after repeated sputtering and also the decomposition of CuCl material.

Working gas pressure of the sputtering chamber has an effect on the scattering of the sputtered species from the target and thereby on the properties of the deposited films. The sputtering pressure was optimized to a value of 5×10^{-3} mbar, by looking at the structural, morphological and optical properties of the deposited films.

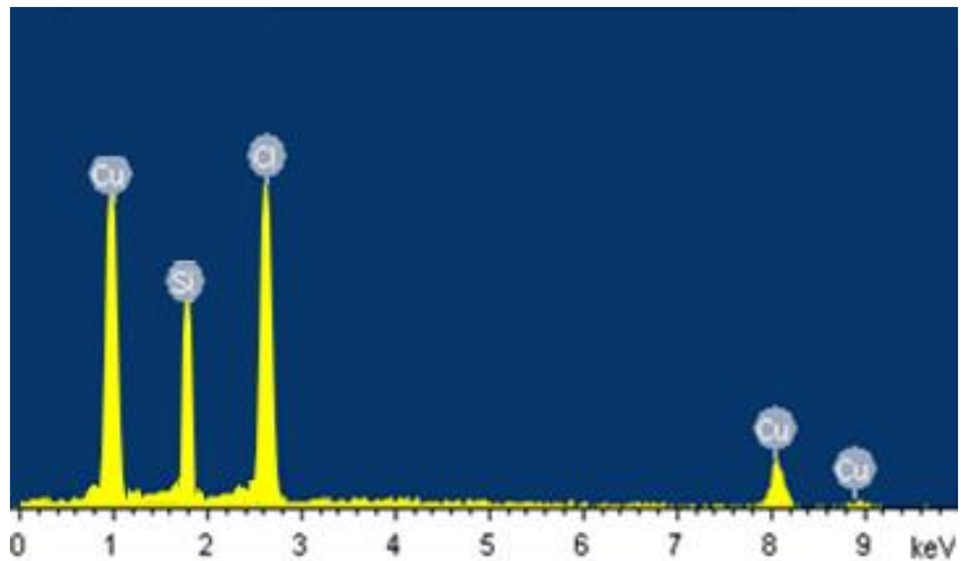

Fig. 3.1: A typical EDX spectrum of a CuCl film deposited at a target substrate separation of 6 cm, with a sputtering pressure and power density of 5×10^{-3} mbar and 1.73 W/cm^2 respectively. The accelerating voltage used for the EDX analysis was 13 kV.

Furthermore, the target to substrate distance can influence the stoichiometry of the film. Three different target substrate distances: 3 cm, 6 cm and 9 cm were used in these studies. It was observed from the EDX analysis that the Cu/Cl ratio is closer to 1 (more stoichiometric) for the films deposited using a target substrate distance of 6 cm than that of 3 and 9 cm. Similar kind of observations were reported by Gomathi *et al*. in RF sputtered CuCl [73].

Figure 3.1 shows a typical EDX spectrum of a CuCl film deposited on Si substrate with the optimised conditions of pressure, power density and target substrate distance. Characteristic lines from Cu and Cl are marked in the spectrum. The strong Si line is from the Si substrate.

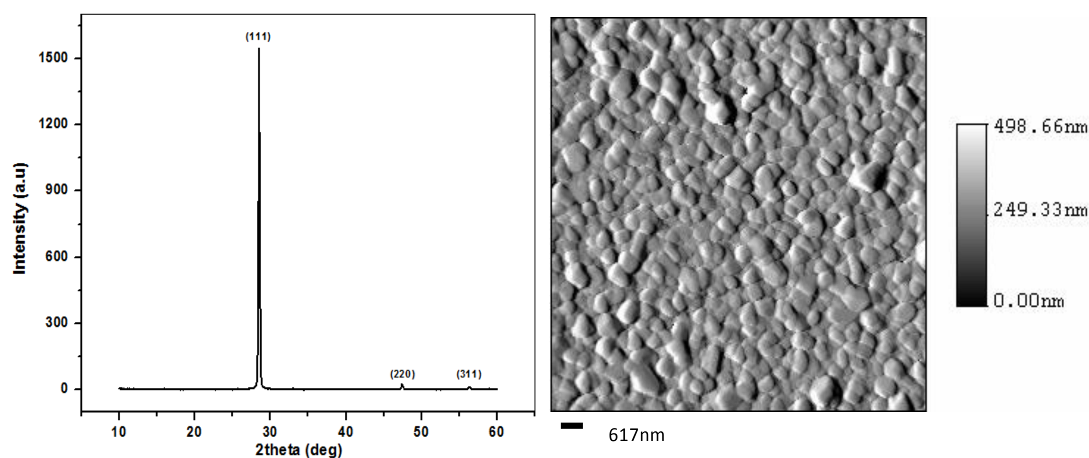

Fig. 3.2**:** XRD spectrum and AFM image of a typical CuCl film deposited using optimized conditions of power (40 W), pressure ($5.5 x 10^{-3}$ mb), target substrate distance (6 cm) and pulse duty cycle (40 %).

The crystal quality and morphology of the CuCl film grown with optimized deposition conditions are shown in the figure 3.2. The XRD pattern shows the preferential orientation of the grains along the (111) direction with the appearance of a strong peak around 28.5°. Slight contributions from the (220) and (311) orientations can also be observed in the XRD pattern. It is clear from the AFM image that the distribution of the grains is quite uniform throughout the film.

The optimized processing conditions for the deposition of the undoped and Zn-doped CuCl are given in the table 3.1. These conditions are optimized based on the structural and optical characteristics of the films to get relatively good crystal quality and optical quality.

Table 3.1: Sputtering process conditions used for the deposition of the undoped and Zn-doped CuCl films. The substrates used were Si and glass slides.

Process Parameters	Used values
Sputtering pressure (mbar)	5.5×10^{-3}
Argon gas flow(SCCM)	5
Target power density (W/cm^{-2})	1.73
Target substrate distance (cm)	6
Pulse frequency (kHz)	150
Pulse width (μs)	2.656

When a group II element is substituted into the copper site, it is expected to act as a donor for copper chloride. In the present case, Zn is used as the dopant, since it has almost the same ionic radii as that of Cu. The figure 3.3 shows an expected schematic diagram of a Zn doped CuCl lattice, with Zn substituted for Cu in the lattice. Some expected Cu-vacancies, which are anticipated in the natural CuCl are also included in the schematic.

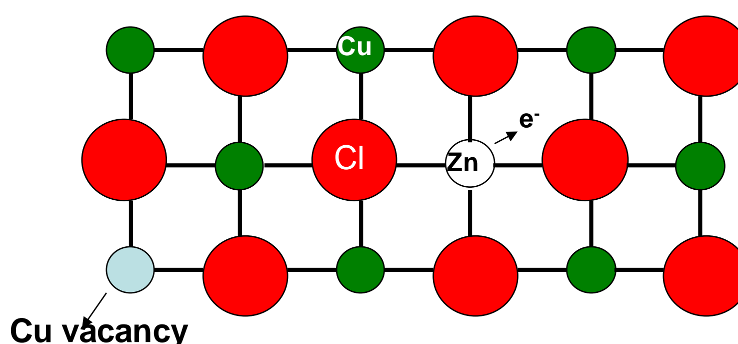

Fig. 3.3: Schematic of the expected CuCl lattice after Zn doping. Zn substitute Cu, and donate an extra electron into the lattice to make it n-type.

The outer electronic configuration of Zn and Cu are $3d^{10}$ $4s^2$ and $3d^{10}4s^1$ respectively. Hence, Zn can donate the extra electron if it replaces Cu in the lattice. The structural and optoelectronic properties of the pulsed dc magnetron sputter deposited undoped and Zn doped CuCl are discussed in the following sections.

3.3.2 Structure and morphology of undoped and doped CuCl

The CuCl:Zn films (samples) are deposited on glass and Si (100) substrates at room temperature by pulsed dc magnetron sputtering of CuCl/Zn targets containing approximately 0, 1, 2, 3 and 5 wt. % Zn. The actual atomic percentages of Zn in the aforementioned films have confirmed as 0, 1, 3, and 5 %, respectively using the EDX analysis with ± 0.2% accuracy.

In order to investigate whether the addition Zn makes any structural changes or create any new phase due to chemical reaction with CuCl, XRD analysis was performed in the undoped and Zn doped CuCl films. The crystalline quality of the CuCl:Zn films was examined and the corresponding diffraction peaks were indexed. These peaks were then compared with the actual powder diffraction patterns supplied by the International Centre for Powder Diffraction Data (ICDD) (table 3.3). In figure 3.4, plots (a), (b), (c) and (d) show the powder XRD pattern of CuCl samples with 0, 1, 5 and 3 % Zn respectively. All the measurements were carried out in identical experimental conditions. The Bragg diffraction patterns of the samples are in good agreement with the ICDD data for polycrystalline CuCl. All the samples show the cubic zincblende structure with lattice planes oriented along (111), (220)

and (311) directions with 2θ values ~ 28.5°, ~ 47.4° and ~ 56.3°, respectively, and preferential orientation along the (111) planes.

Table 3.2: ICDD powder diffraction data for CuCl. Intensities of different peaks are shown here corresponding to the values of their 2θ and (hkl) parameters.

2θ	Intensity (%)	h	k	l
28.5	100	1	1	1
33.02	8	2	0	0
47.43	55	2	2	0
56.29	30	3	1	1

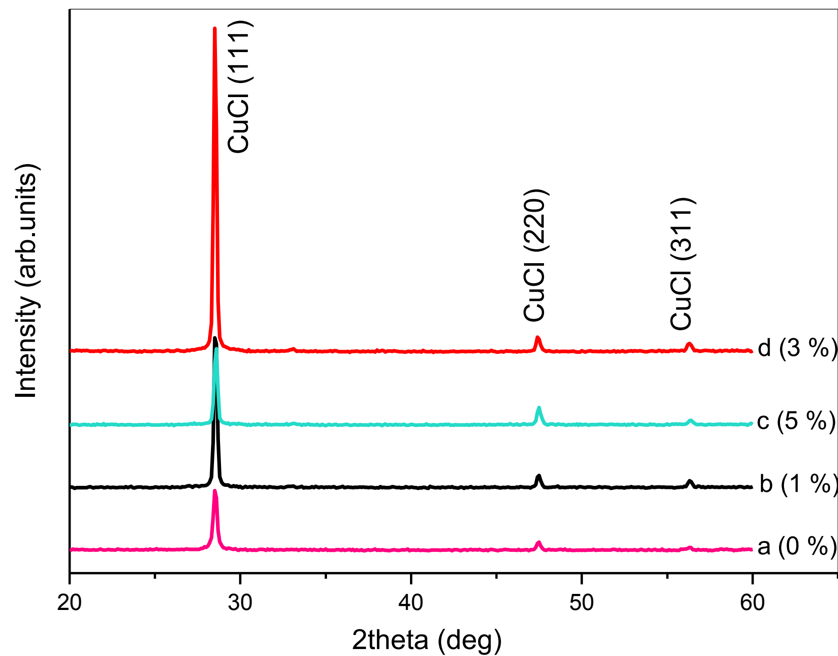

Fig. 3.4: X-Ray powder diffraction pattern for (a) 0 %, (b) 1 %, (c) 5 % and (d) 3 % Zn doped CuCl films deposited on Si (100) substrate. The patterns were recorded under identical conditions.

XRD patterns indicate no sign of structural deformity of CuCl by doping with Zn up to 5%; however, interestingly, an improvement in the orientation along the (111) direction is observed in samples with 1 and 3 % of Zn in comparison to that of undoped sample. The variation of the peak intensity ratio of CuCl (111) to the total intensity (sum of the intensities) of all orientations {CuCl (111) + CuCl (220) + CuCl (311)} (between 2θ values 20° and 60°) as a function of the Zn % is shown in figure 3.5. One observes that the (111) crystalline volume fraction (crystallinity) increases with Zn doping up to 3 %, and beyond that it tends to degrade.

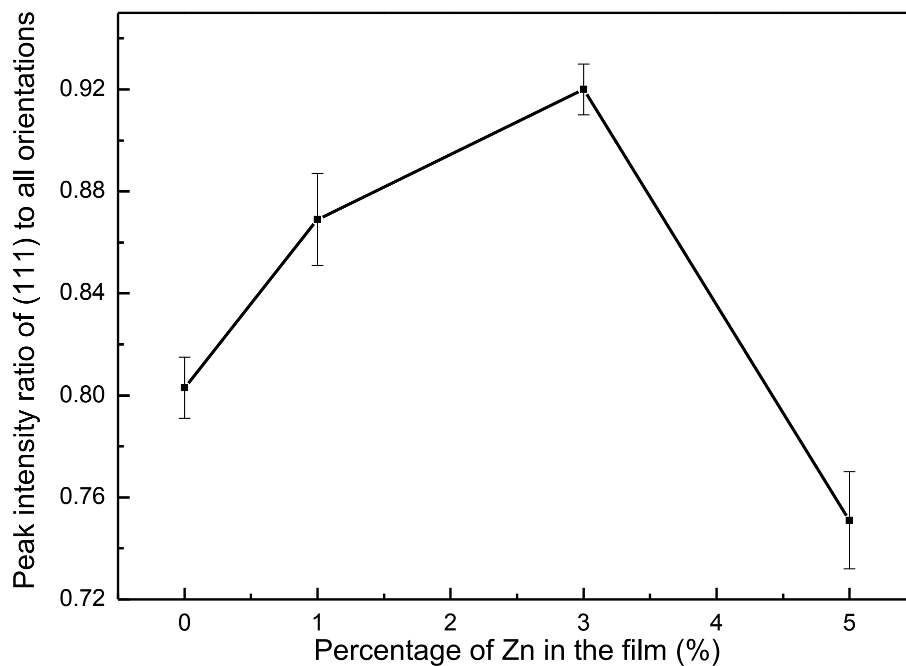

Fig. 3.5: Variation of (111) peak intensity to the total intensity of all orientations as a function of the % of Zn in the film. This plot is according to the XRD data in the fig.3.4

Generally, polycrystalline cuprous halide thin films are believed to contain numerous copper vacancies [65, 103-104]. The introduction of Zn is assumed to fill some of

the Cu vacancies in the CuCl crystal, thereby improving the crystallinity of the doped samples. The incorporation of Zn atoms could be facilitated due to the fact that the ionic radii of the Cu^{+} and Zn^{2+} ions in the tetrahedral co-ordination are equivalent with a value of ~ 60 pm [105].

Figure 3.6 illustrates the variation of the full width at half maximum (FWHM) of the CuCl (111) peak and the average crystalline size in accordance with the weight percentage of Zn in the target obtained from the X-ray diffraction analysis. The average crystalline sizes are calculated using the Scherrer equation,

$$d = \frac{0.9\lambda}{\Delta\theta \cos\theta_B} \qquad (3.1)$$

where λ, θ_B and $\Delta\theta$ are the X-ray wavelength, Bragg diffraction angle and FWHM of the CuCl (111) peak corrected for instrumental broadening respectively.

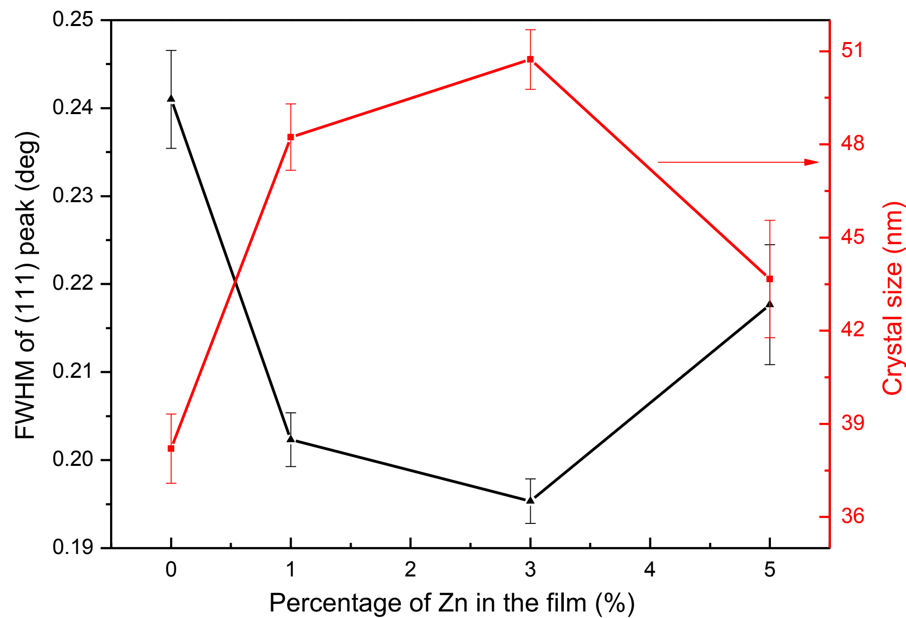

Fig. 3.6: Variation of FWHM of CuCl (111) peak and average crystal size of the CuCl: Zn film as a function of the percentage of Zn in the film. The crystal sizes were calculated using Scherrer equation.

Since the lattice mismatch between the Si (a_{Si} =5.43 Å) and CuCl film (a_{CuCl} =5.40 Å) is very small (~ 0.5%), we expect that the broadening effect due to strain is negligible in this case. The FWHM decreases from 0.24^o (undoped) to 0.18^o (3 % Zn doped) and again increases slightly to 0.2^o for 5 % Zn doping. This clearly indicates an improvement in the crystallinity of the CuCl film with the inclusion of Zn, and the maximum is achieved for 3 % doping. The average crystallite sizes of samples doped with 0, 1, 3 and 5 % Zn are calculated as approx. 37 nm, 47 nm, 49 nm and 44 nm, respectively. The minimum FWHM and the maximum peak intensity ratio of the CuCl (111) with respect to all orientations are observed for 3 % doped sample. Furthermore, the largest crystallite size is also noticed for the aforementioned sample. From the XRD results, one observes that the doping of CuCl films with 3 % Zn appears to be the optimum process and further increases in the Zn concentrations result in a reduction in the (111) crystalline volume fraction and crystalline size (5 % doped sample). The reduction in the crystal properties may be due to the segregation of dopants in the grain boundaries beyond a doping level of 3 %. This hypothesis is examined using SEM analysis of the appearance of non-uniform grains with irregular orientations.

SEM analysis was carried out on the doped and undoped films to investigate the influence of doping on the surface morphology of the films. SEM micrographs of the CuCl:Zn thin films are shown in figure 3.7, which indicates changes in the grain morphology as a function of Zn incorporation in the film. The images clearly show a slight increase in the grain size from the undoped to the 3 % Zn doped sample (average grain size varies from ~120 to ~180 nm for undoped to 3 % doped samples).

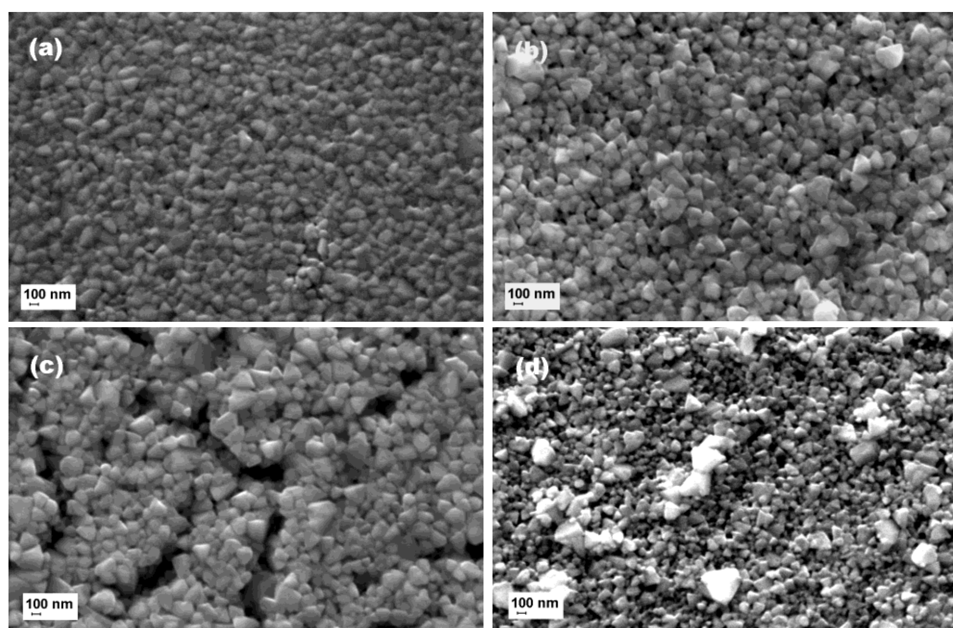

Fig. 3.7**:** SEM images of CuCl: Zn films with (a) 0 %, (b) 1 %, (c) 3 %, and (d) 5 % Zn in the film. All the films were deposited on Si substrate, and images were taken under identical conditions using 13 kV accelerating voltage.

The average crystalline sizes obtained from the SEM images are greater than those obtained from the Scherrer equation using XRD patterns. Similar results were reported by Natarajan *et al*. [43] in sputtered CuCl thin films using atomic force microscopy and XRD studies. The grains in the SEM images can be considered as a group of aggregated nanocrystallites. The SEM images of undoped, 1 and 3 % doped samples show almost homogeneous grain morphology, with uniform orientation of grains, while that of the 5 % doped one shows grains with irregular size and shape with different orientations. This is confirmed by the XRD pattern via a decrease in the peak intensity ratio of the CuCl (111) peak to total intensity of all orientations as shown in figure 3.5.

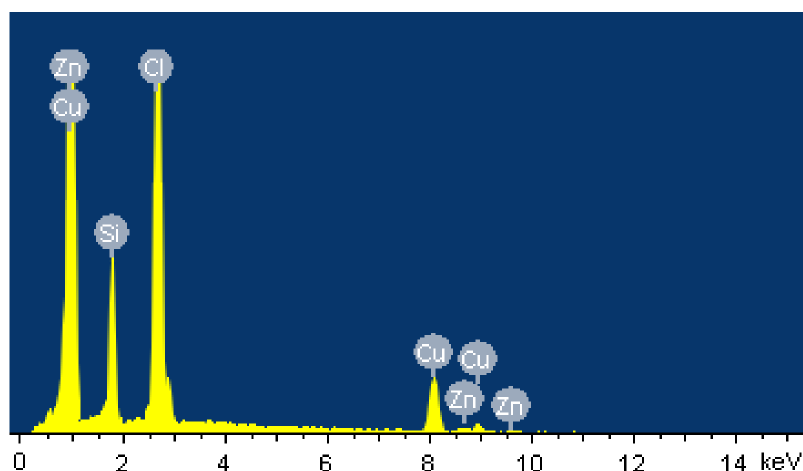

Fig. 3.8: EDX spectrum of a typical 3 % Zn doped CuCl film deposited on Si substrate. The accelerating voltage used for the EDX analysis was 13 kV.

The EDX spectrum of a typical 3 % Zn doped CuCl film is showed in figure 3.8. The measurement was carried out at an accelerating voltage of 13 kV. It clearly shows Zn signal in addition to the Cu and Cl. The Si signal is from the Si substrate underneath. One can see both Cu and Zn peaks overlapped around 1 keV. Again, no impurity elements were detected in the analysis.

3.3.3 Optical characteristics of doped films

3.3.3.1 UV-Vis spectroscopy

It is essential to ensure the optical quality of the doped films before using these for the optoelectronic device applications. Absorption properties of the undoped and the Zn doped CuCl films were investigated using UV-Vis absorption measurements. Films deposited on glass substrates were used for these measurements. The room temperature UV-Vis absorption spectra for the CuCl:Zn films is shown in figure 3.9.

Herein, the major peaks correspond to both high and low energy excitonic bands known as the $Z_{1,2}$ and Z_3 excitons, respectively. The $Z_{1,2}$ and Z_3 excitons are due to the coupling of the lowest conduction band state Γ_6 to both the uppermost valence band holes, Γ_8 ($Z_{1,2}$) and Γ_7 (Z_3), respectively [26, 61]. The $Z_{1,2}$ peak at ~ 372 nm (3.34 eV) and the shoulder Z_3 peak at ~ 379 nm (3.28 eV) are in good agreement with the previously reported absorption data for the undoped CuCl [102]. No significant alteration of the absorption properties of CuCl is noticed by doping with Zn.

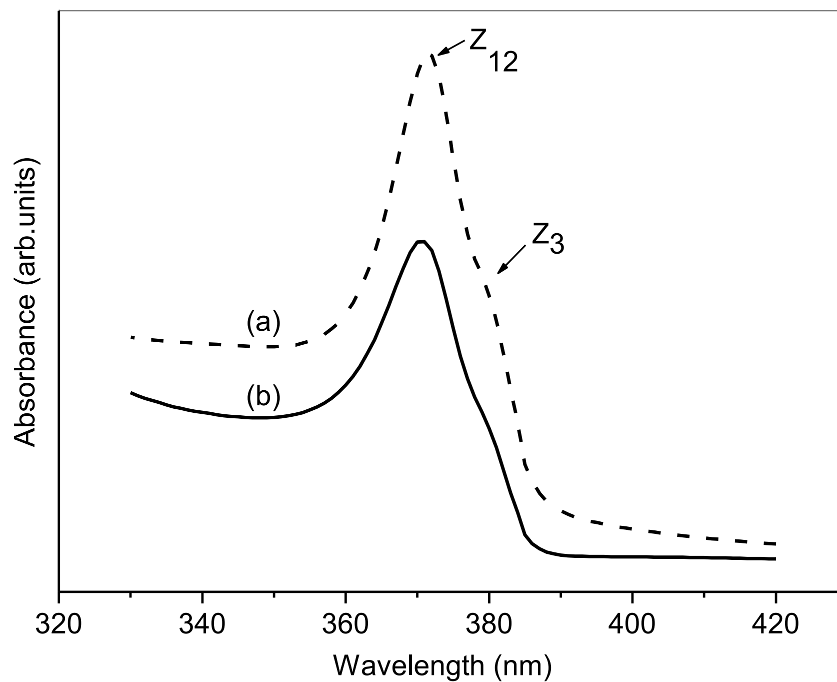

Fig. 3.9: Room temperature UV-Vis absorption spectra of (a) 3 % Zn doped CuCl and (b) undoped CuCl deposited on glass substrates.

3.3.3.2 Photoluminescence (PL)

Further optical characterisation of the films was carried out using room temperature and temperature dependant photoluminescence measurements. The PL measurements for all the samples (both doped and undoped) showed similar excitonic emissions at all temperatures. Figure 3.10 shows the PL spectrum of 3 % Zn doped sample measured at 80 K. It indicates the strong luminescent properties of the Zn-doped CuCl films. This graph clearly delineates four main peaks represented as Z_3 (~3.21 eV), I_1 (~3.19 eV), M (~3.17 eV) and N_1 (~3.14 eV), corresponding to the Z_3 free exciton, I_1 impurity bound exciton, M free biexciton and N_1 impurity bound exciton, respectively.

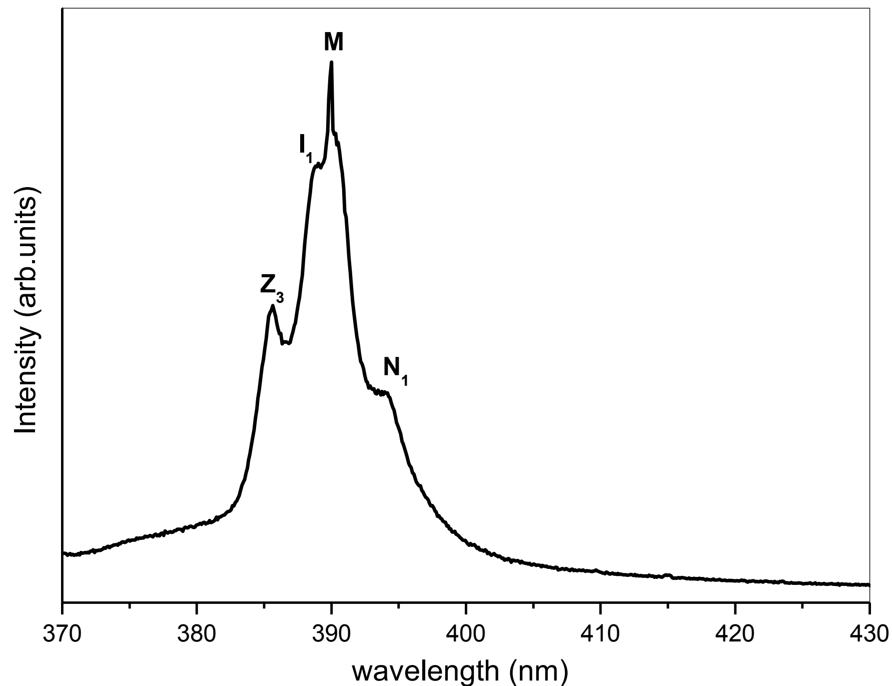

Fig. 3.10: PL spectrum of a typical 3 % Zn doped film at 80 K. The film was deposited on Si (100) substrate.

The impurity corresponding to the I_1 peak has already been reported as being due to a copper vacancy [106], the M free biexciton results from exciton-exciton collisions [26] and the N_1 peak originates from a biexciton bound to an impurity. These results are in agreement with the previously reported low temperature PL data of the undoped CuCl [101-102], indicating that the optical properties of the doped films are not compromised as a result of incorporation of Zn atoms at the doping levels mentioned.

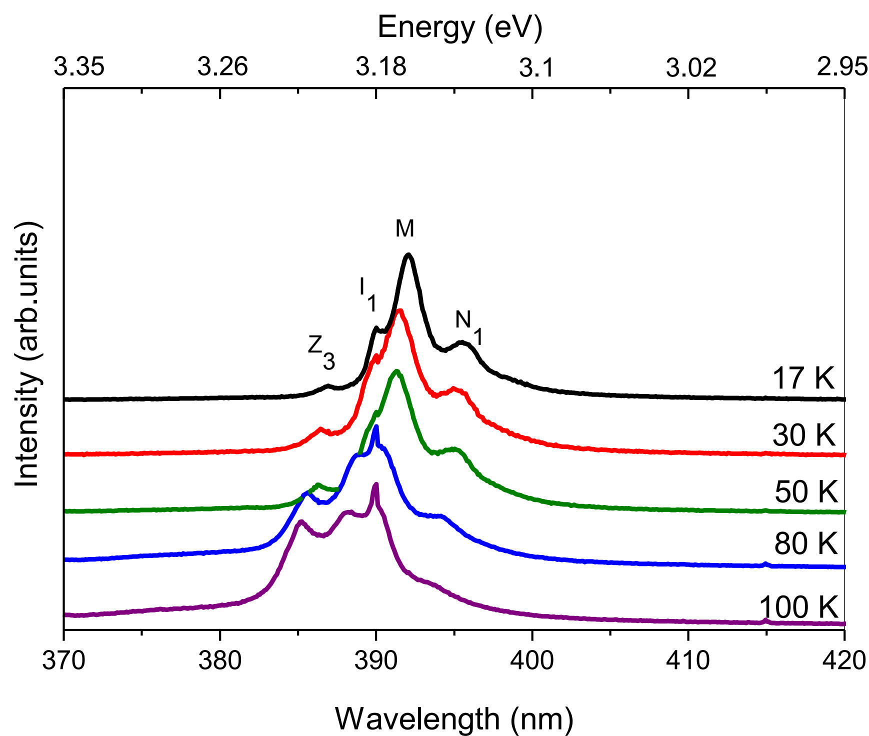

Fig. 3.11: Temperature dependant PL spectrum of a typical 3 % Zn doped CuCl films deposited on Si (100) substrate.

Figure 3.11 shows the temperature dependence of the PL spectrum of 3 % Zn doped CuCl sample. As the temperature increases, the rate of decrease of the peak intensities of I_1 and N_1 become higher compared to that of the Z_3 free excitonic peak intensity, and the spectra become dominated by the Z_3 peak above 100 K up to room

temperature due to the high free excitonic binding energy of CuCl. The influence of temperature on the Z_3 free exciton peak is manifested as a peak energy shift from ~ 3.205 eV to ~ 3.248 eV for a temperature increase from 17 K to room temperature. The increase in the energy value of the Z_3 free exciton as the temperature increases corresponds to an increase in the band gap energy and was theoretically and experimentally analysed for undoped CuCl samples by Garro *et al.* [107]. Analogous results in thin films and nanocrystals of CuCl have been reported previously [62, 108].

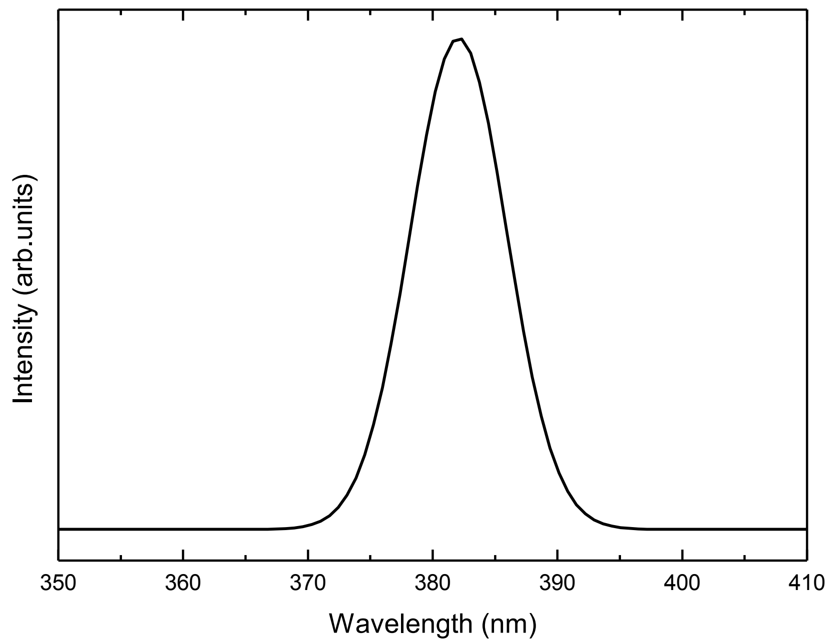

Fig. 3.12: Room temperature PL of the typical 3 % Zn doped CuCl sample.

The room temperature PL spectra of the Zn doped CuCl were also dominated by the Z_3 free excitonic peak, similar to that of the undoped CuCl. Room temperature PL spectrum of the 3 % Zn doped CuCl film is showed in the figure 3.12. The FWHM

of the PL peak obtained using the Gaussian fit was nearly 9 nm, which shows the good optical quality of the doped film.

3.3.4 Electrical properties of doped films

The electrical properties are the key features which determine the suitability of the films for pn-device applications. Hall measurements were performed to investigate the electrical properties of the undoped and the doped CuCl films. Room temperature Hall effect data for the Zn doped CuCl samples measured in the van der Pauw configuration are shown in figure 3.13. Hall measurements were not possible with the undoped CuCl, due to the high resistivity of the sample.

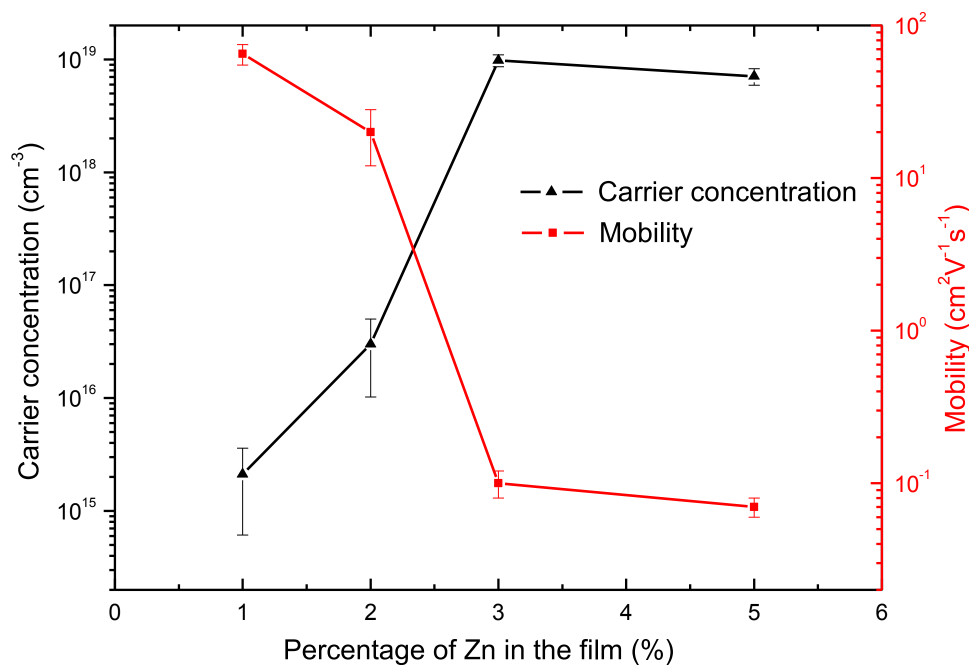

Fig. 3.13: Variation of carrier concentration and mobility as a function of the % of Zn in the target measured using Hall measurement set-up. Films deposited on glass substrates with gold electrodes on top of it were used for the measurements.

The presence of mixed conduction mechanisms was observed for 1 % Zn doped sample: both p-type and n-type conductivities with a relatively lower n-type carrier concentration of the order of ~10^{15} cm^{-3}. This could be explained by dopant compensation via the simultaneous existence of both types of conductivity, i.e. electron conduction due to the inclusion of Zn in the Cu vacancies and hole conduction due to the well known naturally occurring Cu vacancies in the undoped CuCl. Due to the fluctuations in the data for the 1 % doped sample, we included the results for an additional sample developed by the doping of 2 % Zn as well. The doped films (with Zn % > 1) consistently showed n-type conductivity with an increase of carrier concentration from 3.01±1.99 x10^{16} cm^{-3} to 9.8±1.2 x10^{18} cm^{-3} for 2 % and 3 % Zn doped samples respectively, and then slightly decreases to 7.1±1.2 x10^{18} cm^{-3} for 5 % doping. The slight decrease in the carrier concentration of 5 % doped sample with respect to the 3 % doped one is assumed to be due to the fact that relatively fewer Zn atoms can contribute to the conduction, and instead can segregate to the grain boundaries beyond a particular concentration (3 %). A similar reduction in carrier concentration of Al doped ZnO films were reported by Kim et al. [109]. As one expects, the Hall mobilities of the doped films were found to decrease as the Zn % increases. Mobility values of 20±8 $cm^2V^{-1}s^{-1}$, 0.1±0.02 $cm^2V^{-1}s^{-1}$ and 0.07±0.01 $cm^2V^{-1}s^{-1}$ were deduced for 2, 3 and 5 % Zn doped samples, respectively. In a simple form, the Hall mobility may be expressed in terms of impurity scattering mobility μ_i and grain boundary scattering mobility μ_g as follows:

$$\frac{1}{\mu_h} = \frac{1}{\mu_i} + \frac{1}{\mu_g} \qquad (3.2)$$

The sharp decrease in the mobility from 2 % to 3 % Zn doped samples can be attributed mainly to the impact of increased impurity scattering. The presence of grain boundaries and trapped interface charges in semiconductors results in inter-grain band bending and potential barriers which are well known to cause a considerable reduction in the resultant Hall mobility [110]. A further reduction in the mobility of 5 % doped sample in comparison to the 3% doped one may be ascribed to be the combination of both impurity scattering and grain boundary scattering mechanisms as the presence of more grain boundaries was observed in the SEM image of 5 % doped sample (see figure 3.7(d)).

The variation of resistivities of the samples is illustrated in figure 3.14. A value of 250 Ω cm was previously reported as the room temperature resistivity for undoped CuCl films using 4 point probe measurement [101]. The resistivities of the samples decrease to a minimum value of ~ 6 Ωcm for the 3 % doped sample, and increase to ~ 11 Ωcm for 5 % doping. Obviously, the reduction of resistivity of 3 % doped sample is due to higher carrier concentration while the slight increase in resistivity of the 5 % doped sample is due to a slight reduction in carrier concentration perhaps combined with the effect of increased grain boundary scattering as explained earlier.

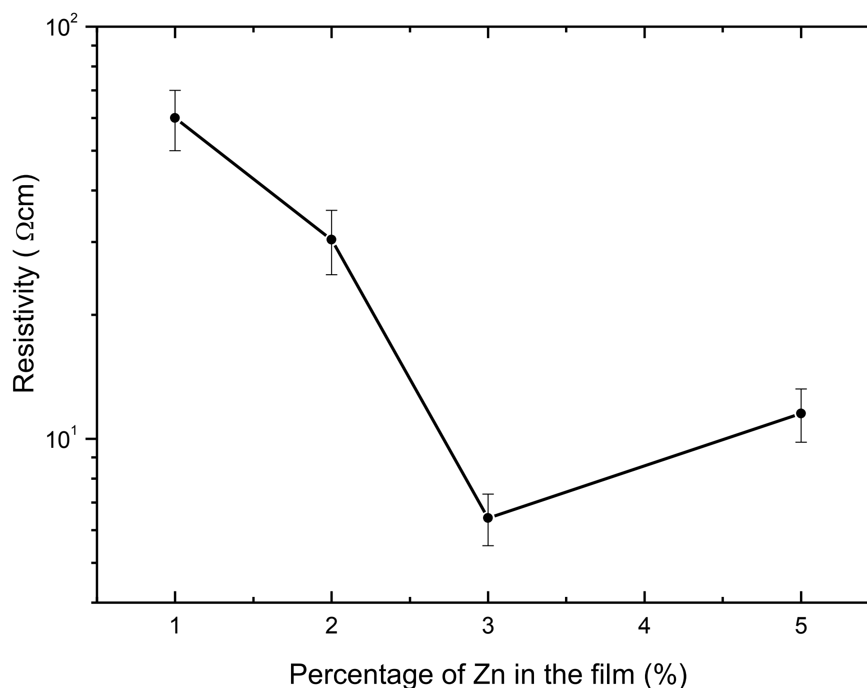

Fig. 3.14: variation of the resistivity of the CuCl:Zn films as a function of the % of Zn in the film

The electrical measurements confirm the efficacy of pulsed dc magnetron sputtering as a means of incorporating Zn in to the CuCl crystal lattice. The substitutional Zn leads to optimal carrier concentrations and resistivities for 3 % Zn doping, among the samples studied.

3.4 Summary

A reliable method for the development of n-type CuCl thin films using pulsed dc magnetron sputtering has been presented in this chapter. Hall effect measurements consistently confirmed that the controlled incorporation of Zn atoms in the cuprous chloride crystals resulted in n-type conductivity CuCl films. The resistivity of the Zn doped CuCl film was found to decrease by more than an order of

magnitude compared to the undoped CuCl film with an average maximum carrier concentration of ~ 9.8×10^{18} cm^{-3} and a minimum average resistivity of ~ 6 Ωcm for 3 % Zn doped samples. XRD, SEM and temperature dependent photoluminescence measurements confirmed that the incorporation of Zn atoms into CuCl has no deleterious impact on the structural and luminescent properties of the doped films in comparison with the undoped films. One can conclude that, it is possible to deposit an n-type CuCl film with good crystal quality and luminescent property and with resistivity, electron concentration and mobility values ~ 6 Ωcm, ~ 9.8×10^{18} cm^{-3} and ~ $0.1 cm^2V^{-1}s^{-1}$, respectively, by 3 % doping of Zn.

Chapter 4

Photoemission spectroscopic study of Zn doped n-type CuCl

4.1 Introduction

An elaborate description on the development, structural and optoelectronic characterizations of the Zn doped CuCl films have been discussed in chapter-3. As part of the investigation of the conduction process in the doped samples, it is essential to probe the influence of Zn doping on the electronic structure of CuCl. In this chapter we use photoemission spectroscopy (PES) to understand the electronic properties of the Zn doped copper chloride thin films. PES provides important information on the chemical bonding, ionic state and the hybridization of the metal and chloride species and the influence of dopant on the electronic structures. Both valence and core levels show the fingerprint of the electronic structure. The features of the core levels and the valence band of CuCl are discussed in this chapter as a function of doping of Zn.

CuCl is a tetrahedrally coordinated I-VII compound semiconductor having a valence band originating from filled d^{10} shell of Cu^+ ion and the s^2p^6 configuration of Cl^- ion [61]. Interestingly, modification of physical properties of this material occurs due to the strong *p*-*d* hybridization [61]. For example, (1) it exhibits non-linear optical properties useful for the applications like light modulation or generation of

higher harmonics. (2) Spin-orbit splitting of edge exciton is reversed compared to that of other zinc blende materials. (3) Bulk moduli are extremely small compared to their isoelectronic neighbours.

There are several reports on the edge exciton of CuCl starting from several decades ago [111-112]. Later, photoemission studies have been reported to give a clear idea about the position of the *d*-levels and to derive approximate partial *p* and *d* densities of states in the valence band region [54-56, 113-118]. The electronic energy band structure of CuCl has been investigated by several researchers on the basis of the studies on ultraviolet absorption spectra [35, 119], X-ray photoelectron spectra [114] and soft X-ray emission and absorption spectra [120]. The Kβ- emission and K-absorption of Cl in CuCl have been discussed in relation to the energy band structure by C. Sugiura [121]. He confirmed that, the upper valence band of CuCl arises mainly from the 3*d* state of Cu and the lower band primarily from the 3*p* state of Cl. The low- energy part of the conduction band arises from the 4*s* state of Cu [121]. Van der Laan *et al*. obtained information about the electronic structure and the energy gap by comparing the XPS spectrum of the valence band of CuCl with band structure calculations [122]. Furthermore, density of valence states of cuprous halides has been studied by Goldmann *et al*. [56]. The formation of satellites was reported when the emission of a 2*p* photoelectron takes place in parallel with a valence band-conduction band excitation in CuCl [123]. Later, it was proved by D. C. Frost *et al*. that, the satellites are the features of the cupric species present in CuCl [124].

However, there is no report on the influence of Zn doping on the electronic structure of CuCl. In order to verify the chemical bond formation and electronic structure of this material in detail, we used soft x-ray absorption and high resolution

photoemission spectroscopy to understand the element specific conduction band density of states and to study the valence and core level photoemission of various Zn doped (1, 3 and 5 %) γ-CuCl samples. PES is a widely used surface analysis technique and could be a powerful tool to understand the influence of Zn dopant on the electronic properties of CuCl. Our findings on the electronic and optical properties are essential for the step towards the realization of CuCl based light emitting devices.

4.2 Experimental details

Thin films of CuCl:Zn were prepared by pulsed dc magnetron sputtering of a CuCl/Zn target, as discussed in chapter-3. Films deposited on Si substrates were used for the XPS studies. The substrates were cleaned before deposition using cleaning methods discussed in the previous chapter. As it is well known that, the CuCl samples are very sensitive to moist air, the deposited samples were transferred very carefully through vacuum desiccators in to the preparation chamber of the photoemission spectroscopic measurement system. All films are of 350±20 nm thick as measured using Profilometer.

Photoemission spectra were obtained at normal incidence geometry with a Scienta SES 200 analyser [125]. The total energy resolution is 0.1 eV as obtained from clean gold. All the obtained spectra were referenced to gold 4*f* and 4*d* levels. All experiments were performed under ultrahigh vacuum conditions in order to avoid any contamination from the atmosphere.

4.3 Results and discussion

4.3.1 Effect of Zn doping- An overview

The influence of Zn doping on the structural, morphological and optoelectronic characteristics of CuCl is extensively discussed in chapter 3. It is observed that Zn doping improves the crystallinity and increase grain size of CuCl up to a certain doping level (3%) [126]. The lattice parameter corresponding to the undoped and 5 % Zn doped CuCl film were calculated from the (111) peak position as 5.418 Å and 5.4 Å respectively. However, there was no noticeable variation of the lattice constant up to a Zn doping of 3 %. Similar kind of decrease in the lattice constant was reported by O'Reilly *et al.* in the case of $ZnCl_2$ doped CuCl [101]. Again, the variation of resistivity, carrier concentration and carrier mobility of the Zn doped CuCl films have studied and published [126]. From the data based on the doped films studied, 3 % doping is observed to be the optimum. The film corresponding to the above doping percentage shows better structural, morphological and optoelectronic properties along with n-type conductivity.

4.3.2 Zn *2p* core level spectra in the doped films

Before starting the analysis of the Zn doped CuCl films, it is essential to investigate the oxidation state and chemical environment of Zn in the film. Core level X-ray photoelectron spectroscopy was used to determine the composition of the film. Since the core-level peak area is directly related via the photoemission cross section to the number of atoms present, the ratio of the cross-section corrected core-level peak areas allows one to determine the stoichiometry of the film without the need of

models or fitting parameters [127]. There was no sign of the Zn 2*p* peak in the undoped CuCl, indicating the absence of Zn in the undoped film.

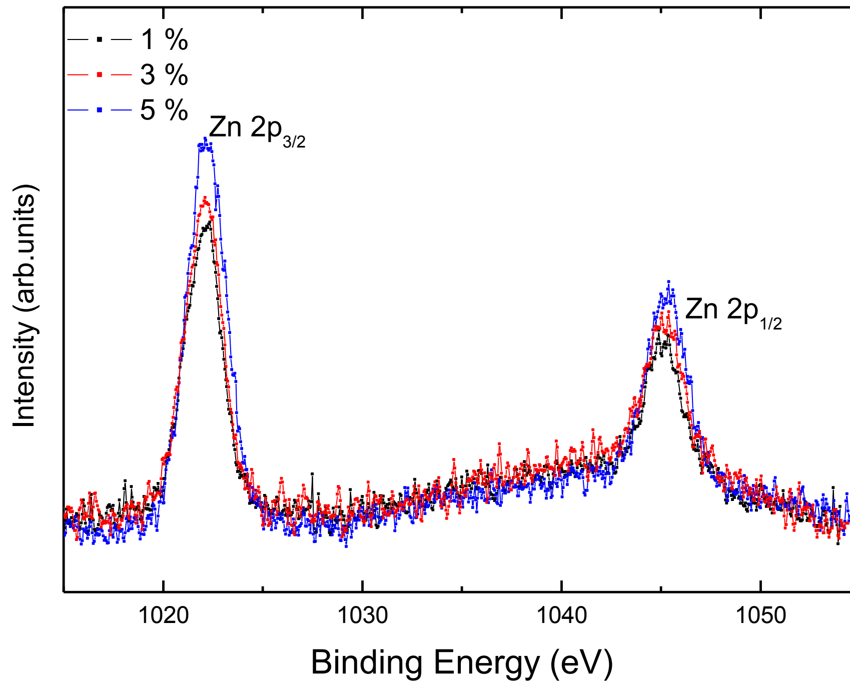

Fig. 4.1: Zn *2p* core level spectra of the CuCl as a function of the Zn doping. The peak around 1022 eV represents Zn $2p_{3/2}$ and that around 1045 eV represents Zn $2p_{1/2}$.

Figure 4.1 shows the series of Zn *2p* core level spectral peaks corresponding to different doping percentages of Zn (1%, 3%, and 5%) in the CuCl films. The peaks at a binding energy of 1022±0.1 eV correspond to the Zn $2p_{3/2}$ and those at 1045±0.1 eV indicate the Zn $2p_{1/2}$ spectral peaks. It is observed from the plot that, as the concentration Zn in the CuCl film increases from 1-5 %, there is a corresponding increase in the intensity of the Zn *2p* peaks. However, the slight discrepancy between the Zn *2p* peak areas observed from the graph and the actual percentage of Zn in the film is due to the fact that, PES collects information from the top few nanometres of the film, rather than analysing the whole film. We also observed a reduction in the

FWHM of the Zn *2p* peak from 2.04 to 1.88 eV as the Zn % increase from 1 to 3. This is attributed to the improvement of crystal quality and lesser defects in the films as a function of doping up to 3 %. This is also in agreement with the results obtained using the XRD and SEM studies discussed in chapter 3 [126]. However, no change in the separation of the spin orbit splitting is observed between the metallic Zn and the substituted Zn in the film. Furthermore, there was no noticeable shift observed between the core levels of the metallic Zn and the substituted Zn in the film [128].

4.3.3 Effect of Zn doping on the Cu *2p* core level spectra

It is very interesting to investigate the influence of Zn doping on the Cu *2p* core levels of CuCl. There are several reports on the Cu core level spectra in CuCl [123-124, 129]. At first Novakov reported the existence of satellites of 2*p* bands in CuCl [123], later D. C. Frost *et al.* noticed the presence of satellites only in cupric compounds, not in cuprous compounds. He observed intense satellites in the 2*p* and 3*s* band of the cupric compounds, and these demonstrated to be very useful in studying the influence of the coordination metal-ligand bonds [124, 127].

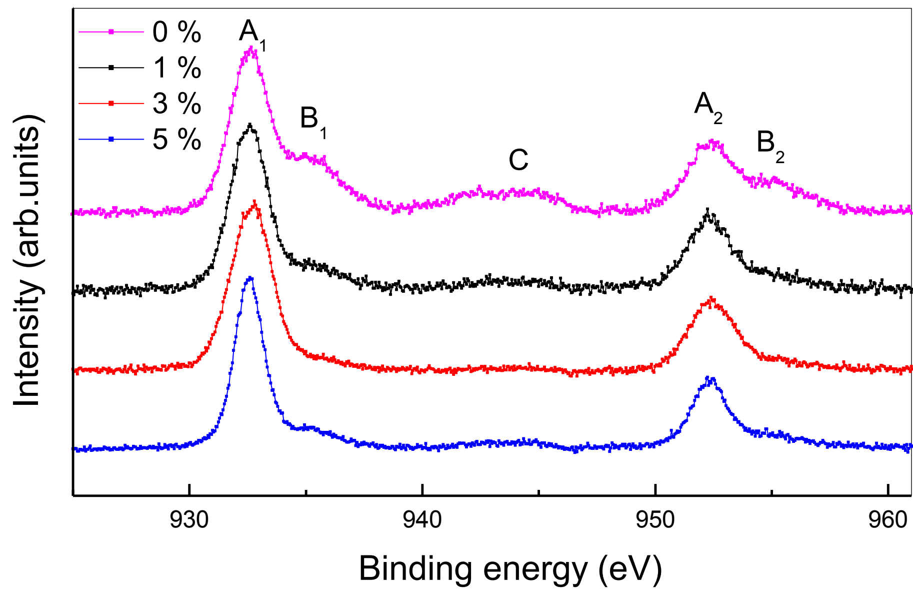

Fig. 4.2: Cu *2p* core level spectra of the undoped and 1- 5 % Zn doped CuCl films. Cu $2p_{3/2}$ (A_1), Cu $2p_{1/2}$ (A_2), shoulder (B_1 and B_2) and the satellite (C) peaks are illustrated here.

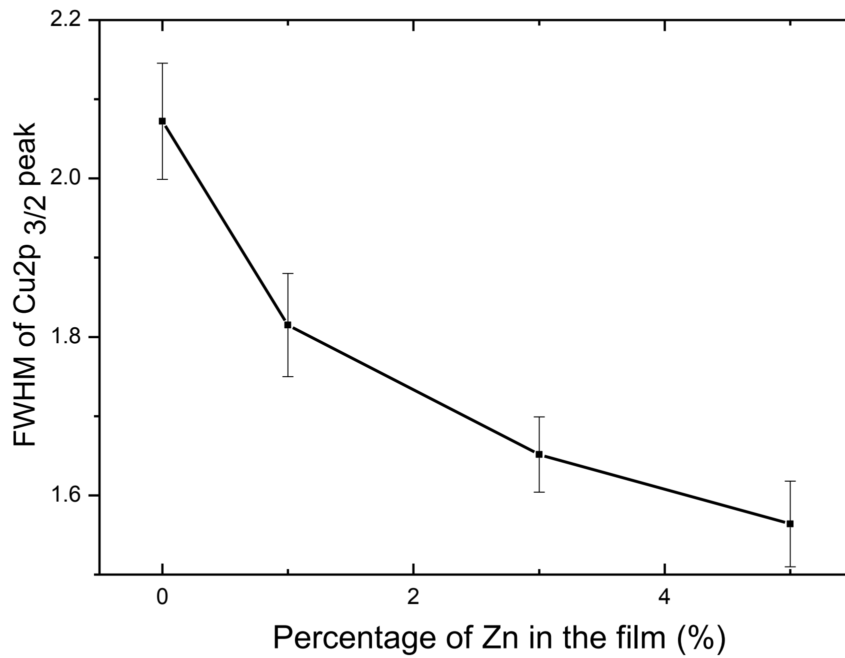

Fig. 4.3: The variation of the full width half maximum of the Cu $2p_{3/2}$ line as a function of the percentage of Zn in the film.

Figure 4.2 shows the Cu $2p_{1/2}$ and Cu $2p_{3/2}$ core level spectra of undoped and the Zn doped CuCl samples (A_1 and A_2). The binding energies correspond to the $2p_{3/2}$ and $2p_{1/2}$ are 932.6 eV and 952.4 eV respectively. These data are in agreement with the previous reports for CuCl [130]. Furthermore, there is clear evidence of satellite peaks in the undoped sample (C), which appears as low intensity peaks around 942 eV and 944.8 eV. These satellites are reported to be due to the presence of cupric species created by the exposure of the film to moisture or oxygen [124, 127]. Van der Laan *et al*. have already reported the presence of satellite peaks around the same region for the $CuCl_2$ [131]. They reported that the satellites are due to the interaction between the core hole and the valence electrons ensuing in a change in the potential seen by the valence electrons upon the creation of the core hole. The intensity of these satellites reduces as the Zn % in the film increases, and almost no sign of satellites for the 3 % Zn doped sample. This could be attributed to the disappearance of cupric species under the influence of Zn doping [127]. Moreover, shoulder peaks are also observed on the higher binding energy side of the *2p* peaks, about 2 eV higher than that of the main peaks. Hence, these shoulder peaks can also be considered as due to the presence of cupric species ($CuCl_2$), which are reported to have binding energies at around 934.6 eV (Cu $2p_{1/2}$) and 954.4 eV (Cu $2p_{1/2}$) [131]. The aforementioned peaks also have the analogous tendency with that of the satellite peaks. Similarly, the appearance of shoulder peaks close to the actual metal peaks was reported by Kishi *et al*. [132] in the case of the reaction of the evaporated metal films of Pd and Au with chlorine gas. Moreover, D. C. Frost *et al*. reported the splitting of the main peaks of $2p_{1/2}$ and $2p_{3/2}$ as a result of the chemical shift of 1-2 eV between Cu^{++} and Cu^{+}, which occurs due to the existence of impurities of different oxidation states [124]. Figure 4.3 represents variation of full width at half

maximum (FWHM) of the Cu $2p_{1/2}$. It is clear from the plot that, FWHM of the $2p_{1/2}$ peak has the maximum value for the undoped sample. As the percentage of Zn in the film increases, the FWHM decreases. The broadening effect of the core level peak has also been reported in association with the appearance of satellite peaks [89]. This can also be considered as due to the presence of cupric species in the undoped sample, which disappears with Zn doping.

4.3.4 Effect of Zn doping on the Cl *2p* core level spectra

The influence of Zn doping on the Cl 2*p* core level of CuCl is also analysed. The Cl $2p_{3/2}$ and $2p_{1/2}$ spectra of the undoped and Zn doped CuCl samples are presented in figure 4.4. These *2p* lines are separated by about 1.5 eV from each other. The intensity of the $2p_{1/2}$ peak is relatively higher for the pristine sample compared to the doped samples. Here, the increased intensity of the higher binding energy peak in the pristine sample can be explained due to the presence of traces of chlorine species in the form of $CuCl_2$ in addition to the presence of chloride ions (Cl^-) in the form of CuCl [133-134]. Analogous results in the higher binding energy Cl *2p* peak have been reported in the case of gold and palladium chlorides [132]. Furthermore, the occurrence of the higher binding energy tail is detected in the case of the undoped sample (marked using a blue circle in the figure 4.4).

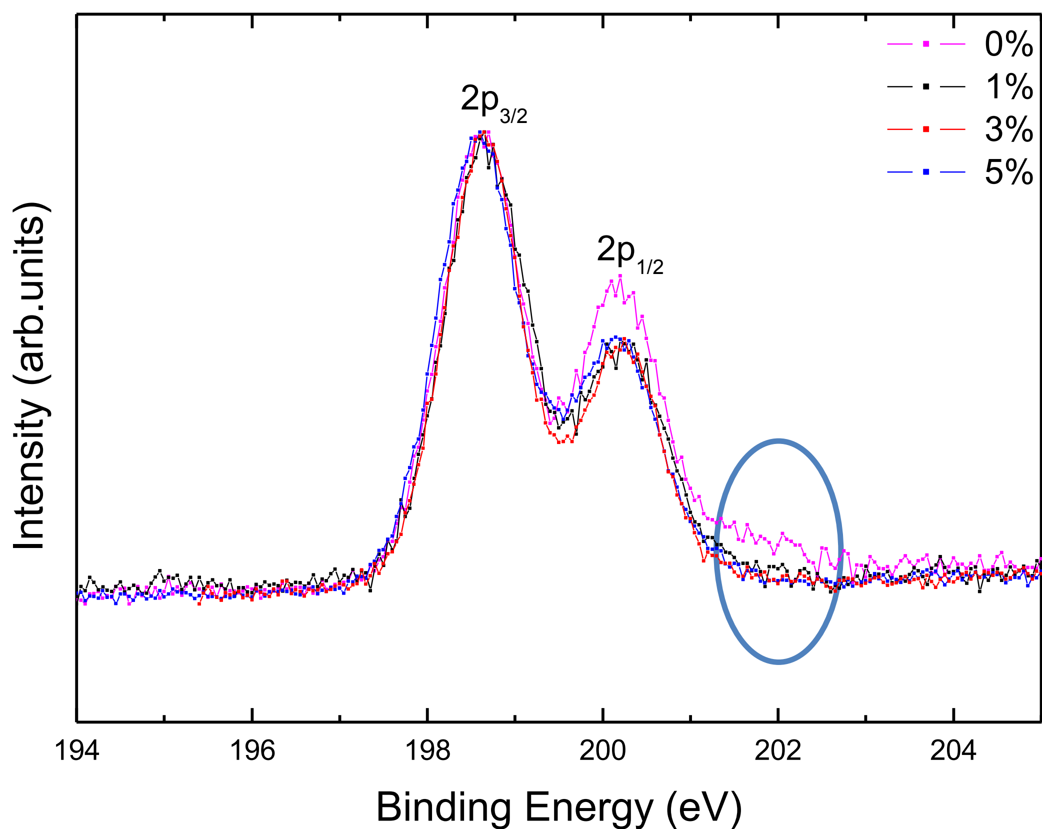

Fig. 4.4: Cl 2*p* spectra of the undoped CuCl and the 1, 3 and 5 % Zn doped samples. The lower binding energy peak corresponds to the $2p_{3/2}$ line and the higher binding energy one corresponds to the $2p_{1/2}$ specral line.

This could be attributed to the presence of the thicker $CuCl_2$ layer in the pristine sample [132]. Both of the Cu 2*p* and the Cl 2*p* core level spectra suggests that undoped CuCl contains trace amount of Cu^{2+} species, along with the major Cu^{+} species. As it is doped with Zn, the amount of Cu^{2+} species reduces and becomes almost absent for the 3 % Zn doped sample.

4.3.5 Influence of Zn doping on the valence band of CuCl

So far, there are quite a few reports on the valence band of CuCl [114, 56, 122, 131]. The valence band spectra of the undoped and the Zn doped CuCl samples are presented in figure 4.5. The spectrum mainly consists of 2 bands, the upper band around 3 eV is mainly Cu-3*d* character and the lower band around 6 eV is of Cl-3*p* character [122]. According to the band structure calculation reported by Van der Laan *et al.*, there are two major bands contributing to the density of states of the upper band. One is an almost non dispersive band L_3-Γ_{12}-$X_{2,3}$ at 3.2 eV and the second one is a broader band $L_{1,3}$-$\Gamma_{1,5}$-X_{15} at 3 eV at L, X, and 2 eV at Γ. Where, Γ, L, and X are respectively the centre of the Brillouin zone at k=o, edge of the first Brillouin zone of k-space in the <111> direction and edge of the first Brillouin zone of k-space in the <100> direction and the subscripts represent the states associated with the respective points. This would explain the asymmetry in the upper band spectrum. Moreover, the asymmetry of the lower band towards the higher binding energy was also explained using the band structure evaluation [122].

It is well known that, CuCl has a strong hybridization of metal *d*- orbital and halogen *p*- orbital, which distinguishes it from other zincblende semiconductors, leading to a small spin orbit splitting at the top of the valence band [35, 135]. Experimental results showed that the admixture of Cu *d* states to Cl *p* states has a vital role in the structure of the valence bands. We observed that, the distance from the upper band to the Fermi level is nearly 2 eV. This implies that the energy gap is no less than 2 eV, which is in agreement with the reports of Van der Laan *et al*. [122].

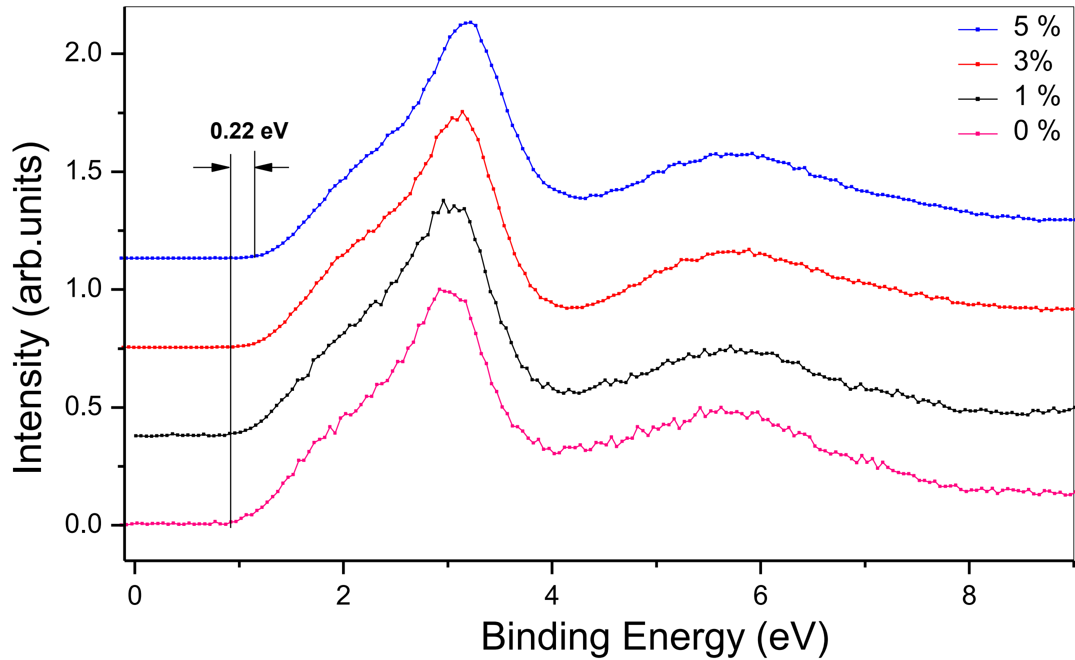

Fig. 4.5: Valence band spectra of CuCl as a function of the percentage of Zn doping. The zero binding energy point corresponds to the Fermi energy, E_f.

Furthermore, both the valence band edge and the peaks in the valence band of CuCl show shifts towards higher binding energy with doping of Zn. This can be explained by the filling of the conduction band of CuCl as it is doped with Zn. A maximum shift of 0.22 eV is achieved for the 5 % Zn doped sample with respect to the undoped one. According to the resistivity data presented in chapter 3, as the % of Zn in the CuCl film increases, the resistivity decreases by an order of magnitude and reaches a minimum value of ~ 6 Ω cm for the 3 % Zn doped sample. The decreasing trend of the resistivity of the doped films is in agreement with the shifting of the valence band edge towards the higher binding energy side. The slightly higher value of the resistivity observed in the 5 % Zn doped film can be explained due to presence of

slightly smaller, irregularly oriented grains with different sizes and shapes (fig 3.7 (d)). The smaller grains will increase the carrier scattering thereby increase resistivity slightly, for the aforementioned sample.

4.3.7 Summary

The influence of Zn doping on the electronic structure of CuCl is investigated using XPS analysis. Studies on the Cu *2p* core level spectra of the samples revealed the presence of satellite peaks and shoulder peaks mainly in the undoped CuCl film, which indicates the existence of trace amounts of cupric species in the undoped CuCl. This is again verified by the observation of the increased intensity of the higher binding peak of Cu *2p* core level. The disappearance of the cupric species under the influence of Zn doping is also confirmed. The increased intensity of the higher binding energy peak as well as the occurrence of the higher binding energy tail in the Cl *2p* core level supports the presence of cupric species in the pristine sample. This effect is also reduced and disappeared due to the doping of Zn. The shifting of valence band of CuCl towards the higher binding energy side is observed as a result of Zn doping due to the filling of the conduction band. A maximum shift of 0.22 eV is noticed for the 5 % Zn doped CuCl film. More experiments need to be performed in order to understand the complete electronic structure of these novel films.

Chapter 5

Growth and characterisation of p-type CuBr

5.1 Introduction

In order to develop CuBr for future optoelectronic applications, it is important to concentrate on the studies of doping of this material to improve the electrical conductivity. CuBr is naturally a p-type mixed ionic-electronic semiconductor material [79, 136]. To date, there are several reports on the electrical properties of CuBr. Desvals *et al.* investigated the electrical properties of the two-phase mixtures of CuBr and alumina using impedance spectroscopy [137]. They observed an enhancement of electrical conductivity for these samples compared to pure CuBr. Furthermore there are reports on the studies of electrical properties of CuBr between 20 and 430°C by impedance spectroscopy [136]. Safadi *et al.* conducted four-point conductivity experiments to separate bulk and interfacial effects in CuBr [138]. A change from predominant ionic conduction above 260 K to electron hole conduction below that temperature was observed by Tortet *et al.* [139]. So far, there are very few reports on the semiconducting properties of CuBr [82, 99]. P-type conductivity of CuBr can be explained either by acceptor doping due to oxygen or by a copper

deficiency $Cu_{1-\delta}$ Br [140]. Mott-Schottky analysis of polycrystalline CuBr by Knauth *et al*. has reported this material to be p-type with an accepter concentration of (2±1) $\times 10^{16}$ cm^{-3} [99]. Furthermore, Hall effect and capacitive measurements on the polycrystalline CuBr have been investigated by Knauth *et al.*; according to their studies oxygen impurities can increase the hole concentration and hence can act as an effective acceptor for CuBr [82]. They reported a hole concentration and mobility of (9±2) $\times$ 10^{17} cm^{-3} and (0.4±0.1) $cm^2V^{-1}s^{-1}$ respectively. The inclusion of oxygen in their Hall samples occurred due to the exposure of the samples to the atmosphere. Again, it has been mentioned that, the incorporation of oxygen was mainly near the surface, because of the very slow oxygen bulk diffusion at room temperature [82].

Although, we tried to deposit CuBr films by pulsed dc sputtering technique at the beginning of the studies, it was difficult to deposit these films from high purity CuBr target using pulsed dc sputtering due to the poor thermal conductivity of the target. Hence we moved towards the thermal evaporation techniques. Present chapter deals with the deposition of thin film CuBr on to Si and glass substrates using the thermal evaporation technique followed by the exposure to a combination of oxygen and argon plasma to improve the oxygen diffusion, thereby doping the CuBr films to p-type. The influence of plasma exposure time on the resistivity, hole mobility and hole carrier concentration of the CuBr film has been investigated. The structural, morphological and optical properties of the doped films have also been explored.

5.2 Experimental details

CuBr thin films of thickness 380±10 nm (thickness was measured using the thickness monitor and later on verified using AFM) were deposited by the thermal evaporation of CuBr powder (99.999%) on to Si and glass substrates using an

Edwards 306A vacuum evaporator with a base pressure of ~5×10^{-7} mbar. Prior to deposition, the substrates were cleaned using acetone, methanol and de-ionised water in an ultrasonic bath. The films of CuBr on Si and glass substrates were then transferred in to a plasma chamber (Oxford Instruments-RIE), in which a mixture of O_2 and Ar (4:1) was used as the working gas at an RF power and chamber pressure of 300 W and 6.6×10^{-2} mbar respectively. The films were then exposed to the oxygen plasma for different time intervals (1, 3 and 5 min) in order to dope it with oxygen to make it p-type. The plasma parameters used for the oxygen doping of the CuBr films are shown in the table 5.1. These parameters were selected to achieve maximum conductivity with minimum exposure time of the films. Films deposited on glass substrates were used for the UV-Vis absorption studies and for the Hall measurements (HL 5500 PC) in the Van der Pauw configuration. The resistivity, carrier concentration and carrier mobility of the oxygen plasma exposed films were examined using Hall measurements. Ohmic contacts were made by an evaporated layer of gold. Films deposited on Si substrates were used for the PL, SEM, AFM and SIMS analysis.

Table 5.1: Values of the Plasma parameters used for the oxygen doping of the CuBr films.

Process parameters	Used values
Flow rate of oxygen (SCCM)	80
Flow rate of Argon (SCCM)	20
Chamber pressure (mbar)	6.6×10^{-2}
Power (W)	300

5.3 Results and discussion

5.3.1 Structural and morphological properties

The structural properties of the as-deposited and the oxygen plasma exposed films were investigated using X-ray diffraction analysis. The diffraction patterns of the films deposited on the Si (100) substrates are showed in figure 5.1. All films show preferential orientation along the (111) direction corresponding to a 2θ value of ~ 27.1 °. Peaks appearing at ~ 45 ° and ~ 53.3 ° correspond to the (220) and (311) planes of CuBr. These observed peaks are in good agreement with the ICDD data on CuBr given in table 5.2 [141]. There was an indication of a small intensity peak around 25.3° in some evaporated samples. This is assumed to be due to the presence of trace amounts of wurtzite phase (β-phase) of CuBr, which has a (100) orientation at around 25.3°. This would be due to the effect of small fluctuations in the current through the heating element during the evaporation of CuBr, which will cause variation in the temperature and there by formation of a higher temperature phase. The aforementioned assumption can be supported by the absence of wurtzite phase observed in the sputtered CuBr samples. The presence of a small amount of wurtzite phase has also been reported by M. Cardona in the case of thermal evaporated thin films [142].

Table 5.2: Powder diffraction data file for CuBr according to the JCPDS card number 06-0292.

2θ	Intensity (%)	h	k	l
27.12	100	1	1	1
31.40	4	2	0	0
45.02	60	2	2	0
53.34	35	3	1	1

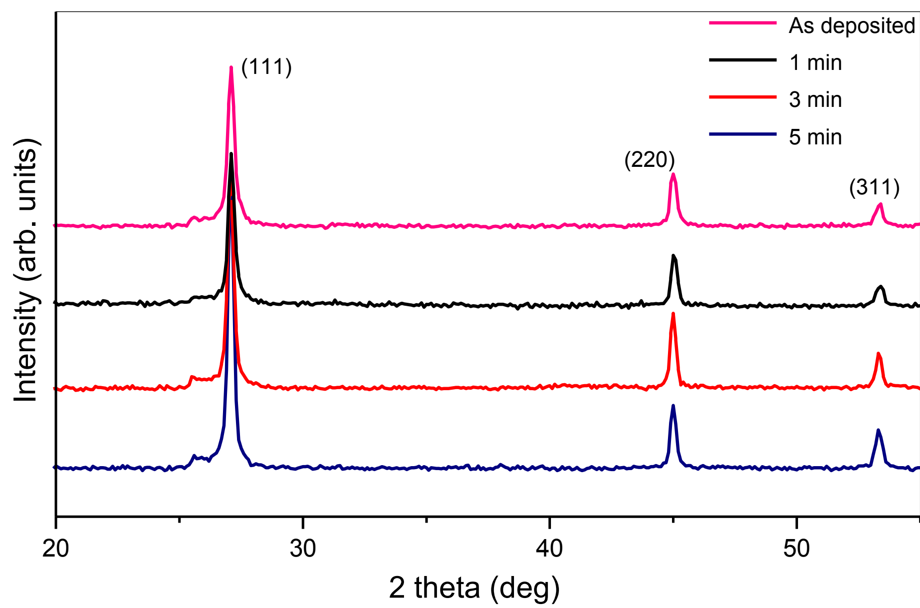

Fig. 5.1: XRD pattern of the as-deposited and the 1 min, 3 min and 5 min oxygen plasma treated CuBr films deposited on Si (100) substrates. All the scans were performed under the same experimental conditions.

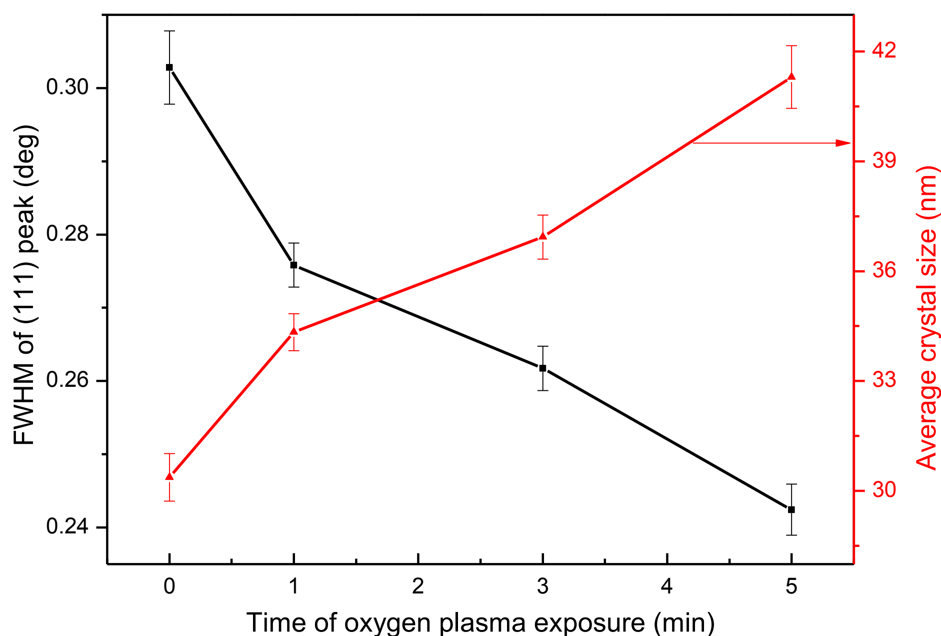

Fig. 5.2: Variation of FWHM of (111) peak and crystal size as a function of the oxygen plasma exposure time. The crystal sizes were calculated using Scherrer equation.

There are no signs of noticeable structural deformities of the Zincblende CuBr from XRD measurements, with the exposure to oxygen plasma up to a time interval of 5 min. However, a slight variation in the FWHM of the (111) peak is observed with the plasma exposure of the films. There was no significant deviation of the peak positions of the (111) orientation of the samples with the plasma exposure. Figure 5.2 illustrates the changes in the FWHM of the CuBr (111) peak and the crystal size as a function of the time of oxygen plasma exposure. The FWHM values were extracted by applying Gaussian fit to the (111) XRD peaks.

The crystal sizes were calculated using Scherrer equation (equation 3.1). A decrease in the FWHM and there by an increase in the average crystal size is noticed with the

increase of the oxygen plasma exposure time. The FWHM decreases from ~ 0.3° for the as-deposited sample to ~ 0.24° for the 5 min plasma exposed one. Conversely, the crystal size increases from ~ 31 nm for the as-deposited sample to ~ 41 nm for the 5 min plasma exposed CuBr film. This can be expected due to the fact that, the bombardment by the energetic argon and oxygen species from plasma causes a combinational effect similar to a low temperature annealing and plasma induced microstructural evolution of the film. During the plasma bombardment, the atoms on the surface and subsurface of the film gain extra energy and the increased mobility help them to relax to lower free energy sites. This enhances the growth of the grains with lower free energy. Similar kind of enhancement in the average grain size with the oxygen plasma exposure has been reported in polycrystalline ITO films [143]. Furthermore, effect of oxygen plasma irradiation on the $LiMn_2O_4$ films has also been reported [144].

The morphology of the as-deposited and the oxygen plasma exposed CuBr films were investigated using SEM and AFM techniques. The SEM micrograph of the as deposited CuBr film on the Si substrate is shown in figure 5.3. An acceleration voltage of 13 kV was used for all measurements. It was very difficult to get a good SEM image on the samples, due to the charging effect as a result of the poor conductivity of the sample. The right hand side image shows a zoomed portion of the lower magnification image in the left side of figure 5.3. SEM images show an average grain size of around 40 nm, which is comparable with the calculated crystal size using the Scherrer formula. The small variations between the grain sizes from both of the measurements can be assumed due to the presence of the agglomerated grains that are observed in the SEM image [43].

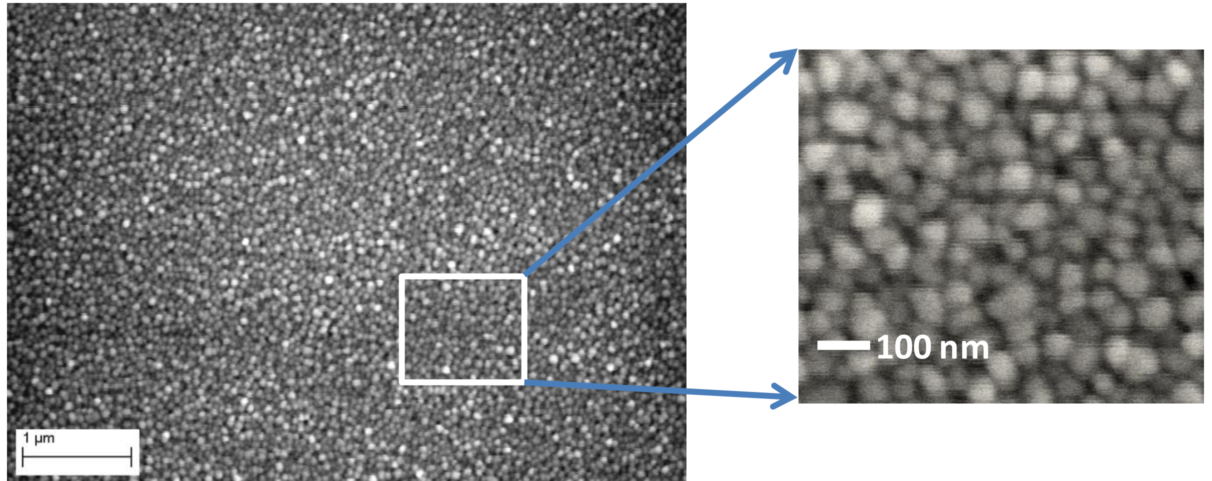

Fig. 5.3: SEM image of the as deposited CuBr film on Si substrate. An accelerating voltage of 13 kV was used for the imaging.

In order to examine the influence of oxygen plasma exposure on the morphology of the CuBr films, SEM studies were conducted on the plasma exposed films as well. It was observed that, there are no substantial variations on the surface morphologies of the 1 min and 3 min plasma exposed samples with respect to the as deposited one. But instead, there were indications of defect formation on the 5 min plasma exposed sample as shown in figure 5.4. The cause of the formation of these defects was assumed to be due to the relatively long time bombardment of the films by the energetic oxygen plasma. The defects observed as black spots are marked using red circles. The zoomed portion of such a spot is indicated on the right hand side of the figure 5.4. Hence it can be inferred that, the plasma exposure time of the films should be less than at least 5 min in order to minimize the defects, which is crucial for the use of these films for the p-n device fabrication.

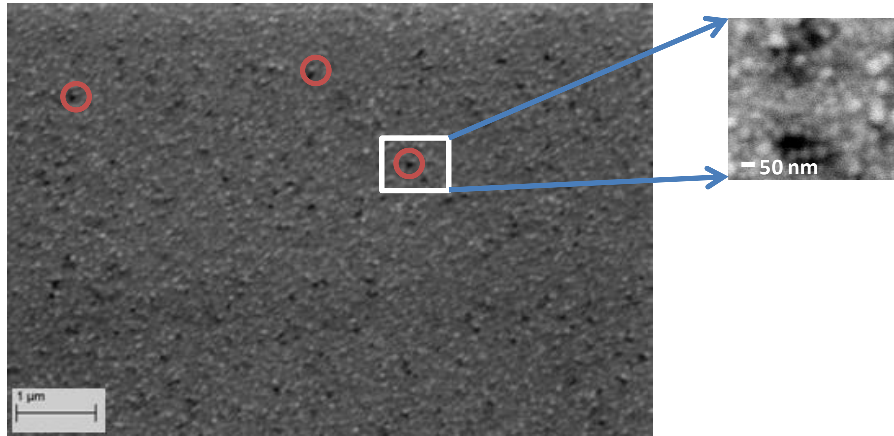

Fig. 5.4: SEM image of the 5 min oxygen plasma treated CuBr film deposited on Si (100) substrate.

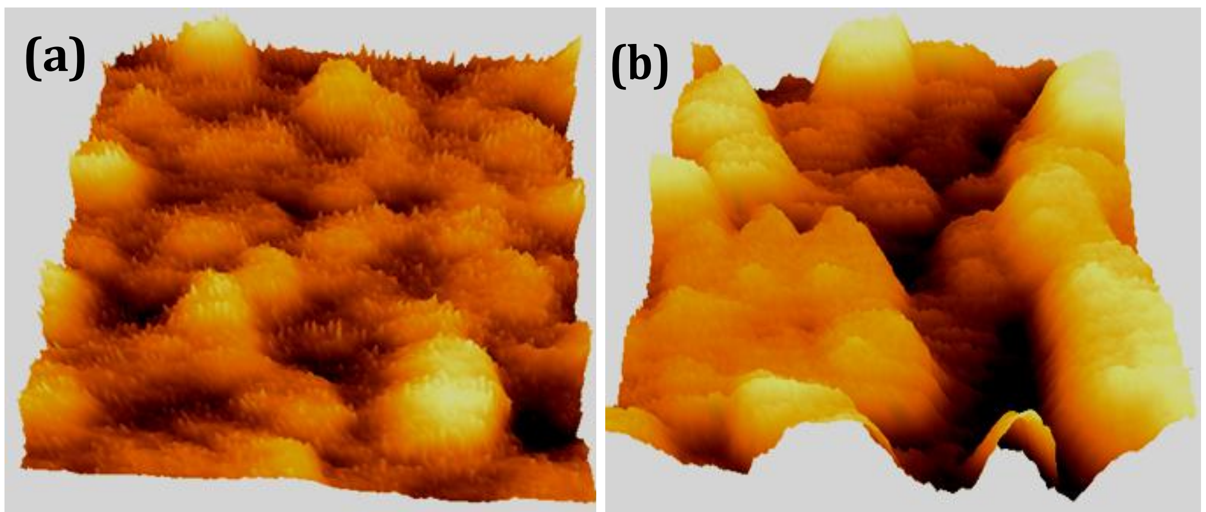

Fig. 5.5: AFM image of the (a) as deposited and (b) 5 min oxygen plasma exposed films deposited on Si (100) substrate. The imaging was performed under the identical conditions and the size of the image in both cases is equal to 0.71 µm×0.71 µm.

Figure 5.5 shows the AFM images of the (a) as-deposited and (b) 5 min. oxygen plasma exposed CuBr films deposited on Si substrates. The size of the image is 0.71×0.71 µm. Figure 5.5 (a) indicates the presence of more uniform grains

compared to (b). The latter clearly exhibits the effect of etching of the surface of the film due to the long time exposure in the oxygen plasma. Presence of bigger grains with non uniform shape and size can be observed for the 5 min plasma exposed sample. The increasing trend of the grain size with the plasma exposure time is in agreement with the trend that observed according to the XRD analysis. These AFM images are in good agreement with the SEM images discussed previously. The ridging effect observed in figure (b) can be correlated to the observed black spots in the SEM image of figure 5.4.

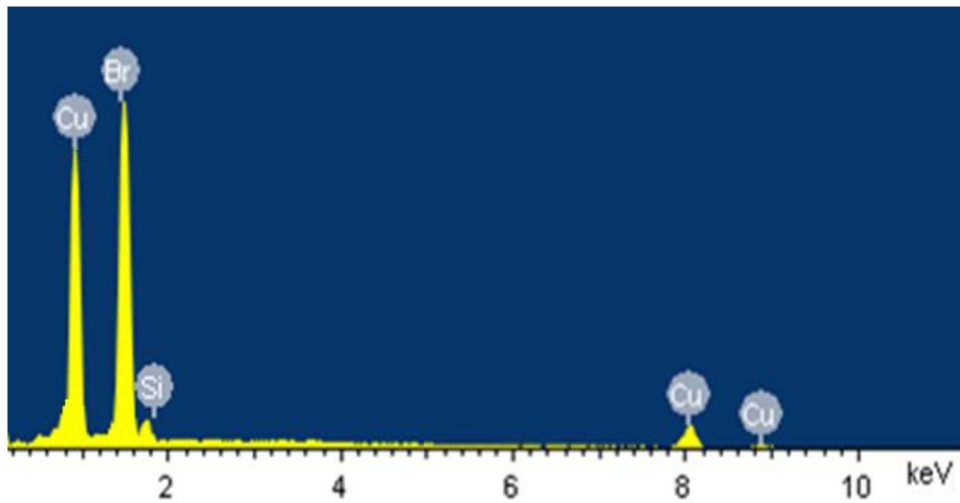

Fig. 5.6: EDX spectrum of a typical as-deposited CuBr film on Si substrate. The experiment was carried out at an accelerating voltage of 13 kV.

The EDX spectrum of a typical as-deposited CuBr film on Si substrate is showed in figure 5.6. An accelerating voltage of 13 kV was used for the measurement. Figure clearly shows the Cu and Br signals along with the Si signal from the substrate. Moreover, no impurity elements were detected from the sample.

5.3.2 Oxygen diffusion studies of the films using secondary ion mass spectroscopy (SIMS)

Secondary ion mass spectroscopy (SIMS) was used to substantiate the presence and diffusion of oxygen in the CuBr sample. The diffusion of oxygen in to the CuBr films is necessary for the reliable performance of these films for the p-n junction device applications. The as-deposited and the oxygen plasma exposed films on Si substrates were used for the SIMS analysis. The diffusion can be investigated by analysing the depth profile of oxygen in the film. In order to optimize the oxygen plasma exposure time of the CuBr film for the development of an effective p-type layer, the depth profiles of oxygen were analysed in samples, which are exposed to plasma for various time intervals. The count rates of different elements present were plotted against the depth of the film. Figure 5.7 indicates the depth profile of Cu and Br in the as-deposited CuBr films. Since the sputtering yield is different for various species (elements) present in the film, the count rate of an element cannot be considered as an actual reflection of the amount of the same in the film. But instead, the relative variation of the concentration profiles of a particular species (say for example, oxygen) in different samples (CuBr films) can be considered as a method to estimate the relative diffusion of that element in the film. Furthermore, the concentration profile can also account for the uniformity of the distribution of an element across the sample thickness.

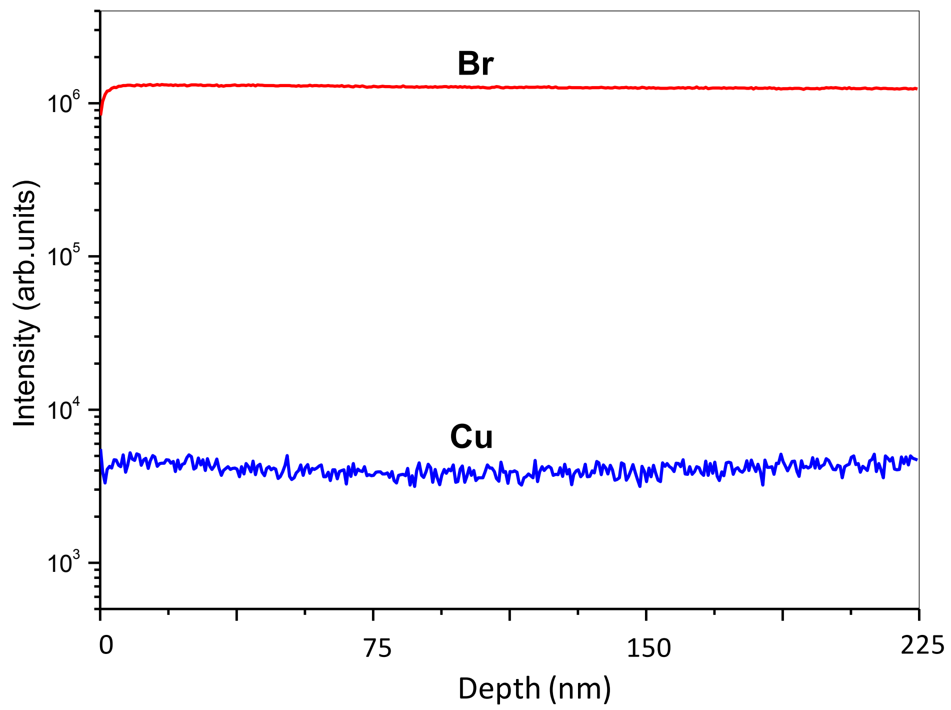

Fig. 5.7: SIMS depth profile of the as-deposited CuBr film deposited on Si substrate.

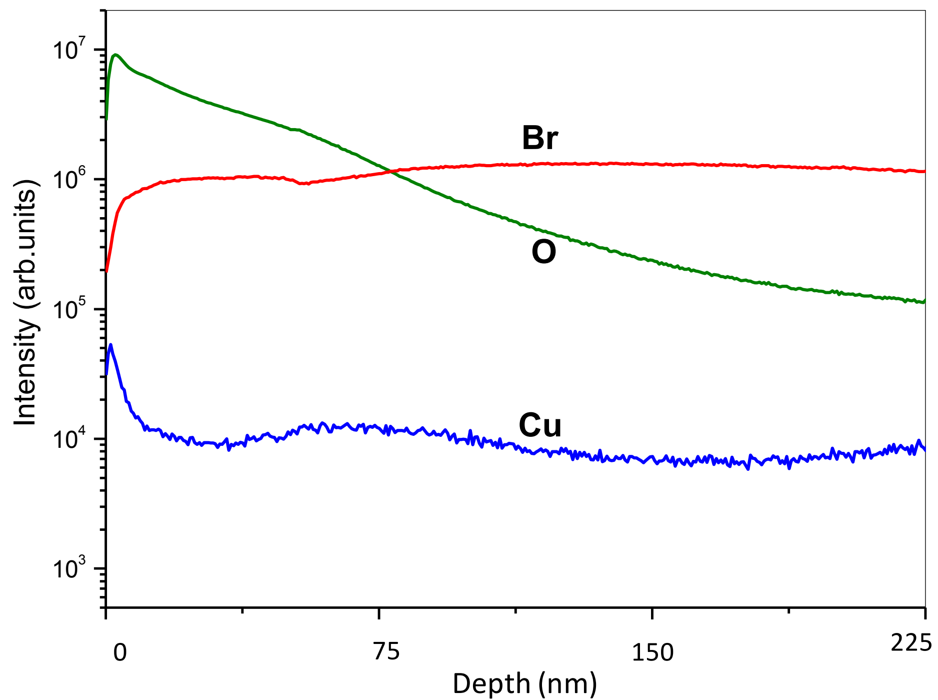

Fig. 5.8: SIMS depth profile of the 1 min oxygen plasma exposed CuBr film deposited on Si substrate.

It is clear from figure 5.7 that, the concentration profile of Cu and Br is almost uniform throughout the film. Again, the effects of oxygen exposure of the CuBr films are illustrated in figures 5.8 and 5.9. The concentration profile of the 1 min oxygen plasma exposed film is indicated in figure 5.8. Cu and Br profiles show moderate uniformity, with the appearance of features showing the surface etching of the films due to the plasma exposure.

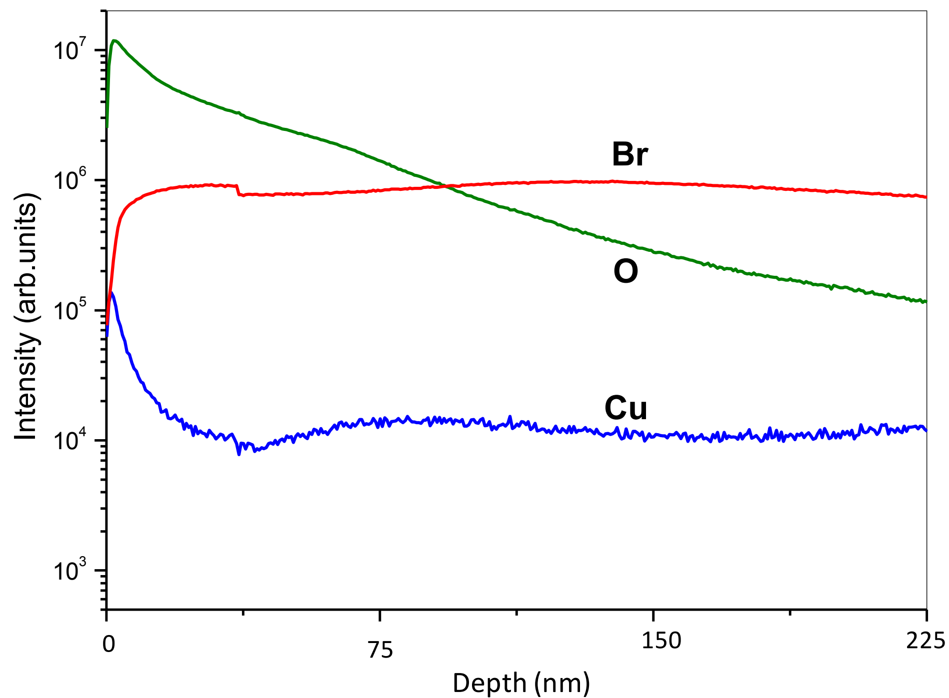

Fig. 5.9: SIMS depth profile of the 5 min oxygen plasma exposed CuBr film deposited on Si substrate.

Figure 5.9 shows the concentration profile of the 5 min oxygen plasma exposed sample. From figures 5.8 and 5.9, count intensity of oxygen at a depth of 150 nm is 2.3×10^5 and 2.8×10^5 respectively for the 1 min and 5 min oxygen plasma exposed films. This indicates that, there is an increase of oxygen count intensity with the increase of oxygen plasma exposure time. But as the exposure time increases, the

effect of etching also increases causes the formation of defects in the film, which is detrimental for the optoelectronic functioning of the film. The variation of oxygen count intensities at three different depths in the film have plotted as a function of the oxygen plasma exposure time as shown in figure 5.10. Figure delineates an order of magnitude increase in the oxygen count intensity for the 1 min oxygen exposed film with respect to the as-deposited CuBr film for all the three depths (~ 37 nm, ~ 75 nm and 150 nm).

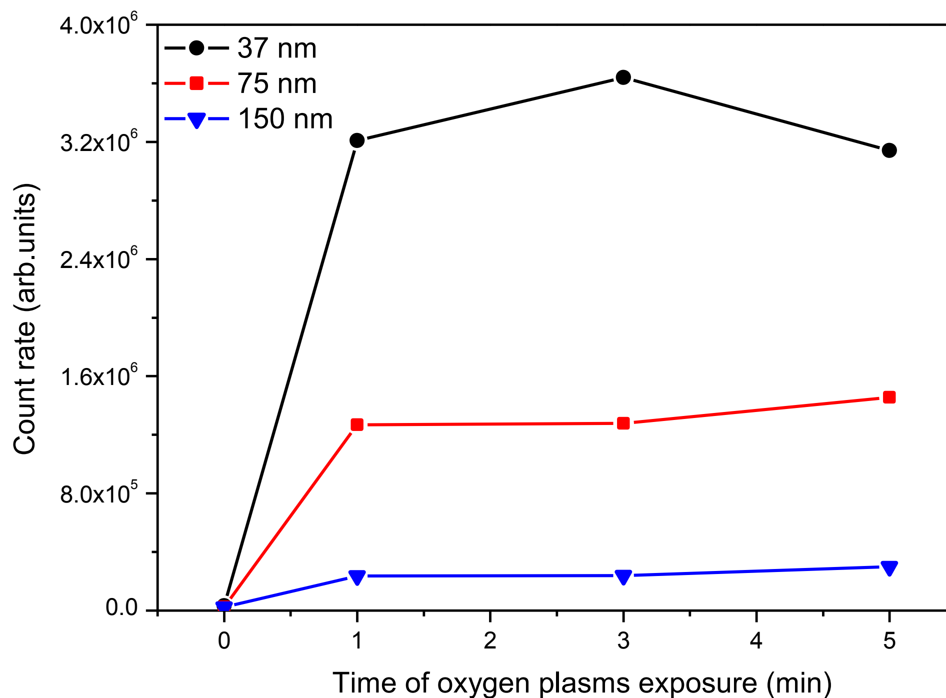

Fig. 5.10: Variation of the oxygen count rate at three different depths ~ 37 nm, ~ 75 nm and ~ 150 nm as a function of the oxygen plasma exposure time. This graph is plotted using the SIMS depth profile data of different samples.

There is slight increase in the count rate for 3 and 5 min exposure times at a depth of ~ 150 nm and 75 nm, but instead, the count rate decreased for the 5 min exposure at a depth of ~ 37 nm. This drop in the oxygen count intensity is attributed to the effect

of pronounced etching on the top surface due to relatively long term plasma exposure. Hence it can be inferred from the graph that the diffusion of oxygen in the film is quite good, which is highly important for the use of this film for the p-n junction device application.

5.3.3 Optical properties

The optical properties of the as-deposited and the oxygen plasma exposed CuBr samples were investigated using the room temperature absorption and the PL studies. The optical absorption spectra of the undoped and the oxygen doped CuBr films are as shown in figure 5.11.

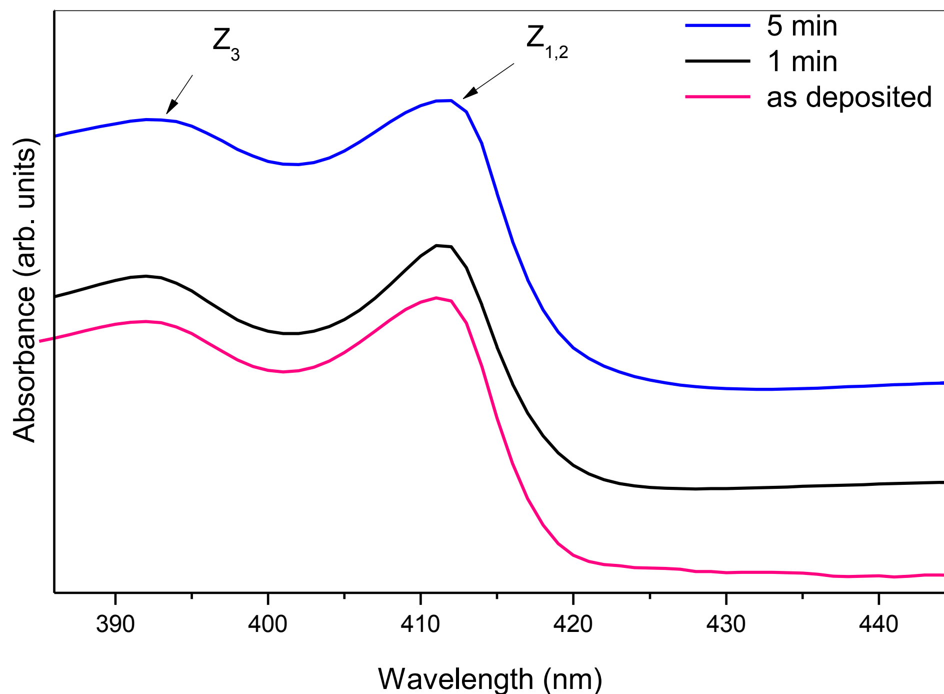

Fig. 5.11: Absorption spectra of the as deposited and the 1 min, 3 min and 5 min oxygen plasma exposed CuBr samples deposited on glass substrate taken under identical conditions.

Spectra shows two major absorption peaks around 411 nm (3.01 eV) and 391 nm (3.17 eV) which are represented as $Z_{1,2}$ and Z_3 respectively. These data are in good agreement with the previous reports on the optical properties of the cuprous halides by M. Cardona [142]. It is clear from the figure that, there is no considerable variation of the absorption peaks with the oxygen plasma exposure up to 5 min.

The UV-Vis transmission spectra of the as-deposited and the plasma exposed CuBr samples were also investigated to comprehend the influence of oxygen plasma treatment on the transmission properties of CuBr. Figure 5.12 shows the variation of the transmittance of the as-deposited and the 1 min and 5 min oxygen plasma exposed CuBr films, as a function of the wavelength.

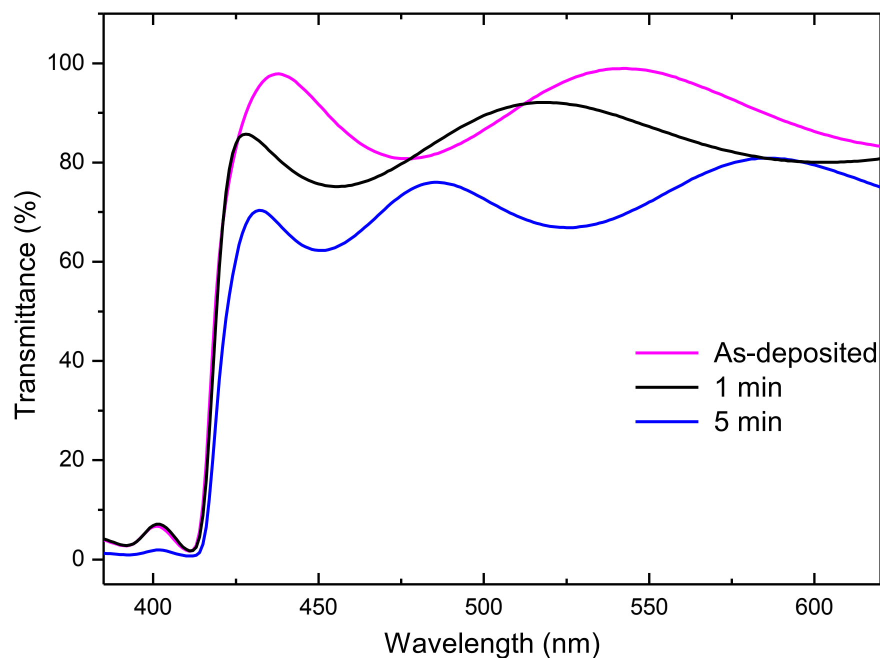

Fig. 5.12: UV-Vis transmittance spectra of the as-deposited and oxygen plasma exposed CuBr films for 1 min and 5 min deposited on glass substrate. The spectra were recorded under identical experimental conditions.

It is quite clear from the graph that, all the films show higher transparency above a wavelength of ~430 nm. Both the as-deposited and the 1 min plasma exposed films show an average transmittance of more than 80 % above the aforementioned wavelength. But interestingly, the average transmittance decreases with the time of oxygen plasma exposure, and it is only above 60 % for the 5 min plasma treated sample. Moreover, the transmission edge of the 5 min plasma treated film is found to be slightly red-shifted with respect to the as-deposited and the 1 min plasma treated sample. This is assumed to be due to the excessive concentration of oxygen in the CuBr crystal, but this still has to be confirmed.

The luminescence properties of the as-deposited and the oxygen doped CuBr films were investigated using the PL analysis. Figure 5.13 shows the room temperature PL spectra of the as-deposited and the 1 min and 5 min oxygen plasma exposed CuBr films. It has been reported that the free exciton luminescence in CuBr bulk crystal is attributed to the lowest energy triplet exciton, named Z_f, whose energy is slightly lower than that of the $Z_{1,2}$ free exciton, due to the exchange interaction [64]. Hence the high energy luminescence peak of CuBr originates from the Z_f free exciton [65]. The spectra showed in figure 5.13 illustrate a strong emission at around 2.97 eV (~417 nm), which is in close agreement with the previous reports on the room temperature PL studies in CuBr [145, 75]. It was observed that, there was no considerable reduction of the intensity of the PL peaks in the 1 min and 3 min oxygen plasma exposed CuBr films with respect to the as-deposited film. Since strong PL response is widely considered as an indication of a high surface quality [146], it can be assumed that there was no substantial etching happened to the film up to a plasma exposure time of 3 min. But there was a massive reduction of luminescence intensity observed in the 5 min oxygen exposed film.

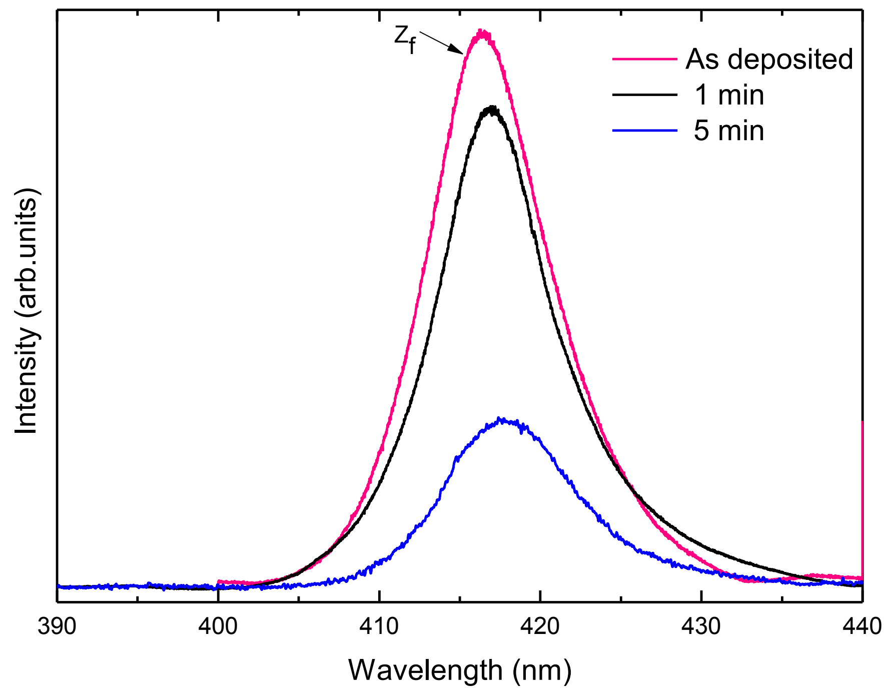

Fig. 5.13: Room temperature PL of as-deposited and 1 min and 5 min oxygen plasma exposed CuBr films.

Moreover, a slight broadening of the PL peak was also noticed for the aforementioned sample. This effect is attributed to the fact that the longer exposure to the oxygen plasma will introduce defects in the CuBr films, which can reduce the emission intensity of the film. The effect of PL quenching due to surface defects was previously reported in Si wafers [147]. The formation of the defects in the 5 min exposed sample is also confirmed in the SEM image (figure 5.4).

5.3.4 Electrical Properties

According to the previous reports, γ-CuBr is usually copper deficient, and the p-type conductivity which arises due to the hole produced by the copper defect can be explained using the Kroger-Vink notation as,

$$V_{Cu} \rightarrow V'_{Cu} + h^{\cdot} \qquad (5.1)$$

The earlier investigations on the Hall measurements of the CuBr samples reveals that, one of the possible reasons for the higher hole concentration would be the introduction of oxygen in to the bromine sites and thereby the creation of acceptor levels in the lattice. The doping effect can be represented as explained by Knauth *et al.* [82] as,

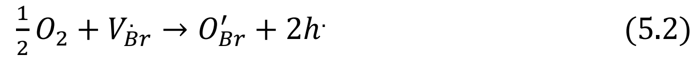

$$\frac{1}{2}O_2 + V_{Br}^{\cdot} \rightarrow O'_{Br} + 2h^{\cdot} \qquad (5.2)$$

Similar results on the increased conductivity of CuI films due to the incorporation of oxygen have also been reported by Zhu *et al.* [148]. In our studies, since the CuBr films are exposed to the oxygen plasma, the diffusion of oxygen in the film would be higher than that which occurs due to simple exposure of the films to atmosphere. Hence we expect more effective p-type doping of the CuBr films as result of the plasma exposure. In order to investigate the effect of oxygen inclusion on the electrical properties of the CuBr films, Hall measurements were performed on the films deposited on glass substrates with gold ohmic contacts. The resistivity, carrier concentration and carrier mobility of the films were examined as a function of the time of oxygen exposure. Since the gold contacts were no longer ohmic for the as deposited sample due to its very high resistance, it was not possible to make a reliable Hall measurement on this sample. The CuBr films were then exposed to

oxygen plasma for different time intervals to dope it with oxygen and hence to make it conductive. As the plasma exposure time increases, the chance of etching of the films also increases. Several iterations were made to fix the plasma parameters and exposure time to confirm maximum diffusion of oxygen with minimum etching of the film by observing the electrical properties and surface morphologies of the films.

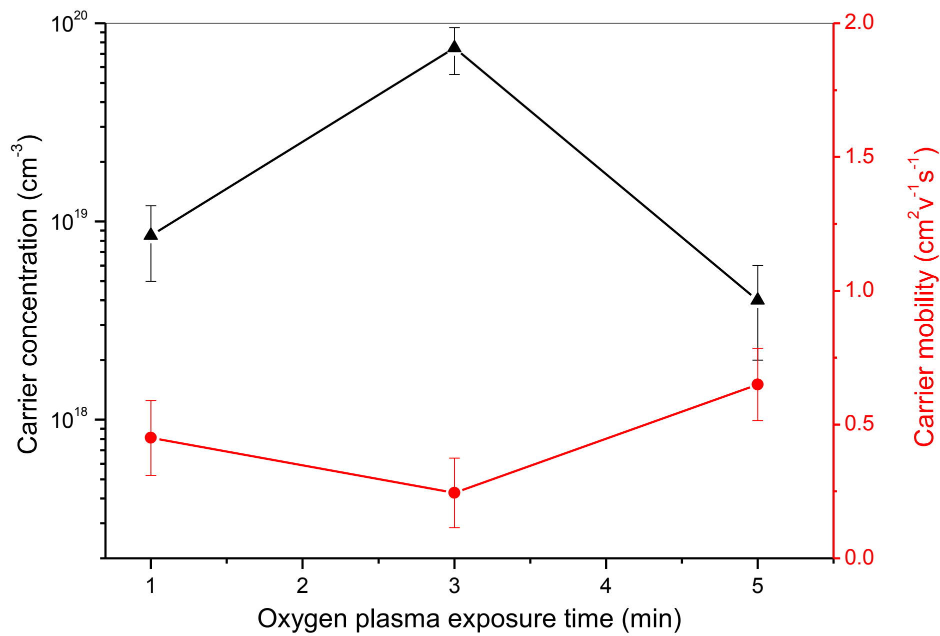

Fig. 5.14: Variation of Carrier concentration and carrier mobility as a function of the time of oxygen plasma exposure.

The impact of the oxygen plasma exposure time on the carrier concentration and carrier mobility of the films has been illustrated in figure 5.14. An inverse trend between the carrier mobility and the carrier concentration with the increase of the plasma exposure time is revealed. At first the mobility decreases from 0.45 $cm^2V^{-1}s^{-1}$ to 0.24 $cm^2V^{-1}s^{-1}$ and then increases to 0.65 $cm^2V^{-1}s^{-1}$, as the time of plasma exposure changes from 1 to 3 and then to 5 minutes respectively. On the contrary to

this, the hole concentration initially increases from 8.5×10^{18} cm^{-3} to 7.5×10^{19} cm^{-3} and then reduces to 4×10^{18} cm^{-3} as the change of exposure time from 1 to 5 minutes. The increase in the hole concentration with the increase of plasma exposure can be explained as due to availability of relatively higher number of oxygen species for conduction (see equation (5.1)). The inclusion and diffusion of more oxygen in to the film with the plasma exposure time is also confirmed using the SIMS depth profile. The reduction in the carrier concentration at higher plasma exposure time (5 min) may be due to the fact that some of the incorporated oxygen will go in to the plasma created defects and simply act as a defect passivation layer rather than contributing to the conduction process. Again, the possibility of the formation of an oxide phase (Cu_2O, although not detected by XRD) cannot be ignored at this long term plasma exposure. The slight improvement in the mobility of the 5 min plasma exposed film is assumed to be due to the slight increase in the grain size of this film (confirmed from figure 5.2, and AFM image), thereby reduce the possibility of the grain boundary scattering.

The resistivities of the oxygen plasma exposed films are plotted in figure 5.15. It is quite clear from the graph that the extremely high resistivity of the CuBr samples fell down to orders of few ohms by the exposure to oxygen plasma. The sudden decrease in the resistivity is expected due to (1) the exposure of the entire film surface to plasma at the same time and (2) the diffusion of oxygen happens everywhere on the surface simultaneously. It was difficult to alter the doping percentage of oxygen in to the film considerably by varying exposure time, since there was a trade off between the oxygen diffusion and the etching effect of the surface. Figure 5.15 shows slight variations in the resistivities of the film with the

plasma exposure of 1- 5 minutes. The variation of resistivity shows a similar trend as that of the mobility with respect to the plasma exposure time.

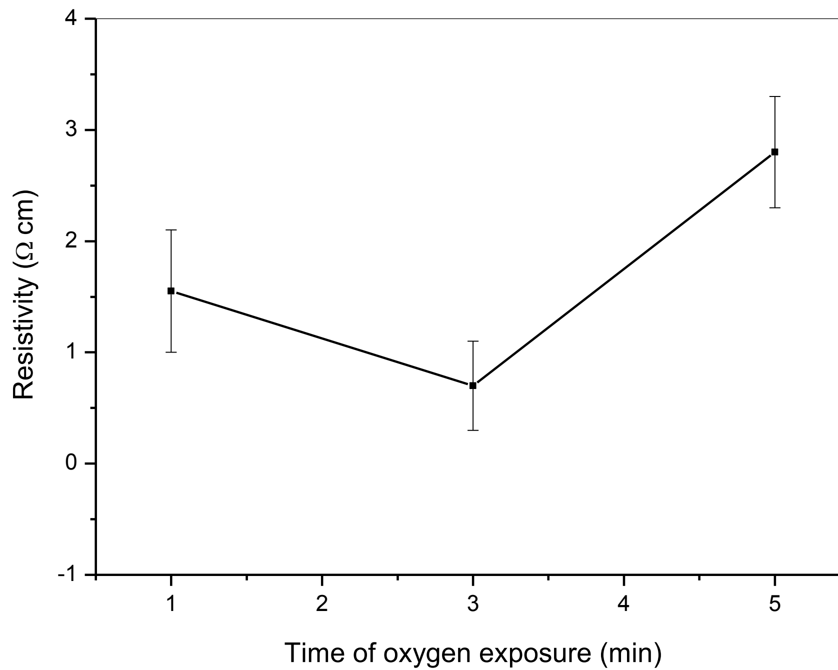

Fig. 5.15: Resistivity of the CuBr film as a function of the time of oxygen exposure.

The resistivity decreases from 1.55 Ω cm to 0.7 Ω cm as the exposure time increases from 1 min to 3 min. This can be explained as a result of the increase of the carrier concentration in the film. As the oxygen exposure time increases to 5 min, the resistivity found to be increased slightly to 2.8 Ω cm due to the decrease in the carrier concentration in the film (figure 5.14) This is believed to be due to the influence of relatively higher etching rate of the film and also, due to the higher chance of formation of defects or damage caused by the energetic plasma bombardment on the film.

5.4 Summary

The growth of p-type CuBr thin films on Si and glass substrates by vacuum evaporation followed by oxygen plasma treatment, and the optoelectronic characterisation of the films are described in this chapter. The preferential (111) orientation of the films is confirmed using XRD. The diffusion of oxygen in to the CuBr film is found to be quite good, using the SIMS analysis. The absorption and PL studies ensure the opical quality of the p-type CuBr film. P-type conductivity of CuBr films was confirmed using room temperature Hall measurements. The variation of resistivity, carrier concentration and carrier mobility of CuBr films as a function of plasma exposure time was investigated. The carrier mobility, hole concentration and the resistivity of the p-CuBr films varies as 0.24 - 0.65 $cm^2V^{-1}s^{-1}$, 4×10^{18} cm^{-3} – 7.5 $\times10^{19}$ cm^{-3} and 0.7 - 2.8 Ω cm respectively. Hence, one can conclude that, it is possible to deposit a p-type CuBr film with good crystal quality and luminescent property and with resistivity, hole concentration and mobility values ~ 1.5 Ω cm, ~ $8x10^{18}$ cm^{-3} and ~ 0.5 $cm^2V^{-1}s^{-1}$, respectively with an oxygen plasma exposure time of 1 min.

Chapter 6

CuBr/Si heterojunction for photovoltaic applications

6.1 Introduction:

A material that converts light energy in to electrical energy is called a photovoltaic (PV) material, which performs an important role in the field of renewable energy. So far, there are several reports on various materials and technologies for the PV applications. These include crystalline Si, single junction GaAs, thin film technologies, tandem cells, multi-junction concentrators and other emerging technologies like dye-sensitized cells, organic and inorganic cells, quantum dot cells etc. Although crystalline silicon is the dominant candidate in the photovoltaic market, higher cost of manufacture act as a major obstacle for the commercialization of the aforementioned cells. Hence the search for cheaper materials and simple processing techniques are essential for the cost reduction. Again, the minimization of material usage through the introduction of thin film technology will also reduce the production cost [149]. Recent literature shows that, heterojunction PV cells made by the deposition of a transparent semiconductor thin film on Si substrate can be a good candidate for the PV applications [150].

There are several reports on the heterojunction solar cells based on the transparent oxide-semiconductor heterojunctions [151-159]. The thin films of these oxide

semiconductors have exceptional properties of high optical transparency with good electrical conductivity. They perform not only as a heterojunction partner but also an anti reflection coating [160]. Examples for the transparent conducting oxides used are semiconductors like indium oxide (In_2O_3), tin oxide (SnO_2) and indium tin oxide (ITO). But the crucial problem associated with these materials is the higher cost due to limited indium resources. Hence cheaper and alternative materials have to be explored for the large area and terrestrial applications [161]. Improvement of the short circuit current (J_{SC}) in CIGS (Copper Indium Gallium Selenide) thin film solar cells has been reported by using a transparent conducting boron doped ZnO window layer [162].

It was already shown in chapter 5 that, both the as-deposited and oxygen doped CuBr exhibits good absorption in the UV and blue/violet region of the spectrum. Owing to lower lattice mismatch with Si (~ 4.7%) compared to other well known UV emitting materials like ZnO, CuBr will be worth trying as a candidate for the use as a heterojunction partner with Si. This heterojunction has advantages like simple processing techniques, better blue response, non-toxicity and lower cost. Furthermore, it has been reported that, highly conductive wide-gap p-type window materials are very difficult to fabricate, which corroborate the importance of the development of p-CuBr and the heterojunction device [152]. This could be an attractive candidate for the future PV technologies because the metals are abundant on earth, inexpensive and non-toxic.

6.2 Experimental methods

P-type CuBr layers required for the fabrication of the PN heterojunction were deposited on Si substrate as discussed in chapter 5. N- type Si (111) wafer with a resistivity of around 1-10 Ω cm was used as the substrate. Prior to deposition, the Si substrates were cleaned using acetone and de-ionised water in an ultrasonic bath subsequently dipping in to a 10 % solution of HF to remove the natural SiO_2 layer from the surface. Then it was again cleaned using de-ionised water. The back ohmic contact for Si was made using evaporation of an Al layer, followed by a heat treatment at 400°C for 3 min. The p-CuBr/n-Si heterojunction was fabricated using a 1 minute plasma exposed CuBr film and the IV characteristics were investigated using a Keithley 4200 semiconductor parameter analyser. Evaporated gold layer was used as the top electrode for the heterojunction cell. Metal shadow masks with a hole diameter of 3 mm was used during the evaporation of gold for making circular contacts on the device, which was used as the cell size. Photoresponse properties of the heterojunction were analysed by the illumination of the device using incandescent lamp and blue and red LEDs.

6.3 Theory of heterojunction diode and photovoltaic cells

A PV cell can be considered as a p-n diode which can generate power to an external load when it is illuminated. The basic idea of the photovoltaic effect can be explained as follows. When a semiconductor absorbs light with photon energy greater than its band gap, free holes and electrons are produced. The essential property needed for the operation of the photovoltaic cell is the presence of an

internal field which can separate the freed carriers in to the external circuitry before the recombination happens. In general, the photovoltaic devices need to fulfil two requirements, first one is the photogeneration of electrons and holes in the light absorbing material and the second is the separation of these carriers to the external circuitry. When p and n-type semiconductors combine to form a p-n junction, due to the differences in the electron and hole concentrations on the two sides, electrons will diffuse in to the p-region and hole to the n-region. This carrier diffusion would cause the appearance of positive charges on the n-side and negative charges on the p-side (as shown in the figure 6.1(a)), which leads to the formation of an electric field. Further diffusion will be balanced by the developed potential barrier. This field then produces an internal potential drop at the junction (figure 6.1(b)).

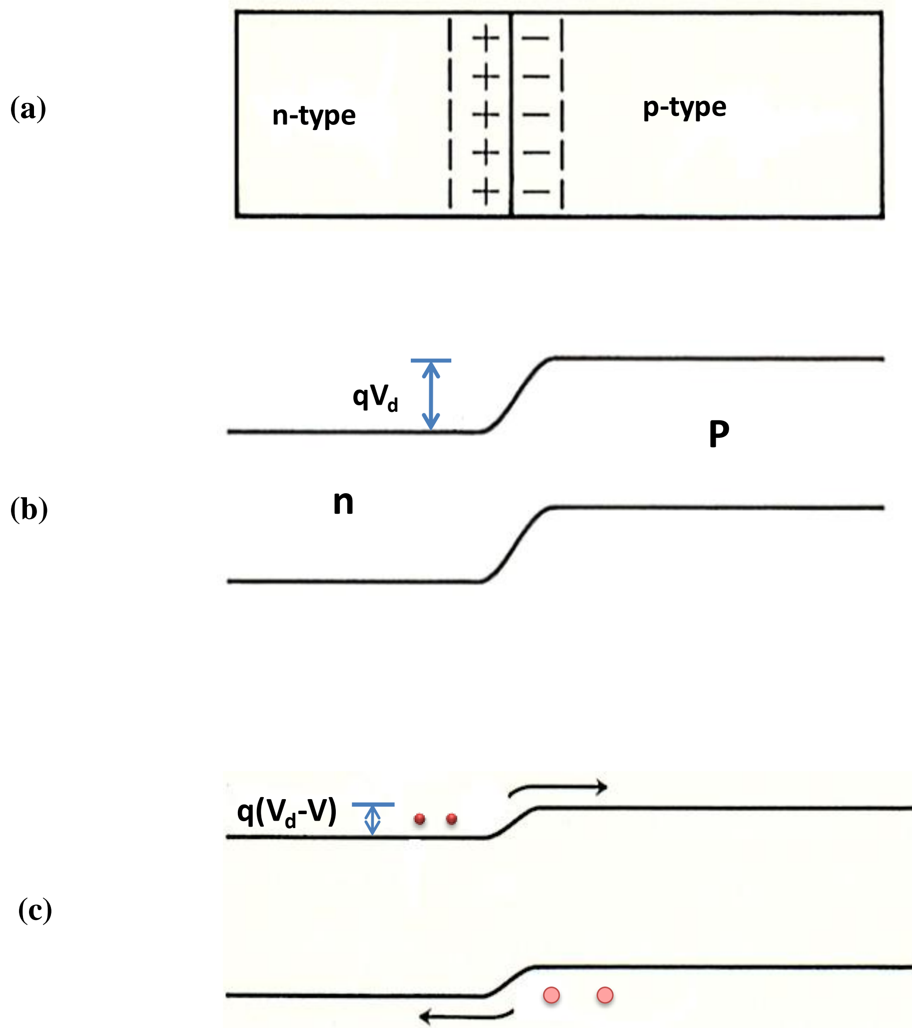

Fig. 6.1: Schematic of the (a) p-n junction, energy band diagram (b) without an applied voltage and (c) with an applied voltage of V across the junction.

The space consisting of the two charge layers is called the space charge region or the depletion region. Afterwards, when a forward bias voltage is applied to the junction (figure 6.1(c)), the potential barrier is sufficient to balance the diffusion tendency,

which thereby causes a current flow across the junction due to the injection of electrons to the p-region and holes to the n-region [163]. In the case of an ideal diode in which diffusion is the major carrier transport mechanism at the junction interface, The Shockley diode equation can be used to express the J-V characteristics. According to the conventional p-n heterojunction theory, the J-V characteristics can be approximately expressed using the following equation, (J=I/A, is the current density; where A is the area of the device)

$$J = J_s \left\{ \exp\left(\frac{qV}{kT}\right) - 1 \right\} \tag{6.1}$$

Where, q is the electronic charge, T is the temperature, k is the Boltzmann's constant and J_s is the reverse saturation current density.

A PV cell can be considered as a two terminal device which conducts like a diode in the dark, and produces a photovoltage under illumination. The photoresponsive properties of the p-n heterojunction PV cell can be investigated by the analysis of the J-V characteristics under illumination. An equivalent electrical circuit model used to describe the J-V characteristics of the ideal p-n type PV cell is illustrated in figure 6.2, where a constant current source is in parallel with the junction. The source I_L results from the excess carriers produced by illumination; I_s is the diode saturation current and R_L is the load resistance.

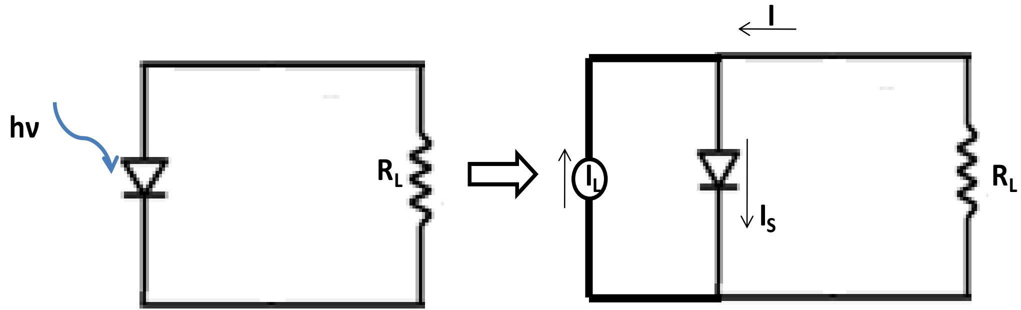

Fig. 6.2: Schematic of an ideal PV cell equivalent circuit. A constant current source is connected in parallel with the junction. The current source I_L results from the excitation of excess carriers by illumination, I_s is the diode saturation current and R_L is the load resistance.

The I-V characteristics of the above device can be written as

$$I= I_s \left\{\exp\left(\frac{qV}{kT}\right) - 1\right\} - I_L \qquad (6.2)$$

And $J_S = {I_S}/{A}$, where A is the area of the device [160].

When the PV cell is illuminated, photocurrent is produced due to the generation of electron-hole pairs. This photocurrent shifts the J-V characteristics by the amount of photocurrent in the negative direction along the Y axis (Current axis) as shown in the figure 6.3. The points at which the J-V graph crosses the X-axis (voltage axis) and Y-axis (current axis) are termed as the open circuit voltage (V_{oc}) and short circuit current (J_{sc}) , respectively. V_{oc} can be defined as the voltage developed across the cell when the current in the external circuit is zero or it is the maximum voltage

available from a solar cell. Similarly, J_{sc} can be defined as the current flows through the cell when the voltage across it is zero, or when the cell is short circuited. V_{oc} can be expressed using the following equation,

$$V_{oc} = \frac{kT}{q} ln\left(1 + \frac{J_{sc}}{J_0}\right) \qquad (6.3)$$

The theoretically attainable maximum power that can be extracted from the cell is given by the product of J_{sc} and V_{oc} ($|J_{sc} \times V_{oc}|$). But the real maximum power (P_{max}) will be equal to the maximum value of the product J×V ($J_m \times V_m$) in the range between voltages 0 and V_{oc} and current densities 0 and J_{sc} (or P_{max} is the greatest possible product of J and V at an operating point). The ratio of P_{max} to the product $|J_{sc} \times V_{oc}|$ is called the Fill Factor (FF) of the PV cell.

$$FF = \frac{P_{max}}{J_{sc} \times V_{oc}} \qquad (6.4)$$

Hence FF is a measure of the "squareness" of the trace of the J-V characteristics and is also the area of the largest rectangle that fits into the J-V curve.

The power conversion efficiency of the PV cell can be defined as the ratio of the maximum power produced by the PV cell to the power incident due to the illumination.

$$\eta = \frac{P_{max}}{P_i} = \frac{FF \times J_{sc} \times V_{oc}}{Pi} \qquad (6.5)$$

Where, P_i is the illumination power density.

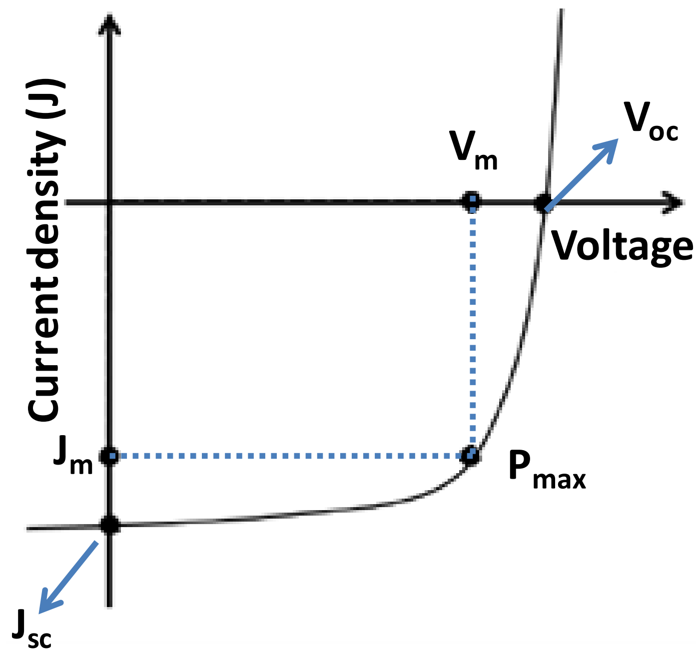

Fig. 6.3: Demonstration of J-V characteristics of a PV cell under illumination. (V_m, I_m) is the maximum power point. V_{oc} and J_{sc} are the open circuit voltage and the short circuit current, respectively.

In order to improve the efficiency, one should improve the three factors in the numerator of equation 6.5.

The photovoltaic conversion efficiency has some theoretical upper limits (~ 28% for crystalline Si) due to the following physical reasons:

(1) Among the total incoming photons, ~ 25 % have energies less than the band gap energy of the material and hence no electron hole pair generation takes place. (2) ~ 30 % have energy greater than the band gap of the material and will be wasted as

heat or re-emitted. Hence, ~55% of the original energy is wasted due to the ineffective interactions of light with the solar cell materials.

The capability of a solar cell to convert an incoming photon of particular wavelength in to electron hole pair is called quantum efficiency. If the measurement neglects the loss due to reflection, it is called internal quantum efficiency and if it includes the reflection loss, it is termed as external quantum efficiency [164].

A standard test condition is normally used for the determination of the conversion efficiency of the photovoltaic cells (solar cells). The above standard is given by, an irradiance of 1000 W/m^2 perpendicular on to the front surface of the cell, kept at a temperature 25°C and the spectral distribution passing at an elevation angle of 41.8° through the atmosphere, which is termed as air mass 1.5 (AM 1.5).

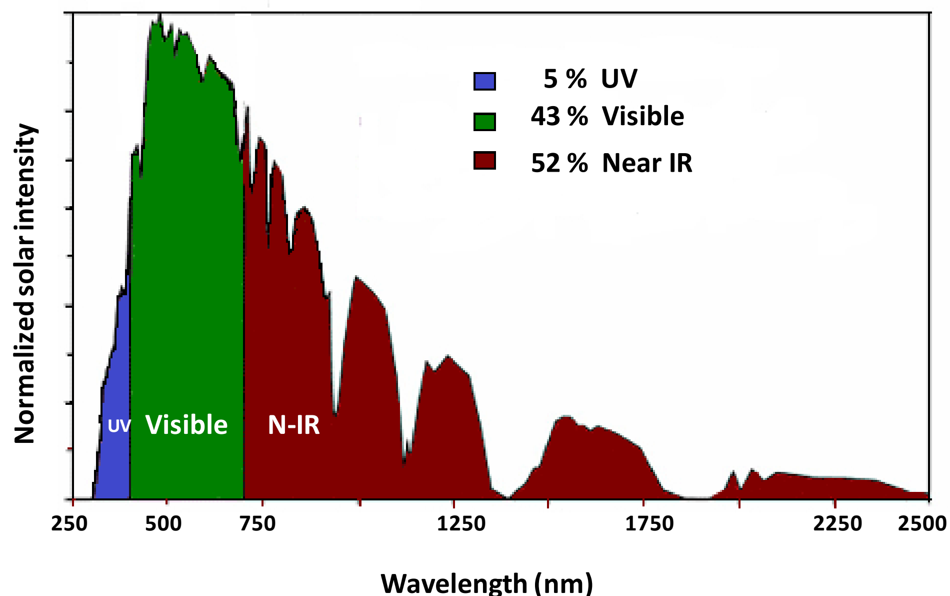

Fig. 6.4: Solar energy distribution corresponding to AM 1.5 illumination. Intensity profile of sunlight at the surface of the earth.

Figure 6.4 shows the intensity profile of the sunlight at the surface of the earth. It is clear from the plot that, contribution from the ultraviolet (UV) radiation is very small compared to the visible and near infrared (IR). Visible light (0.4–0.7 µm) contributes 43% of the power, about 52 % is in the near-infrared (NIR) region (0.7–2.5 µm, 52%) and the rest in the UV region (0.3–0.4 µm, 5%) [165].

Consider the case of a p-n heterojunction PV cell made of a p semiconductor layer of band gap E_{g1} and an n- layer of band gap E_{g2}. (figure 6.4) (1) When light with energy less than E_{g1} (first) but greater than E_{g2} (second) is incident on the device, it will pass through the first layer , which then act as the window layer and get absorbed by the second layer. (2) When the light energy is greater than $E_{g1,}$ then it will be absorbed by the first layer itself. In both the above cases, the carriers generated in the depletion region and within a diffusion length of the p-n junction will be collected from the cell.

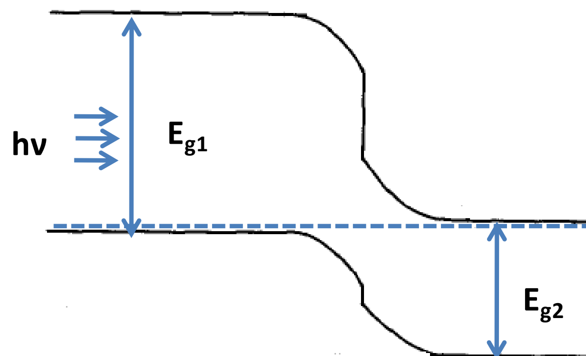

Fig. 6.5: Schematic of an energy band diagram of a p-n heterojunction.

The following are the advantages of these kinds of cells. (1) They will have improved spectral response in the short wavelength region, if E_{g1} is higher enough to

absorb this range of frequencies and result to better and effective carrier generation. (2) The series resistance can be lowered by the heavy doping of the first semiconductor without affecting its light transmission properties. (3) The radiation tolerance can be enhanced by the use of thick layer of the first semiconductor besides being high in band gap.

6.4 Results and discussion

6.4.1 I-V characteristics of the CuBr/Si heterojunction

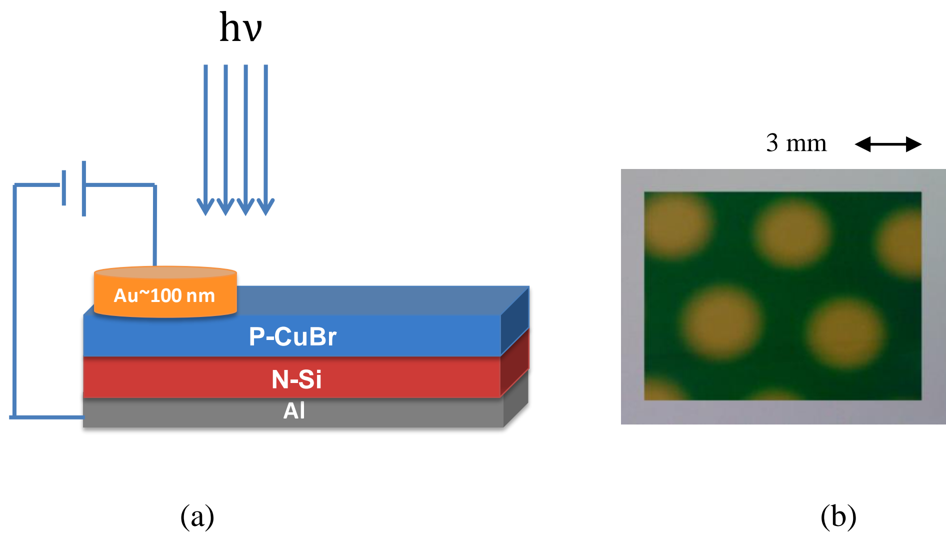

Fig. 6.6: (a) Schematic of the structure of the P-CuBr/N-Si heterojunction device, (b) photograph of the top view of the device. The yellow dots are the circular gold electrode on the top of the device.

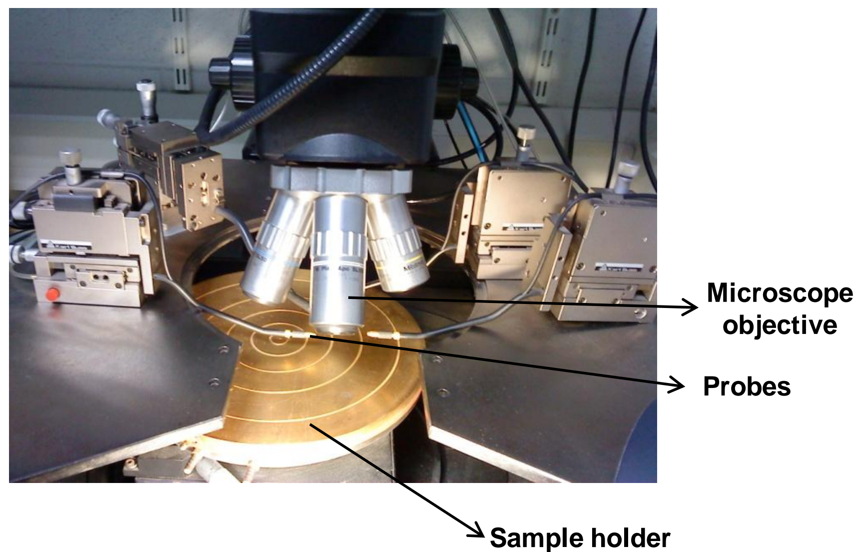

Fig. 6.7: Photograph of the probe station used for the I-V measurements.

Schematic structure and a photograph of the top view of the CuBr/Si heterojunction used for our studies are indicated in figure 6.6. Before starting to learn the properties of the heterojunction, it is essential to make sure that the gold contacts to the p-CuBr is ohmic. In order to prove this, p-CuBr is deposited on a glass substrate followed by the evaporation of Au electrode layer on top of that, and then studied the current-voltage characteristics of the structure. The two probes were placed on the 2 different Au contacts. I-V curve between the two gold contacts on the p-CuBr is plotted in figure 6.8. The linear and symmetric I-V curve confirms good ohmic behaviour of the Au contacts. Moreover, Al metal has already been reported as a good ohmic contact for N-Si [166]. Afterwards, the p-n device is placed on the sample stage of the probe station and the 2 probes of the instrument are placed on the 2 electrodes (Au and Al) of the device. In order to test the device under forward and reverse bias condition, the applied voltage was varied from -4 V to +4 V, and the corresponding currents were measured.

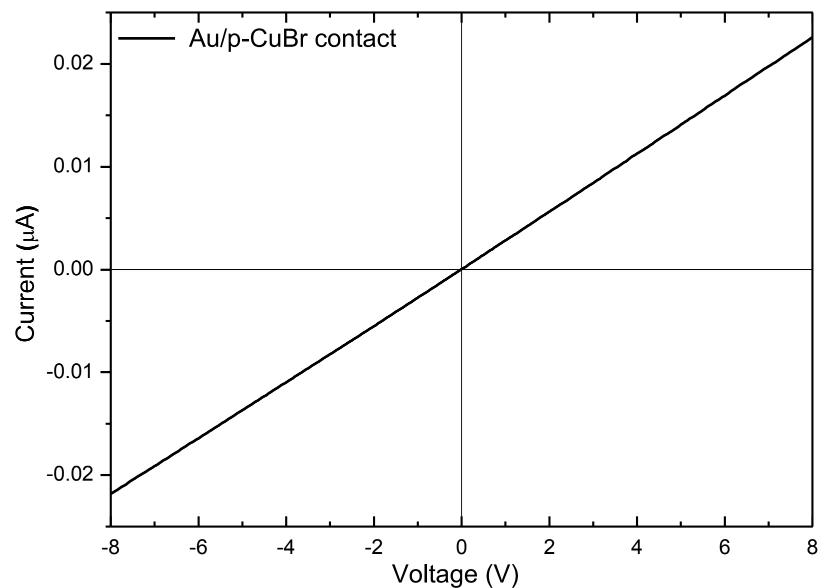

Fig. 6.8: I-V characteristics measured between two gold contacts on p-CuBr.

The I-V characteristics of the CuBr/Si heterojunction under dark condition at room temperature are illustrated in figure 6.9. The non-linear behaviour of the I-V Curve verifies the rectifying property of the heterojunction. In the forward bias condition the current increases super-linearly with the increase of the applied voltage. Also extremely small increase in the reverse leakage current in the reverse bias condition demonstrates the good rectifying behaviour of the heterojunction. Again, the ohmic nature of the Au contacts confirms that, the rectification occurs from the p-n junction itself.

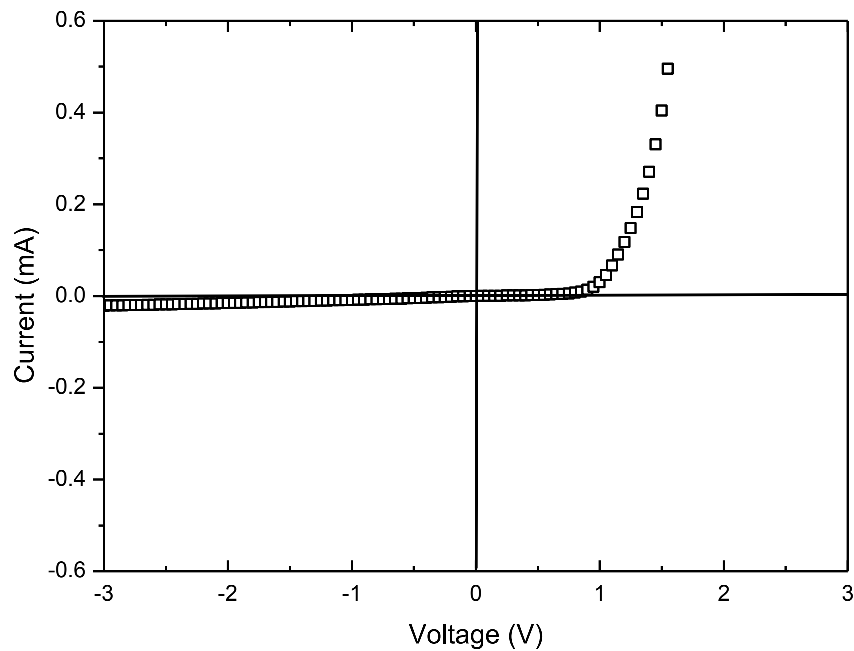

Fig. 6.9: I-V characteristics of the p-CuBr / N-Si heterojunction.

From the I-V curve, one can see the rectification ratio, that is the ratio of the forward to reverse current (I_F/I_R) is ~ 31 at 3 V, which indicates the formation of a good heterojunction diode with the CuBr/Si combination. The reverse leakage current is found to be only 2×10^{-5} A at 3 V reverse bias. The turn on voltage of the heterojunction is found to be ~ 1 V. When a forward bias of 3 V is applied, the

current density reaches up to 95 A/m^2. The ideality factor n, which indicates the quality of the diode, can be determined with the help of equation (6.1). Using the above equation, n can be expressed as [167],

$$n = \frac{q}{kT}\frac{dV}{dlnJ} \tag{6.6}$$

'n' can be determined from the slope of the straight line region of the forward bias log J -V characteristics using equation 6.6. According to the above equation, the ideality factor of the heterojunction is about 1.32 when the forward bias voltage is 0.02- 0.06 V, about 2.48 at a forward voltage of 0.06- 0.2 V and about 4.39 at forward voltage 0.2- 0.4 V. According to Sah-Noyce-Shockley theory [168], the ideality factor of a p-n junction is 1 at lower voltage and 2 at higher voltage. Ideality factors greater than 2 are assumed to be due to the presence of some surface states or may be due to the presence of a thin SiO_2 layer on the Si substrate even after the HF cleaning.

The plot extracts a turn-on voltage of ~ 1 V for the p-n device, which is less than the band gap energy of CuBr (3.1 eV). Since the band gap of the p-region is more than two times of that of the n-region, the barrier region will be asymmetrical as shown in figure 6.10. Figures 6.10 (a) and (b) show the schematic energy band diagrams at thermal equilibrium and under forward bias, respectively. The low turn-on voltage can be tacit from this band structure. In the present case, the carrier concentration in the p-region is orders of magnitude higher than that of the n-region. Hence the energy barrier for holes will be smaller than that of electron in the heterojunction interface. Again, the decrease of the barrier height with the application of a forward bias to the p-n junction is well known.

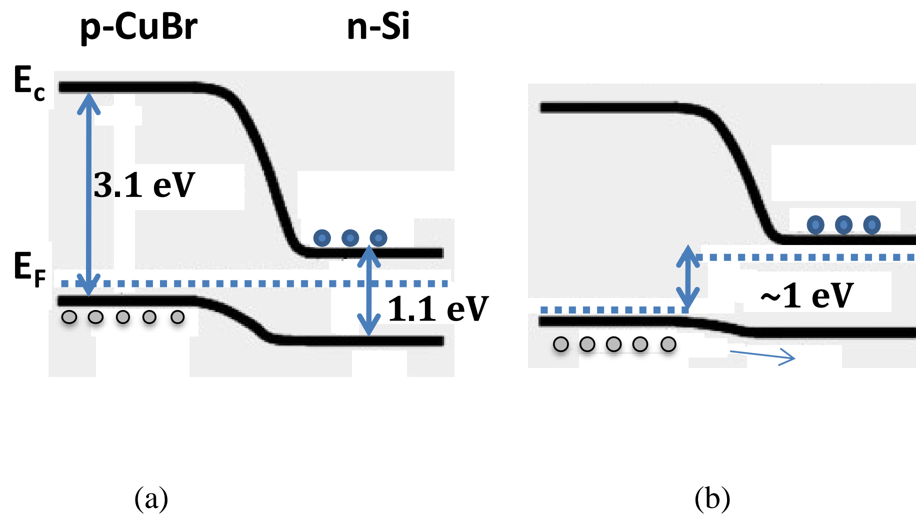

Fig. 6.10: Schematic of the band diagram of the p- CuBr/n-Si heterojunction diode at (a) thermal equilibrium and (b) under forward bias.

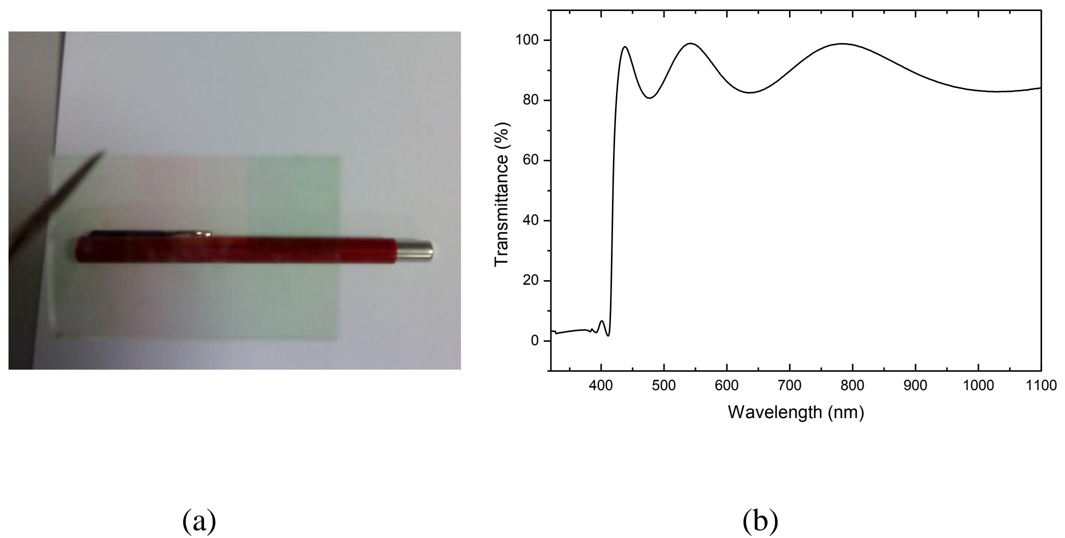

Fig. 6.11: (a) Photograph and (b) Transmittance spectra of a typical p- CuBr film deposited on glass substrate. Both the figures confirm the high transparency of the film in the major part of the visible spectrum.

Here, as the forward bias is applied to the heterojunction, the valence band maximum of Si shifts to a higher energy level and approaches the valence band of p-CuBr, and the barrier to the hole carriers decreases. Thus the application of forward bias of the order of 1 V (Figure. 6.10 (b)) leads to the movement of holes from the valence band of CuBr to the valence band of Si and produces conduction current. Hence the heterojunction can be turned on at a lower voltage of around 1V. Similar kind of lower turn on voltage in the Si based heterojunctions was reported previously [156, 169].

6.4.2 I-V characteristics under illumination

The photoresponsive properties of the p-n junction were studied using the measurement of the I-V characteristics under illumination. The device was illuminated by an incandescent lamp and LEDs. The I-V characteristics under the illumination of an incandescent lamp are shown in figure 6.12. Figure 6.12 shows the I-V characteristics of the heterojunction under dark and illumination. The black curve indicates the dark I-V curve, which was discussed already. When the device is illuminated, the I-V characteristics appear different from that in the dark. It is found that, the heterojunction exhibits rectifying property in the presence of light also. There is no significant change in the forward characteristics of the device with illumination with respect to that in the dark condition. However, illumination has a considerable influence on the reverse characteristics of the heterojunction device. The reverse current shows a drastic increase at the beginning and then gradually saturated after a reverse voltage of 2 V.

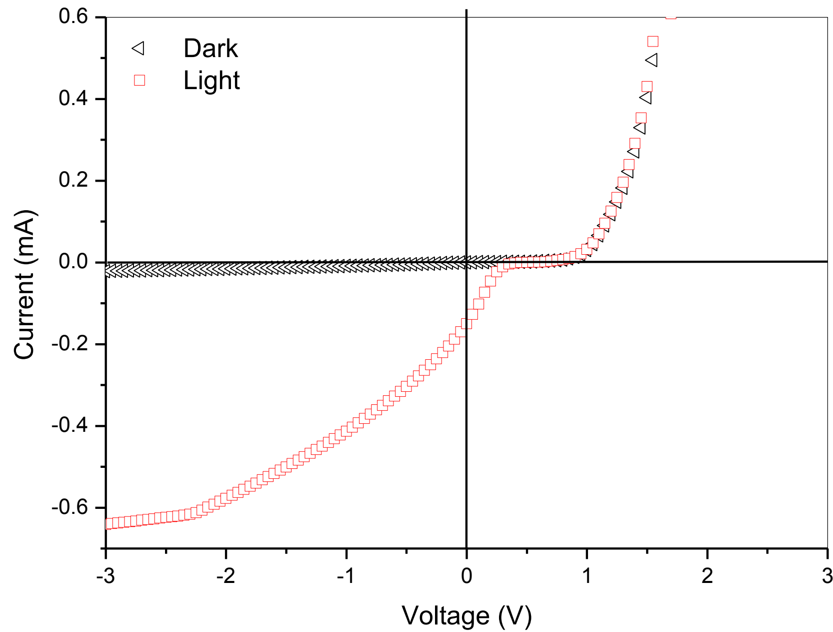

Fig. 6.12: I-V characteristics of the CuBr/Si heterojunction measured under dark and illumination conditions (incandescent bulb). The device structure used is Au/p-CuBr/n-Si/Al.

The photoresponse of the I-V characteristics can be explained as follows. From the transmission spectra of CuBr (figure 6.11 (b)), it is clear that the film is highly transparent (average transmittance > 80 %) for wavelengths above ~ 440 nm in the visible and near IR region. Hence, when the device is illuminated with an incandescent lamp, the wavelengths higher than ~440 nm pass through the CuBr layer without considerable absorption and are absorbed by the underneath Si substrate (figure 6.13). Moreover, energy higher than 3.1 eV is absorbed by the top CuBr layer (figure 5.11). Both these processes generate electron hole pairs which is responsible for the observed photocurrent in the reverse bias condition. It is expected that, the number of photo generated carriers are orders of magnitude less than the number of carriers already present in the device due to doping. Hence, there will not

be any considerable change for the number of majority carriers under illumination compared to that in dark. But conversely, there will be considerable change in the number of minority carriers under illumination, as the number was very small in the dark condition. This is the reason why the top CuBr film act as a good absorber for the short wavelength while, as a window layer for the higher wavelength light.

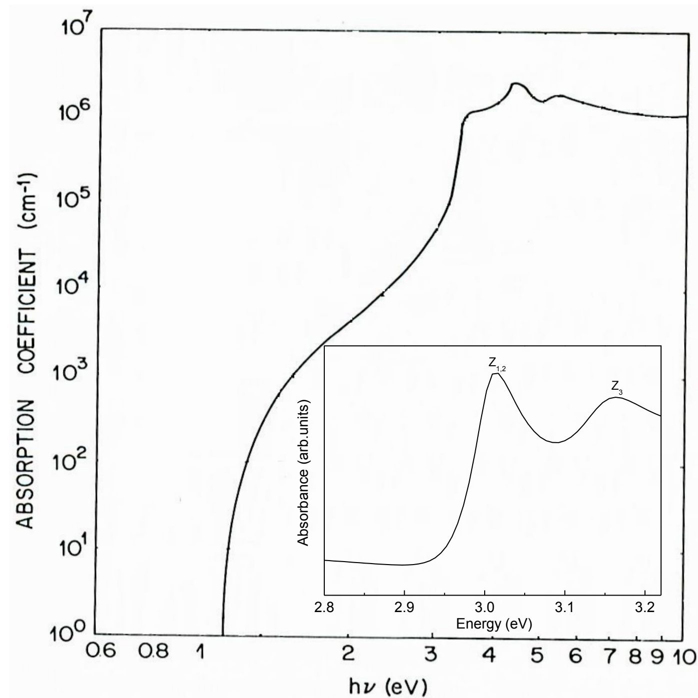

Fig. 6.13: Absorption coefficient of pure Si [160] and absorbance of CuBr on glass substrate (inset) at 300 K.

Figure 6.13 shows the measured absorption coefficient near and above the fundamental absorption edge of pure Si at 300 K [160]. It is clear from the graph that, Si shows good absorption in the whole visible region. The inset graph shows room temperature absorbance of CuBr film deposited on glass substrate.

The response of the CuBr/Si heterojunction with various wavelength illuminations was also studied using red and blue LEDs. The spectral responses from the LEDs are shown in figure 6.14 (a) and it can be observed that the spectral band width is above 20 nm. The influence of the LED illumination on the I-V characteristics of the heterojunction is illustrated in figure 6.14 (b). It can be observed that, the blue illumination has higher impact on the I-V characteristics of the heterojunction. During the red illumination, the top CuBr act as a transparent layer and the light gets absorbed by the bottom Si layer. Hence, the possiblilty of the photogenerated carrier formation is limited only in the bottom layer. But on the other hand, the illumination wavelength of the blue LED is close to the absorption edge of CuBr. Consequently, there is possibility for slight absorption from CuBr layer as well during blue illumination, compared to that during the red illumination. The higher reverse current during the blue illumination attributes to the more effective carrier generation due to the absorption of light at relatively closer position to the junction (in Si) and also might be due to the combined absorption of blue light in the p and n-layers of the heterojunction. Similar observations were reported in ZnO/Si heterojunctions [156].

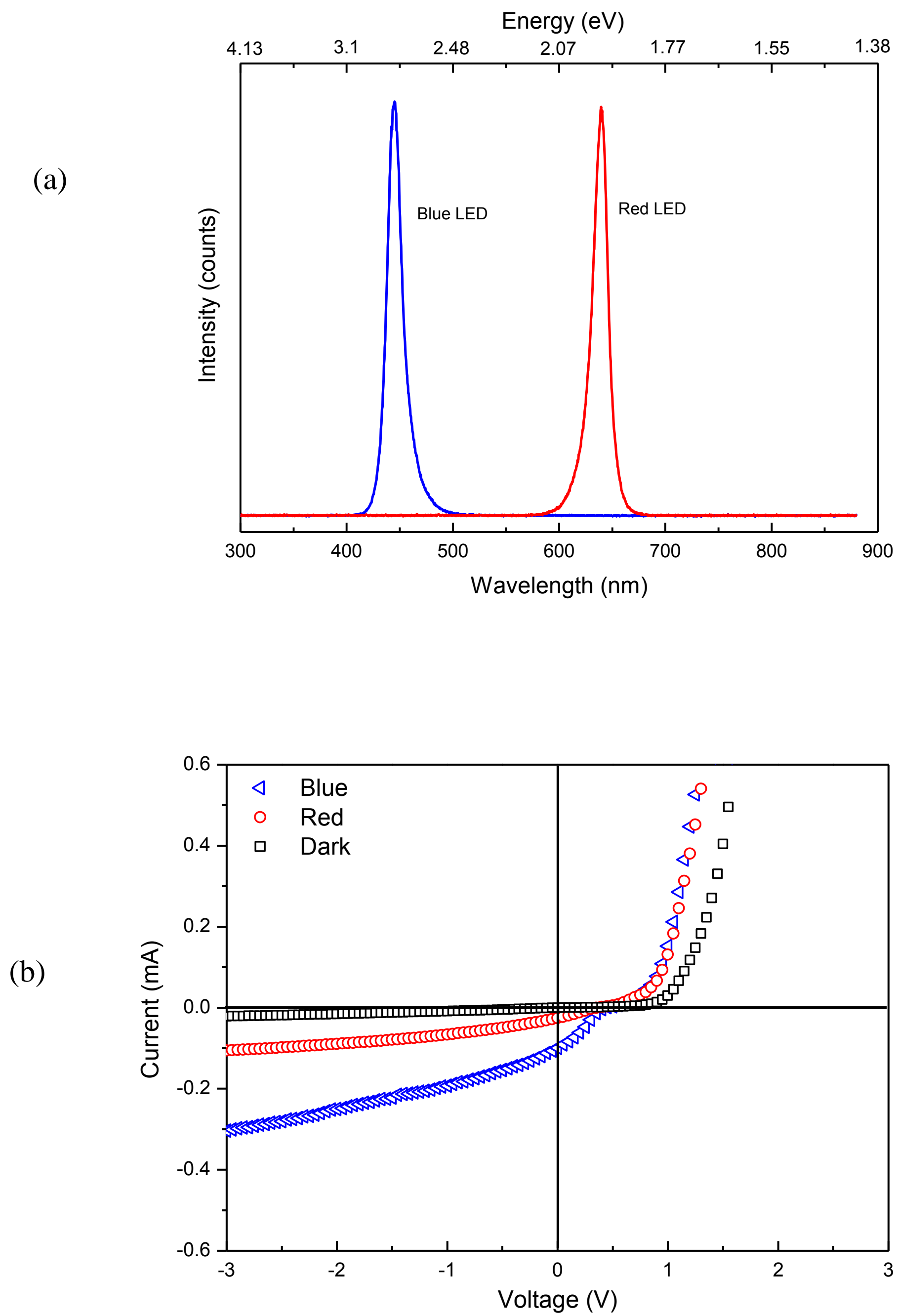

Fig. 6.14: (a) Spectral response from the blue and red LEDs. The plots show spectral width of above 20 nm for both LEDs. (b) Illumination effect due to red and blue LEDs on the I-V characteristics of the heterojunction plotted with the dark curve.

The efficiency of the Si/CuBr heterojunction PV cell can be determined using the J-V characteristics under 85 mW cm^{-2} illuminations. The illumination forces the J-V characteristics to shifts in to the forth quadrant. Figure 6.15 shows the zoomed portion of the J-V curve in the forth quadrant. The zoomed image can be used for the easy extraction of the PV cell parameters from the curve. The figure reveals the values of the open circuit voltage and the short circuit current as 0.475 V and 3.29 mA/cm^{-2}, respectively. The maximum power is the maximum product of the current and voltage that can be obtained among the data points in the forth quadrant. The ratio of this maximum power to the product $V_{oc} \times J_{sc}$ gives the fill factor, FF. The higher the FF, the higher is the electric power that can be extracted

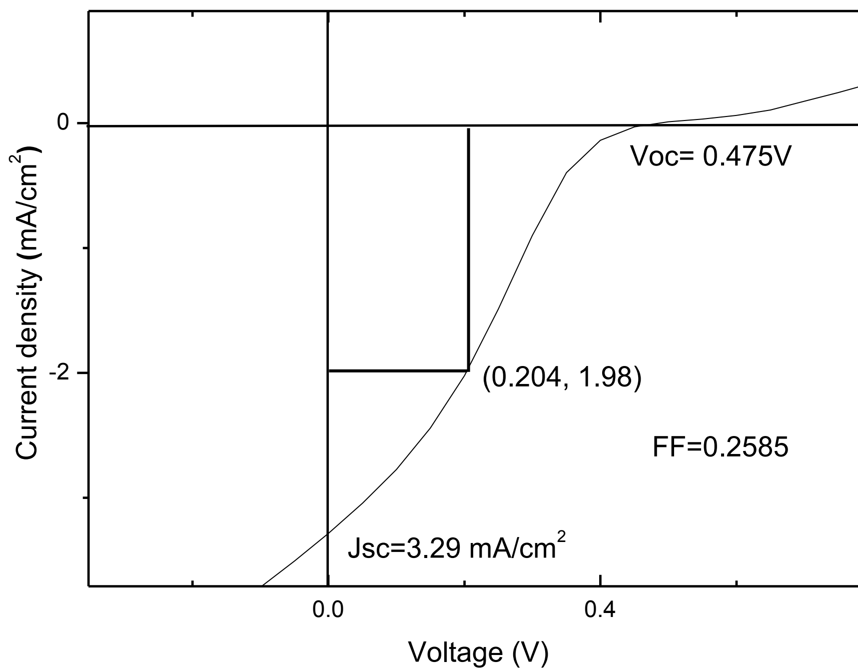

Fig. 6.15: The efficiency calculation of the CuBr/Si PV cell using 85 mW/cm^2 illuminations. The maximum power point, J_{sc}, V_{oc} and FF are indicated in the figure.

In order to determine the power conversion efficiency of the PV cell, the value of the maximum power has to be related to the incident power. According to the data presented here, the efficiency of the PV cell is given by ~ 0.5 %. The measured efficiency is quite low compared to the other well-known inorganic thin film PV technologies. However, we expect an improvement in the efficiency of the cell with AM 1.5 illumination and also by tuning the thickness of the CuBr layer. These processes are underway now. The thickness of both layers should be such that, maximum absorption of light take place close to the junction to reduce recombination possibilities and hence to improve the efficiency.

Figure 6.16 shows the variation of the I-V characteristics with the illumination time. The device was illuminated continuously to 30 minutes and the I-V curve was plotted at every 10 minutes during this time. It was found that there is a slight increase in the forward as well as reverse current with the illumination time. The inset plot represents the variation of short circuit current I_{sc} with respect to the illumination time.

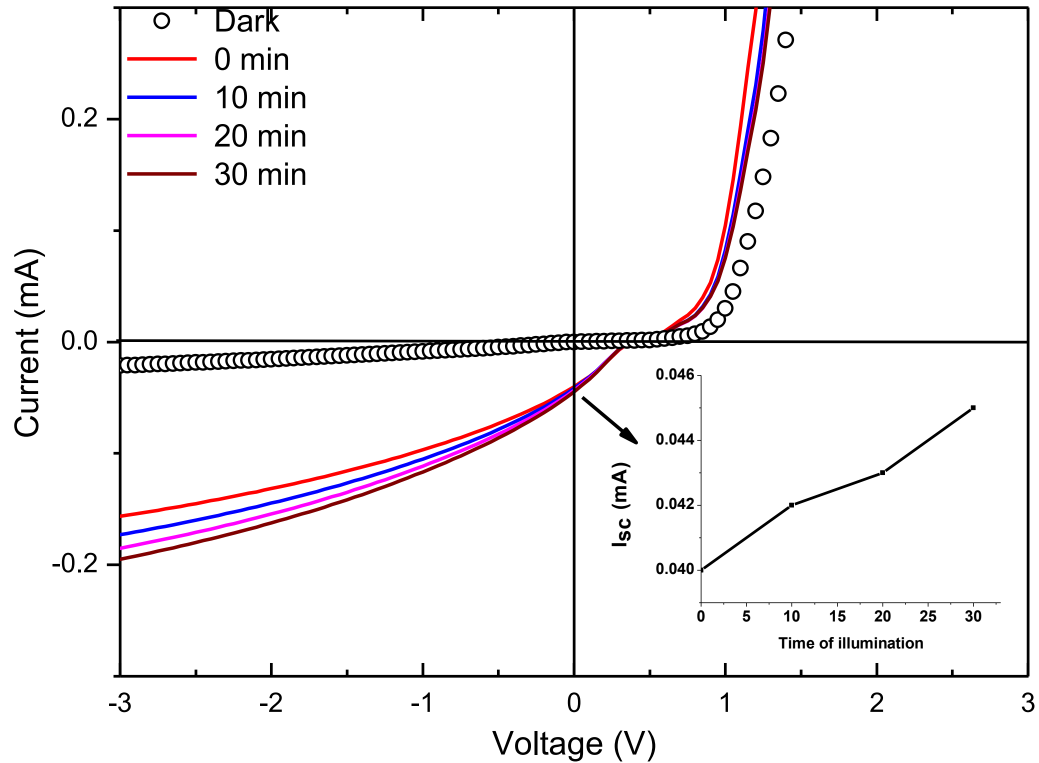

Fig. 6.16: Effect of illumination time on the I-V characteristics of the heterojunction device. The slight changes in the short circuit current as a function of the illumination time are shown in the inset.

There is a linear-like relationship of the I_{sc} with the illumination time. This is expected to be due to the heating of the sample as a result of the continuous exposure to light. The positive temperature coefficient can be explained as due to the effect of thermally excited intrinsic charge carriers along with the narrowing of the band gap of the semiconductors [170]. The effect of temperature on the electrical properties of the PV cell has to be investigated by the I-V measurements at different sample temperatures.

6.4.3 Stability of the device

Although copper bromide has several advantages as a semiconductor, one issue to work with this material is its sensitivity towards the moist air as described in chapter 1.

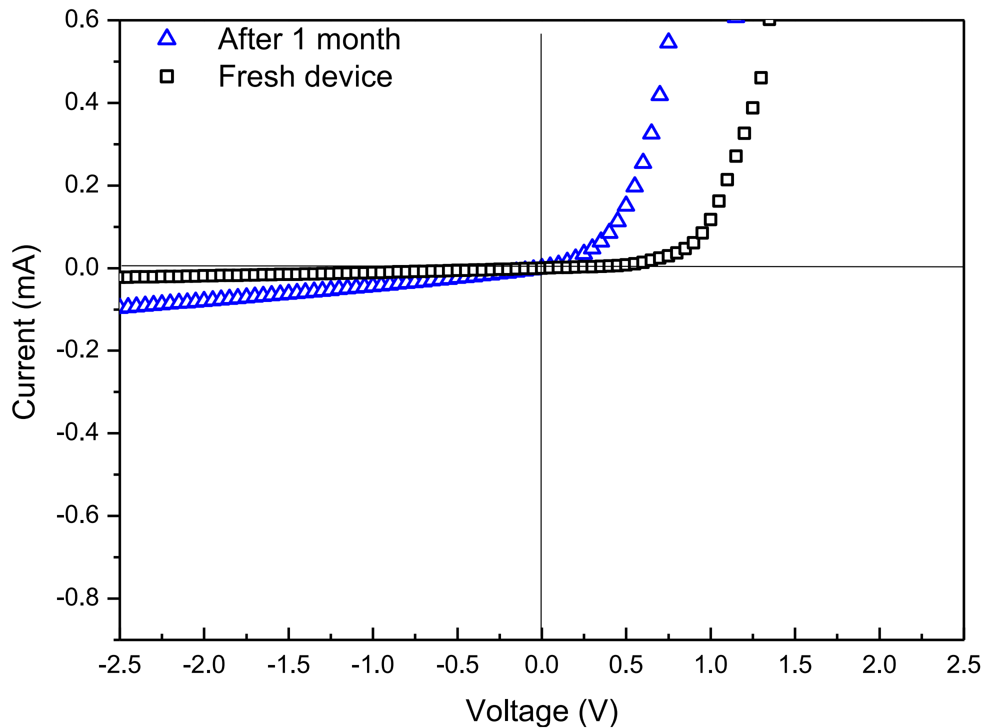

Fig. 6.17: Influence of the aging on the I-V characteristics of the heterojunction

This can be again confirmed using the aging effect studies on the I-V characteristics of the Si/CuBr heterojunction. Figure 6.17 shows the effect of aging on the properties of the heterojunction. The variation of the IV characteristics of the heterojunction with the time of exposure of the device in to the ambient atmosphere is illustrated in the figure. The black curve indicates the I-V characteristics of the freshly made device. The blue one represents that after 1 month of exposure of the device in the ambient. The decrease in the turn on voltage, and the increase in the reverse leakage current is attributed to the degradation of the CuBr layer due to

exposure to the ambient atmosphere, and thereby the degradation of the junction. But this issue can be solved by the use of a capping layer on the top of the CuBr layer [36, 171].

6.5 Summary:

p-CuBr/n-Si heterojunction is fabricated and the I-V characteristics were investigated. The diode characteristics of the junction were confirmed by the rectifying feature of the I-V curve. Low leakage current of the diode under reverse bias condition was also established. A turn on voltage of ~ 1V was revealed from the I-V characteristics of the diode. The realisation of the CuBr/Si PV cell was also discussed. PV parameters of the heterojunction were investigated from the J-V characteristics of the junction under illumination. The efficiency of the PV cell under 85 mW/cm^2 illuminations was also determined. The influence of the blue and red illumination on the I-V characteristics of the heterojunction was studied. The effect of illumination time was also established. It is also measured recently that, the device gives an efficiency of ~1.2% with an AM 1.5 illumination. This value indicates the importance of further exploration of this device.

Chapter 7

Development of ultra thin chromium transparent contacts

7.1 Introduction

Realization of reliable and low cost transparent conductive materials is a vital challenge for the modern optoelectronic industry. These materials are very important for applications such as light emitting diodes, photo detectors, solar cells and surface emitting laser diodes [172-176]. Nowadays transparent conductive oxides (TCOs) are extensively used for these applications [177]. They are highly-doped wide band gap semiconductors, and the most commonly used one is Indium tin oxide (ITO). Even if it has an excellent combination of low electrical resistivity and high optical transmittance in the visible (VIS) region, some of the drawbacks of ITO lead to the search for an alternative material. These drawbacks include the need for post deposition annealing, incompatibility with organic LEDs due to the diffusion of oxygen and indium into the active organic layers [178-179], reduced transparency in the UV and IR region, high cost of production, and the toxic nature of indium metal. Moreover, the work function of the ITO surface strongly depends on the cleaning methods [180].

It has been reported that ultra thin metal films could be a better alternative to the transparent conductive oxides [181-183]. When the thickness of the metallic film is reduced to a sufficiently low value, it can be used as an optically transparent material

with excellent electrical properties. If ultra thin films of metals like chromium can be controllably deposited by some straightforward and commercially viable methods, it could resolve some of the technical drawbacks associated with the TCOs. The realisation of ultra thin chromium film developed by bipolar pulsed dc magnetron sputtering, and the effect of sputtering parameters on the electrical properties of the film are investigated in this chapter.

D. S. Ghosh *et al*. have recently reported the optical and electrical properties of dc sputtered chromium film [181]. Here, the advantages of bipolar pulsed dc sputtering over dc sputtering have been exploited in the deposition of ultrathin metallic films as transparent electrodes. The former has higher ion current density, self bias voltage and thermal substrate load compared to the latter, which is due to the strong ion and electron bombardment on the substrate thereby producing denser and hence lower resistivity films compared to dc sputtering [184].

7.2 Experimental details

Ultra thin chromium films were prepared by bipolar pulsed dc magnetron sputtering of a chromium target onto optically polished glass and silicon substrates. Prior to deposition the substrates were ultrasonically cleaned by acetone, trychloroethane, methanol and de-ionized water and blown dry with a nitrogen gun. An ENI RPG-100 pulse generator was used to drive a planar magnetron fitted with the chromium target in the power regulation mode. The target was 99.99% pure chromium with 50 mm diameter and 6 mm thickness supplied by the Kurt J. Lesker Company. The chamber was first pumped down to a base pressure of $7x10^{-7}$mbar by cryogenic pumping. Sputtering was carried out in pure argon atmosphere and the gas flow rate was adjusted to 2 sccm using a mass flow controller. During deposition, the chamber

pressure was 0.36 Pa. The distance between target and substrate was 9 cm. The target was pre-sputtered for 10 min prior to the deposition, to avoid contamination of the deposited film and to get a stable plasma discharge. A constant pulse frequency of 100 KHz was used in all experiments. The thicknesses of the films were first measured using Profilometer and later on controlled by adjusting the sputter deposition time (the thickness can be inferred from the deposition rate ~ 6 nm/m). The surface morphology of the films was studied by Atomic force microscopy (AFM). A four point probe was used to investigate the electrical resistivity of the film. The effect of sputtering parameters such as target power and pulse duty cycle on the electrical resistivity of the thin film was also explored. A Perkin Elmer Lambda 40 spectrometer was used to analyse the optical transmittance of the films.

7.3 Results and discussion

7.3.1 Variation of resistivity with thickness

In order to develop a transparent conducting film, it is highly essential to investigate the influence of thickness on the resistivity of the film. Our findings show that, the resistivity and the transmittance of the ultra thin Cr films are highly dependent on their respective thicknesses. So as to investigate the effect of thickness on the resistivity, Cr films are deposited at a constant target power of 100 W and a pulse duty cycle of 10%. Films with thicknesses less than 10 nm were developed by varying the deposition time. The variation of resistivity as a function of thickness is plotted in figure 7.1.

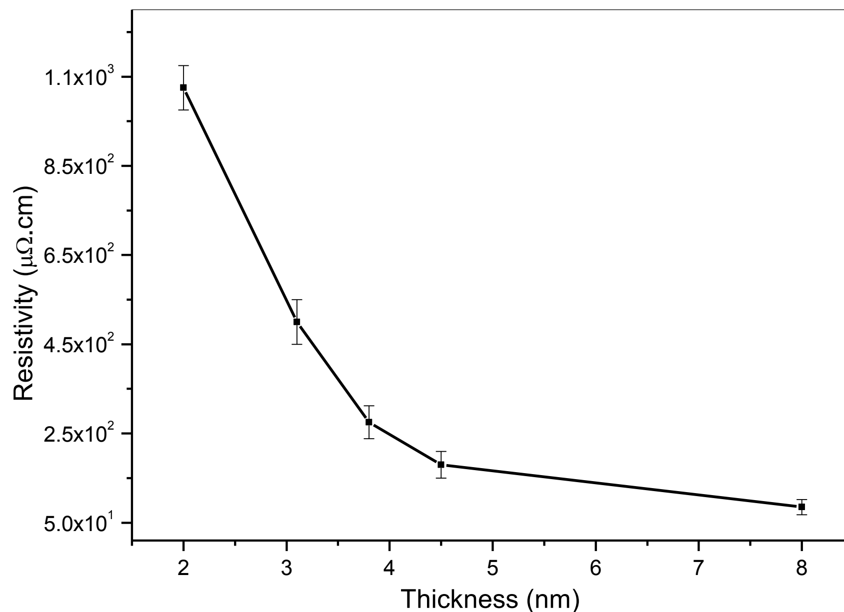

Fig. 7.1: Variation of resistivity of Cr- films as a function of thickness. All the films were deposited under identical experimental conditions (target power = 100 W and pulse duty cycle = 10 %).

The graph indicates a drastic decrease in the resistivity from ~ $1x10^3$ μΩ cm for a film of thickness 2 nm to ~ $8x10^1$ μΩ cm for an 8 nm thick film. It is well known that the resistivity of the polycrystalline films is higher than its single crystalline version. It was first reported by Fuchs and Sondheimer (FS) [185-186] that, the resistivity of the metallic films increases with decreasing thickness as soon as the thickness becomes comparable to the electron mean free path. According to FS theory, the aforementioned size effect (thickness dependence of resistivity) is due to the scattering of the conduction electrons at the surface of the film and at the interface. On the basis of these assumptions, they added an additional resistivity term to the intrinsic resistivity, when the film thickness becomes less than the mean free path of the conduction electrons. Furthermore, in the case of polycrystalline materials, the effect of grain boundary scattering would also be considered, when the distance between grain-boundaries become comparable to the electron mean free path. Hence, the increase in resistivity of ultra thin Cr films with decrease of thickness can be attributed to the presence of the surface scattering and grain boundary scattering of electrons.

7.3.2 Variation of transmittance with thickness

The investigation of the influence of thickness of the Cr film on the transmittance is highly essential for the development of ultra thin transparent conducting contacts based on this material. The optical transmission of the films in the wavelength region of 350 nm to 1000 nm has been studied with films of different thicknesses. These results are illustrated in figure 7.2. It is clear from the plot that, an average transmittance of greater than 65 % is achieved for films of thicknesses less than 4.5 nm. Film of thickness 2 nm shows an average transmittance of ~ 90 %, and it reduces to ~ 48 % for an 8 nm thick film. Hence it is possible to develop a film of above ~85 % transparency using Cr metal, when the thickness is reduced to less than 3 nm (Figure 7.3). Photograph of a highly transparent Cr film deposited on glass substrate is also presented here.

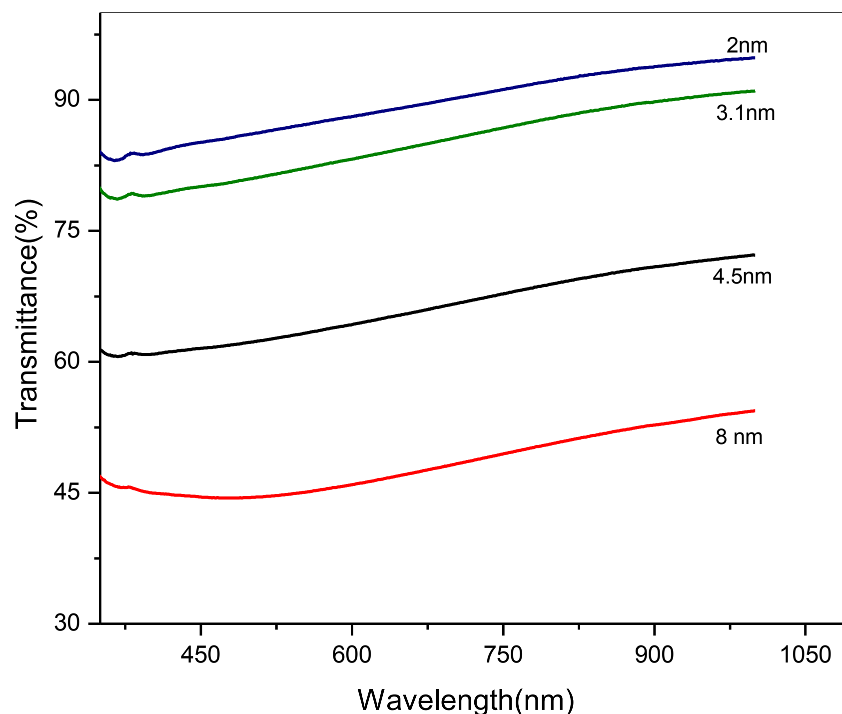

Fig. 7.2: Optical transmittance plotted against wavelength for Cr films of various thicknesses. The measurements were performed under identical conditions.

(a)

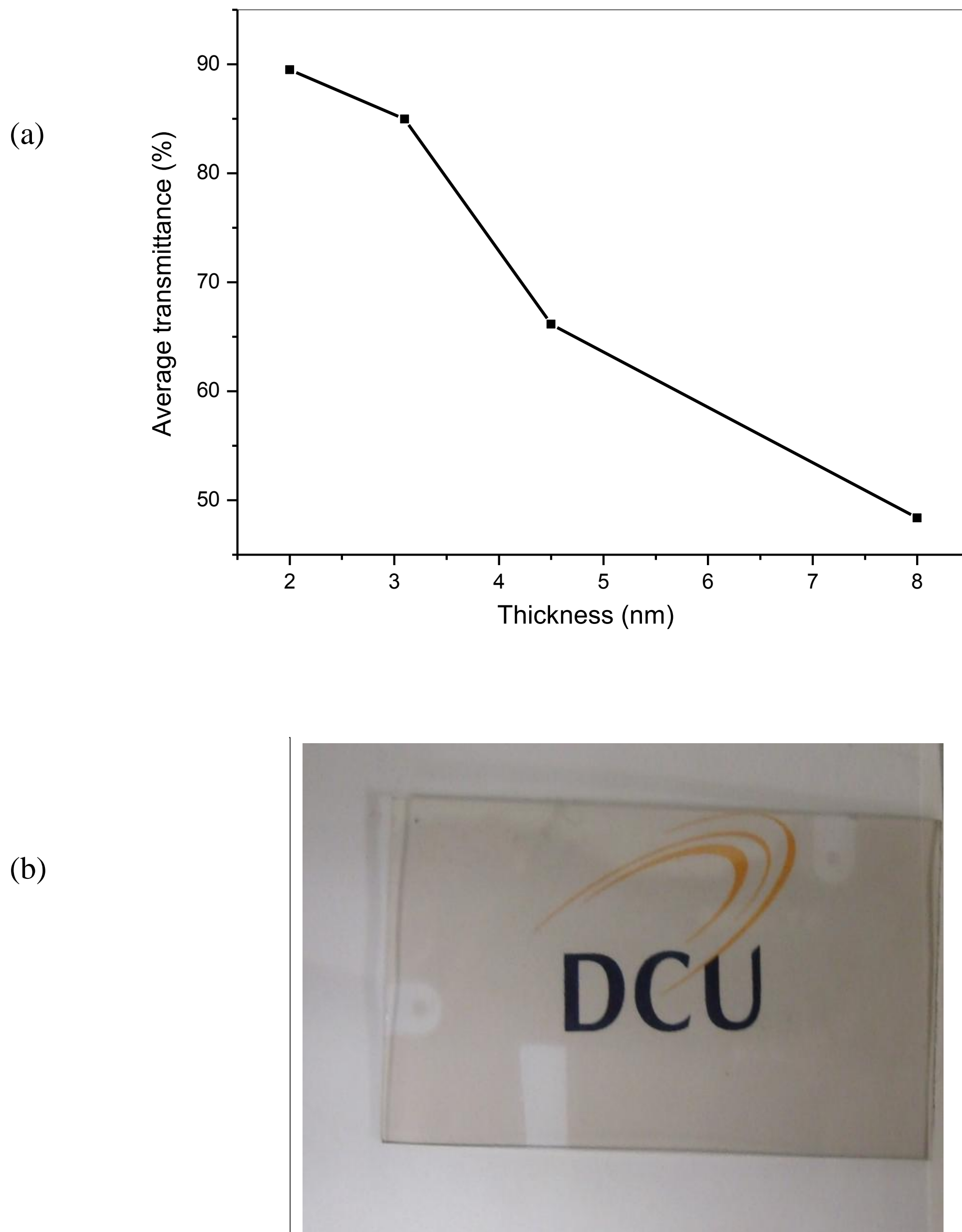

(b)

Fig. 7.3: (a) The variation of average transmittance of the Cr films as a function of thickness measured under identical conditions, (b) Photograph of ultrathin Cr film deposited on glass substrate (thickness=2.8 nm).

The average transmittance of the films with different thicknesses plotted against resistivity is illustrated in figure 7.4. This would be helpful to select the thickness of the film to get a desirable combination of transmittance and resistivity.

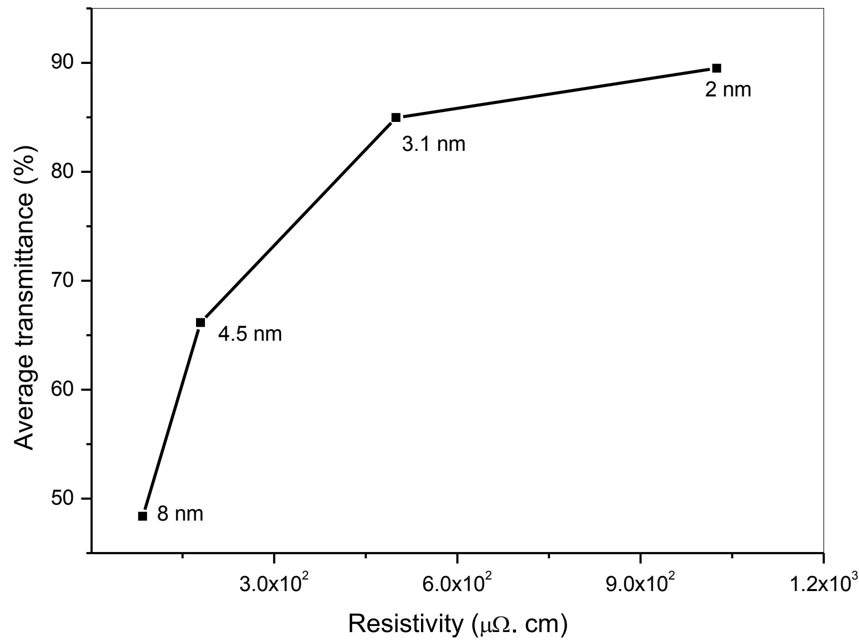

Fig. 7.4: Variation of average transmittance plotted against resistivity of the films. The corresponding thicknesses are also indicated in the figure.

Our findings reveal that, a combination of average transmittance of 90 % and resistivity of the order of $1x10^{-3}\mu\Omega$ cm can be achieved for a film deposited on glass substrate, at room temperature. Furthermore, both average transmittance and resistivity reduced to 85 % ($5x10^2$ $\mu\Omega$ cm), 66 % ($1.8x10^2$ $\mu\Omega$ cm) and 48 % ($8.5x10^1$ $\mu\Omega$ cm), respectively for films of corresponding thicknesses 3.1 nm, 4.5 nm and 8 nm.

A typical AFM image of the surface of a film of thickness 5 nm deposited on Si substrate is illustrated in figure 7.5. The measured RMS roughness of the film was 3.4 nm, on a Si substrate with an RMS roughness of ~ 1.3 nm. Similarly for the 2 nm

thick film, the RMS roughness was 1.85 nm. Here the transmittance has been studied mostly in the visible region.

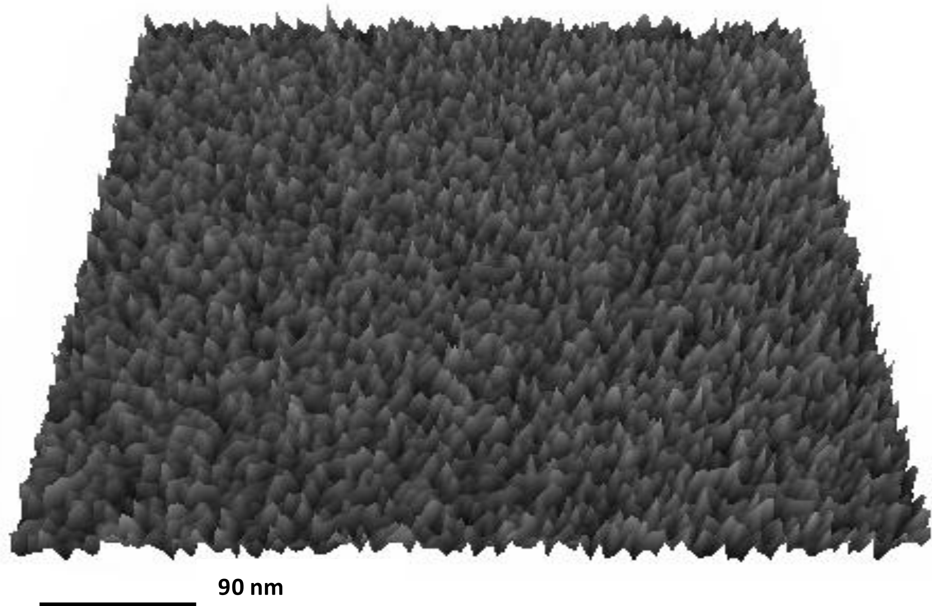

Fig. 7.5: AFM image of a typical chromium film of thickness 5 nm
(maximum z- height is 3.5 nm)

However, it has already been reported by D. S. Ghosh *et al*. [181] using dc sputtering that, the ultra thin Cr films are highly transparent in the UV as well as in the IR region. Thus these films can be used in the complete range from UV to IR.

7.3.3 Effect of target power on resistivity

The pulse parameters used for the deposition of the films have to be optimised to develop a transparent contact with a combination of maximum transparency and minimum resistivity. The influence of target power on the resistivity of the films is

studied by depositing films of constant thickness at various target powers at constant pulse duty cycle and frequencies.

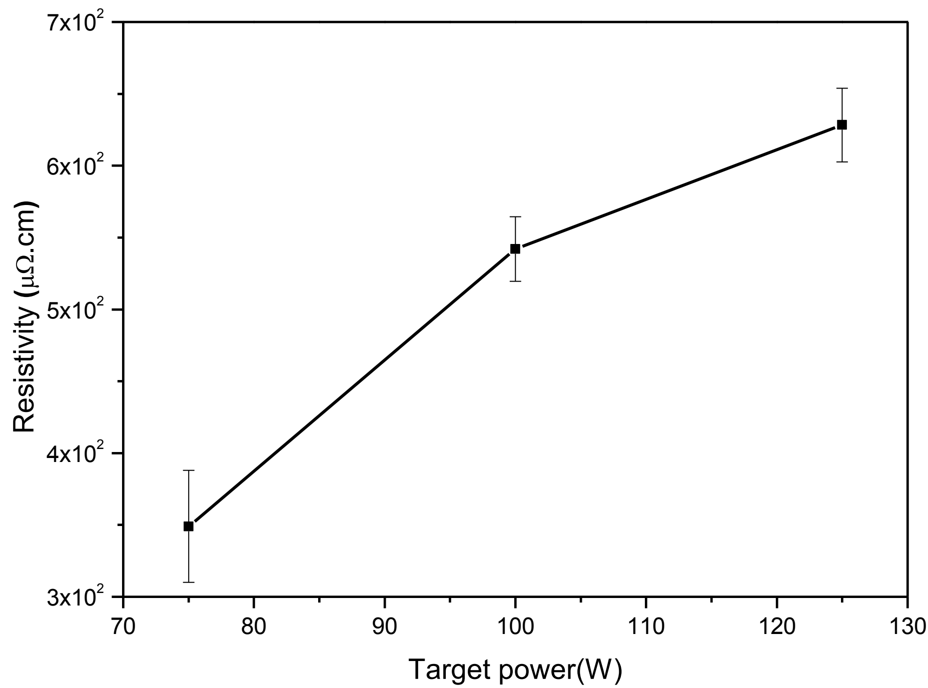

Fig. 7.6: Variation of resistivity of the Cr film as a function of target power used for deposition. All experiments were carried out at identical conditions (duty cycle = 10 % and pulse frequency = 100 KHz).

The deposition of the films is performed at 3 different target powers of 75 W, 100 W and 125 W at a 10 % pulse duty cycle and at a frequency of 100 kHz. The resistivities of these films were measured and were plotted as shown in figure 7.6. The target power has influence on resistivity of the film. A monotonic increase in resistivity from $3.5x10^2$ μΩ cm to $6.3x10^2$ μΩ cm has been observed with an increase in target power from 75 W to 125 W. An increase of magnetron voltage from 350 V to 420 V with a corresponding increase of current from 0.21 A to 0.29 A is observed for an increase of target power from 75 W to 125 W. As the target power is increased, the film experiences bombardment with higher energy sputtered particles.

This will most likely create defects in the thin film, thereby cause an increase in carrier scattering. Thus the resistivity increases with the target power. An increase of the RMS surface roughness from 1.73 nm to 2.1 nm is also noticed for a film of thickness 3.5 nm with an increase of target power from 75 W to 125 W.

7.3.4 Influence of pulse duty cycle on resistivity

The influence of pulse duty cycle on the resistivity of the film is investigated as part of the optimisation of the deposition parameters of the film. Figure 7.7 shows the dependence of the resistivity of the film on pulse duty cycle at a target power of 100 W. It is found that the resistivity of the film gradually decreases as the duty cycle increases from 10-20 %, and then begins to increase as the duty cycle rises to 30 %. There is a reduction in the magnetron voltage (from 386 to 339 V) and an increase in the magnetron current (from 0.25 to 0.29 A) corresponding to the increase of duty cycle from 10 to 30 %. A decrease in resistivity of ITO films with increase in the pulse duty cycle is also reported by W. J. Lee *et al*. [187].

S. H. Seo *et al*. reported that as the duty cycle is reduced, the cathode voltage and current, and thus the cathode delivered power at the pulse-on phase rapidly increases in the constant power mode [188]. Further to this, H. Bartzsch *et al*. reported that both the ion current density and self-bias voltage increase with decreasing duty cycle at constant frequency and sputtering power, which leads to an increase in the substrate bombardment with the ions and electrons from the plasma at lower duty cycles [184]. Again an enhancement of free electron mobility and deposition rate with an increase in the pulse duty cycle has previously been reported [187, 189]. In the present case (figure 7.7), at a very low duty cycle of 10%, the film undergoes higher ion and electron bombardment, which in turn leads to damage of

the film. Furthermore, the lower adatom mobility and deposition rate would make the film less dense at lower duty cycle [190]. All these effects combine to give a film of higher resistivity at lower duty cycle.

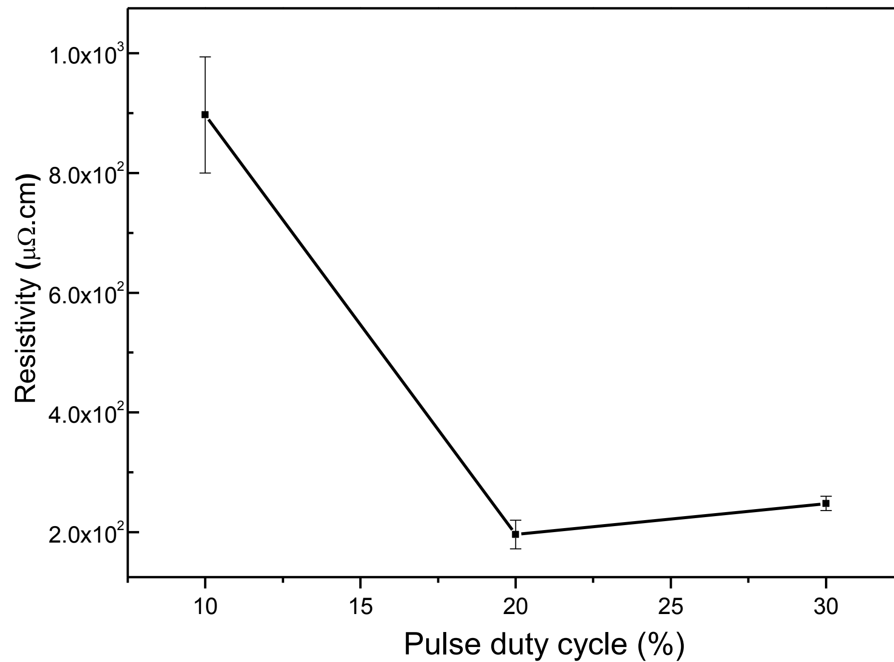

Fig. 7.7: The variation of resistivity of Cr film as a function of pulse duty cycle used for the deposition. All experiments were performed at a target power of 100 W and at a pulse frequency of 100 KHz.

As the duty cycle increases to 20 %, the substrate bombardment turns out to be less vigorous and tends to produce denser and less resistive films, without causing any damage. The increased mobility at this higher duty cycle is also favourable for the formation of lower resistivity films. Again, as the duty cycle increases further to 30 %, the substrate bombardment becomes less effective in producing denser films, and the effect of deposition rate dominates, and the resistivity begins to increase slightly. It is clear from the observations that the present method can offer ultra thin

chromium films with improved resistivity compared to the previously reported results [181]. The resistivity can be further improved by selecting a suitable combination of target power and pulse duty cycle.

The influence of aging of the Cr films was also investigated by looking at the transmittance and resistivity data after nearly 1.5 years. It was found that, there was no considerable variation (2-3 %) of the transmittance data with aging of the film. There was slight (~ 0.5 μΩ cm) increase in the resistivity values, which was more prominent for very thin films of < 2 nm. But for films having thicknesses > 3 nm, the effect was negligible.

7.4 Summary

The growth process and characterisation of ultra thin chromium transparent metal contacts, deposited by pulsed dc magnetron sputtering at room temperature without any post deposition annealing have been discussed in this chapter. The effect of target power and pulse duty cycle on the resistivity of the film is investigated. We find that the resistivity of the film increases with target power, and there is an optimal value of the duty cycle to produce a film of lowest resistivity at constant target power and pulse frequency. Hence from these observations it is expected that ultra thin chromium metallic films deposited by bipolar pulsed dc magnetron sputtering can perform as an effective alternative to the transparent conductive oxides. Cr film deposited at optimized conditions of target power (75 W) and pulse duty cycle (20 %) found to have resistivity and average visible transparency of the order of $\sim 4\times10^2$ μΩ cm and ~ 85 % , respectively, close to the corresponding values of ITO films ($\sim 5\times10^2$ μΩ cm and ~ 85%).

Chapter 8
Conclusions and future works

8.1 Conclusions

Among the wide band gap materials which show numerous functional properties depending on their crystal structure, morphology and optoelectronic properties, my studies focused on the cuprous halides (CuCl and CuBr). These materials appear as promising candidates for the future optoelectronic applications due to their high excitonic binding energies. These are very poorly conducting materials, and hence need to be doped to improve the conductivity, which is crucial for the future applications. The higher excitonic binding energies of these materials strengthen the importance of the exploration of their utility towards the realization of the exciton based light emitting devices. Moreover, good conducting p-type CuBr was developed in this work, exhibits high transparency in the major part of the visible spectrum, along with its good absorption in the UV and violet/blue region. The investigation of the appropriateness of this material as both a window layer and a heterojunction partner for the phototvoltaic cell is a matter of very high interest, since the development of a p- type transparent conducting material is a difficult job [1].

The successful development and characterization of the n-CuCl grown by the doping of CuCl using Zn are described in the third chapter of the thesis. The structural and the morphological properties of the n-type CuCl, deposited by pulsed dc magnetron sputtering of the CuCl:Zn target, are studied using XRD and SEM measurements. It

is observed that, there is no structural deformity for the CuCl by doping with Zn up to 5 %. But instead, an improvement in the crystallinity of CuCl is noticed with the doping of Zn up to 3 %. Higher doping concentration of Zn (5 %) is found to reduce the crystal quality of CuCl. Hence, among the various doping concentration studied, 3 % was found to be the optimum. Absorption and PL studies on the undoped and doped CuCl samples confirmed that, there is no significant degradation of the absorption and luminescence properties of the CuCl with doping. High UV emission from the doped samples is also verified. The n-type conductivity of the Zn doped CuCl samples are confirmed using the Hall effect experiments. An order of magnitude reduction in the resistivity of CuCl is achieved by doping with Zn (~ 6 Ω cm for 3 %). The carrier mobility and the carrier concentration of the 3 % Zn doped samples are found to be, respectively ~ 0.1 $cm^2V^{-1}s^{-1}$ and $9.8x10^{18}$ cm^{-3}.

Since Zn performs the role of a good n-type dopant for CuCl, it is highly worthwhile to investigate the effect of doping on the electronic structure of CuCl. The results of the photoemission studies on the undoped and the Zn doped CuCl are described in chapter 4. The variation of Cu 2*p* and Cl 2*p* core level spectra of the CuCl as a function of Zn doping reveal the presence of cupric species in the undoped sample. The occurrence of the cupric species is found to decrease and disappear as the concentration of Zn in the film increases. There was almost no sign of the presence of the cupric species in the 3 % Zn doped CuCl sample. Moreover, the investigation of the valence band spectra of the doped samples indicates a shift towards the higher binding energy side with respect to that of the undoped sample with the increase of concentration of Zn in the film. A maximum shift of 0.22 eV was observed for the 5 % doped sample. This specifies the filling of the conduction

band of CuCl with the doping of Zn, which thereby supports the reduction of resistivity of the doped samples described in chapter 3.

The growth and optoelectronic characterization of the p-CuBr film is described in chapter 5. The films are developed by the vacuum evaporation of CuBr followed by the oxygen plasma exposure. Our findings prove that, oxygen act as a good acceptor for CuBr. There are no noticeable changes for the structural and optical properties of CuBr under oxygen doping, provided the plasma exposure time does not exceed a certain limit. The doped films showed good transparency along with high emission in the violet/blue region. The investigation of the electrical properties revealed that, the resistivity of the doped films is very low, of the order of ~1 Ω cm (3 min exposure). The corresponding hole mobility and hole concentration of the aforementioned films were, respectively, 0.24 $cm^2V^{-1}s^{-1}$ and 7.5×10^{19} cm^{-3}. SIMS analysis on the doped films reveals that the diffusion of oxygen is quite good in the CuBr films.

Realization of the heterojunction diode based on p-CuBr/n-Si structure is described in chapter 6. It is found that I-V characteristics of the heterojunction device show good rectifying behaviour with a turn on voltage of ~ 1 V, with quite low leakage current (2×10^{-5} A). The lower turn on voltage of the diode compared to the band gap of CuBr was explained with the aid of a schematic band diagram. Again, the photo response of the heterojunction is investigated by measuring the I-V characteristics under illumination. It is found that, the top CuBr layer act as a window layer for the PV cell for major part of the visible spectrum, and absorbs well in the UV/blue region and contributes photogenerated carriers for conduction. The generation of the carriers is confirmed by the appearance of increased reverse current in the I-V characteristics under illumination. The response of the cell under the

illumination of the red and blue LED indicated that, there are more carrier generation under blue illumination than red. This is assumed to be due to the additional carrier generation due to absorption of CuBr in this region. The effect of illumination time on the I-V characteristics was also established.

The development of a transparent conducting contact, which can be used as an alternative to the most common ITO, is a novel work and could be useful for the realization of the p-n junction devices based on CuX as well as other materials. Chapter 7 explains the growth and development of the ultrathin Cr-based transparent electrodes, using pulsed dc magnetron sputtering. The influence of film thickness on the resistivity and transmittance was investigated. Again, the variations of resistivity of the films as a function of pulse parameters were also described.

8.2 Future directions

After the successful deposition of the highly luminescent p and n-type Cu-halide materials, the important future work could obviously include the fabrication of a light emitting device based on these materials. This process is in progress now. Although, the Zn doped CuCl films show good optical properties along with high electron concentration, the electron mobility must be increased for better performance of the devices based on these films. Hence, more knowledge of the conduction mechanism is essential to improve the carrier mobility in these doped films. Future work could include the study of the influence of temperature on the conduction properties of the films.

The exploration of the conduction mechanism in the p-CuBr would also be a field of interest for the future studies. Annealing experiments to improve the hole mobility of the films could also be tried. XPS measurements would be advantageous to investigate the influence of oxygen doping on the band structure of CuBr, which is important to illustrate the band diagrams of the p-n structures based on this material.

Several interesting projects can be suggested for the improvement and understanding of the CuBr/Si heterojunction PV cell. The efficiencies of the PV cells have to be measured using standard AM 1.5 light source to get the actual value and the wavelength dependent measurements have to be carried out. It is also important to understand the influence of the thickness of CuBr film or Si wafer on the photovoltaic efficiency of the device. The thickness of both p and n-layers has to be adjusted to make maximum absorption close to the junction to improve the efficiency of the device by reducing carrier recombination. A complete elucidation of the conduction properties of the junction has to be developed based on the band diagrams. The effect of presence of an interfacial SiO_2 layer on the photovoltaic properties of the device could also be investigated. The variation of the photocurrent as a function of temperature can also be studied. Another important study could include the development and studies of CuBr based p-n heterojunctions with more lattice matched substrates than Si. That would improve the performance of the PV cell made out of these materials.

References:

1) A. Kuramata, K. Horino and K. Domen, *FUJITSU Sci. Tech.*, J. **34**, 2 (1998).
2) Z. I. Alferov, *Sov. Phys. Usp.,* **15**, 834 (1973).
3) J. S. Preston, *Poc. Roj. Soc. (Lond.)* Series A, **202,** 449 (1950).
4) H. Kroemer, *Proc. IRE*, **45**, 1535 (1957).
5) H. Kressel and J. K. Butler, *Semiconductor Lasers and Heterojunction LEDs*, Academic Press, New York (1977).
6) R. L. Anderson, *Solid State Electronics*, **5,** 341(1962).
7) P. Wurfel, *Physics of Solar Cells from Basic Principles to Advanced Concepts*, Wiley-Vch Verlag GmbH & co. Weinheim (2009).
8) A. K. Sreedhar, B. L. Sharma and R. K. Purohit, *IEEE T. Electron Dev*., **3**, 309 (1969).
9) S. Guha, J. Yang, and A. Banerjee, *Prog. Photovolt. Res. Appl.* **8**, 141 (2000).
10) H. -W. Schock and R. Noufi, *Prog. Photovolt. Res. Appl*. **8**, 151 (2000).
11) P. Sheldon*, Prog. Photovolt. Res. Appl.* **8**, 77 (2000).
12) I. Akasaki and H. Amano, *Jpn. J. Appl. Phys*. **36**, 5393 (1997).
13) F. A. Ponce and D. P. Bour, *Nature*, **386**, 351 (1997).
14) J. Han, M. H. Crawford, R. J. Shul, J. J. Figiel, M. Banas, L. Zhang, Y. K. Song, H. Zhou and A. V. Nurmikko, *Appl. Phys. Lett*., **73**, 1688 (1998).
15) S. Nakamura, M. Senoh, N. Iwasa, S. Nagahama, T. Yamada and T. Mukai, *Jpn. J. Appl. Phys*. **34**, L1332 (1995).
16) O. Ambacher**,** J. Phys. D: *Appl. Phys*. **31,** 2653 (1998).
17) H. Yoshida1, M. Kuwabara, Y. Yamashita, Y. Takagi, K. Uchiyama and H. Kan, *New J. Phys.***11,** 125013 (2009).

18) Y. K. Su, S.J. Chang, C.H. Ko, J.F. Chen,W.H. Lan,W.J. Lin, Y.T. Cherng, and J. Webb, *IEEE Trans. Electron Dev.* **49**, 1361 (2002).

19) T.C.Wen, S.J. Chang, L.W.Wu,Y.K. Su,W.C. Lai, C.H. Kuo, C.H. Chen, J.K. Sheu and J.F. Chen, *IEEE Tran. Electron Dev.* **49**, 1093 (2002).

20) C.H. Kuo, S.J. Chang, Y.K. Su, J.F. Chen, L.W. Wu, J.K. Sheu, C.H. Chen, and G.C. Chi, *IEEE Electron Dev. Lett.* **23**, 240 (2002).

21) J. I. Pankov, E. A. Miller and J. E. Berkeyheiser, *RCA Rev*. **32,** 383 (1971).

22) H. Amano, M. Kito, K. Hiramatsu and I. Akasaki, *Jpn. J. Appl. Phys*.**28**, L2112 (1989).

23) X. Li, S.G.Bishop and J. J. Coleman, *Appl.Phys.Lett.* **73,** 1179 (1998)**.**

24) H. Marchand, X.U. Wu, J.P. Ibbetson, P.T. Fini, P. Kozodoy, S. Keller, J.S. Speck, S.P. DenBaars and U.K. Mishra, *Appl. Phys. Lett.,* **73**, 747 (1998).

25) T. Mukai, K. Tadekawa and S. Nakamura, *Jpn. J. Appl. Phys.,* **37**, L839 (1998).

26) B. Monemar, Phy.Rev.B **10,** 676 (1974).

27) D. M. Bagnall, Y. F. Chen, Z. Zhu, T. Yao, S. Koyama, M. Y. Shen, and T. Goto, *Appl.Phys. Lett.* **70,** 2230 (1997).

28) P. Zu, Z. K. Tang, G. K. L. Wong, M. Kawasaki, A. Ohtomo, H. Koinuma and Y. Segawa, *Solid State Commun.* **103,** 459 (1997).

29) D. C. Look and B. Claflin, *Phys. Status Solidi B* **241,** 624(2004).

30) C. G. van de Walle, *Phys. Rev. Lett.* **85,** 1012 (2000).

31) B. Theys, V. Sallet, F. Jomard, A. Lusson, J-F. Rommeluère and Z. Teukam, *J. Appl. Phys.* **91,** 3922 (2002).

32) B. Wyncke and F. Bréhat, *J. Phys. Condens. Matter*, **12**, 3461 (2000).

33) S. Hull, D.A. Keen, *Phys. Rev.* ***B*** **50**, 5868 (1994).

34) C. Schwab and A. Goltzené, *Prog. Crystal Growth Charact*., **5,** 233 (1982)

35) M. Cardona, Phys. Rev., **129,** 69 (1963)

36) R. S. Williams, D. K. Shuh and Y. Segawa, *J. Vac. Sci. Technol.* A, **6,** 1950 (1988).

37) F. O. Lucas, L. O' Reilly, G. Natarajan, P. J. McNally, S. Daniels, D. M. Taylor, S. William, D. C. Cameron, A. L. Bradley, A. Mitra, J. Cryst. Growth, 287, 112 (2006).

38) J. D. Lee, *Concise Inorganic Chemistry*, Chapman and Hall, London (1996).

39) G. Suyal, M. Mennig and H. Schmidt, *J. Mater. Chem.*, **12**, 3136 (2002).

40) http://en.wikipedia.org/wiki/Copper(I)_chloride

41) A. Yanase, Y. Segawa, *Surface Science,* **329**, 219 (1995).

42) . L. Seguin, M. Bendahan, L. L. Seguin, M. Pasquinelli and P. Knauth, *Thin Solid Films*, **32,** 323 (1998).

43) G. Natarajan, S. Daniels, D. c. Cameron, L. O' Reilly, P. J. McNally, O. Lucas, R. T. Rajendra Kumar, I. Reid, A. Mitra and L. Bradley, *J. Appl. Phys.* **100,** 033520 (2006).

44) W. M. Tong, R. S. Williams, A. Yanase, y. Segawa and M. S. Anderson, *phys. Rev. Lett.*, **72**, 3374 (1994).

45) L. O'Reilly, O. F. Lucas, P. J. McNally, A. Reader, G. Natarajan, S. Daniels, D. C. Cameron, A. Mitra, M. M. Rosas and A. L. Bradley, *J. Appl. Phys.* **98**, 113512 (2005).

46) S. Takami, Y. Egashira, I. Honma and H. Komiyama, *Appl. Phys. Lett.* **68,** 1020 (1996).

47) K. Kadono, T. Suetsugu, T. Ohtani, T. Einishi, T. Tarumi and T. Yazawa, *J. Mater. Res.*, **20**, (2005).

48) J. Sasai, K. Tanaka and K. Hirao, *Scripta mater.* **44,** 1225 (2001).

49) K. Tsunetomo *et al.*. Jpn. *J. Appl. Phys*. **30**, 1764 (1991).

50) S. Kono, T. Ishii, T. Sagawa and T. Kobayashi, *Phys. Rev. Lett.* **28**, 1385 (1975).

51) T. Ishii, S. Sato, T. Matsukawa, Y. Sakisaka and T. Sagawa, *J. Phys. Soc. Jap.* **20,** 2054 (1965).

52) K. S. Song, *J. Phys. Chem. Solids* **28**, 2003 (1967).

53) M. A. Khan, *J. Phys. Chem. Solids,* **31**, 2309 (1970).

54) S. Kono, T. Ishii, T. Sagawa and T. Kobayashi, *Phys. Rev. Lett.* **28**, 1385 (1972).

55) M. G. Mason, *Phys. Rev. B,* **11**, 5094 (1975).

56) A. Goldmann, J. Tejeda, N. J. Shevchik and M. Cardona, *Phys. Rev. B.*, **10,** 4388 (1974).

57) A. Goldmann, D. Westphal, *J.phys. C: solid State Phys.* **16**, 1335 (1983).

58) K. Shindo, A. Morita and H. Kamimura, *J. Phys. Soc. Jap.* **20,** 2054 (1965).

59) F. Meseguer , J. C. Merle and M. Cardona, *Solid State Commun.*, **50**, 709 (1984).

60) D. Sanvitto, F. Pulizzi, A. J. Shields, P.C.M. Christianen, S.N.Holmes, M.Y. Simmons, D.A.Ritchie, J.C.Maan and M.Pepper, *Science,* **294,** 837 (2001).

61) A. Goldmann**,** *phys. stat. sol. (b)*, **81**, 9 (1977).

62) A. Gobel, T. Ruf, M. Cardona, C. T. Lin, J. Wrzesinski, M. Steube, K. Reimann, J. C. Merle and M. Joucla, *Phys. Rev. B,* **57**, 15183 (1998).

63) S. Nikitine, *Progress in Semiconductors*, John Weily&Sons, New York (1962).

64) M. Ueta, H. Kanzaki, K. Kobayashi, T. Toyozawa and E. Hanamura, *Excitonic Process in Solids*, Springer-Verlag, Berlin (1986).

65) M. Nakayama, A. Soumura, K. Hamasaki, H. Takeuchi and H. Nishimura, *Phys. Rev. B*, **55**, 10099 (1997).

66) T. Goto, T. Takahashi and M. Ueta, *J. Phys. Soc. Japan,* **24**, 314 (1968).

67) Y. Kaifu and T. Komatsu, *Phys. Stat. Sol. (b)* **48**, K125 (1971).

68) M. Nakayama, H.Ichida and H. Nishimura *J. Phys.: Condens. Matter* **11**, 7653 (1999).

69) Y. Masumoto, S. Okamoto and S. Katayanagi, Phys. Rev. B, **50**, 18658 (1994).

70) G.M. Gale, A. Mysyrowicz, *Phys. Rev. Lett.* **32**, 727 (1973).

71) Y. Kaifu *et al.*, *J. Phys. Soc. Jpn.* **22**, 517 (1967).

72) L. O'Reilly, G. Natarajan, P. J. McNally, D. C Cameron, O. F. Lucas, M. Martinez- Rosas, L. Bradley and A. Reader, *J. mater. Sci. Mater. Electron.* **16**, 415 (2005).

73) Gomathi Natarajan, R. T. Rajendra Kumar, S. Daniels, D. C. Cameron and P. J. McNally, *J. Appl. Phys.* **100**, 096108 (2006).

74) F. O Lucas, A. Mitra, P. J. McNally, S. Daniels, A. L. Bradley, D. M. Taylor, Y. Y. Proskuryakov, K. Durose and D. C. Cameron, *J. Phys. D: Appl. Phys.* **40,** 3461(2007).

75) S. Kondo and T. Saito, *Appl. Phys. Lett.* **90**, 201915 (2007).

76) R. J. Maurer, *J. Chem. Phys.* **13**, 321 (1945).

77) C. Wagner, *J. Chem. Phys.* **18,** 62 (1950).

78) A. V. Joshi and J. B. Wagner, *J. Electrochem. Soc.* **122,** 1071(1975).

79) J. B. Wagner, C. Wagner, *J. Chem. Phys.* **26,** 1597 (1957).

80) J. N. Frers, *Ber. deut. Chem.. Ges.* **60**, 864 (1927).

81) C. Divakar, M. Mohan and A.K. Sigh, *Solid State Commun.* **34**, 385 (1980).

82) P. Knauth, Y. Massiani and P. Pasquinelli, *Phys. Stat. Sol.* **165**, 461 (1998).

83) S. Swann , *Phys. Technol.*, **19,** 67 (1988).

84) P. J. Kelly and R. D. Arnell, *Vacuum*, **56**, 159 (2000).

85) Y. Xiang, W. Chengbiao, L. Yang, Y. Deyang and X. Tingyan, *Plasma Sci. Technol.* **8,** 337 (2006).

86) T. Moiseev, D. C. Cameron, *Surface & Coatings Technology*, **200,** 5306 (2006).

87) R. D. Arnell, P.J. Kelly and J.W. Bradley, *Surface & Coatings Technology,* **188,** 158 (2004).

88) W. Zhou and Z. L. Wang, *Scanning Microscopy for Nanotechnology*, Springer, USA (2007).

89) J. F. Watts, J. Wolstenholme, *An introduction to Surface analysis by XPS and AES ,* Wiley, England (2003).

90) M. Cardona and L. Ley, *Photoemission in Solids,* Springer, Berlin (1978).

91) R. H. Williams, G. P. Srivastava and I.T. McGoverns, *Rep. Prog. Phys.*, **43**, 87 (1980).

92) S. Nakamura, T. Mukai and T. Senoh, *Appl. Phys. Lett.* **64**, 1687 (1994).

93) Y. Ryu, T-S. Lee, J. A. Lubguban, H.W. White, B-J. Kim, Y-S. Park, C- J. Youn, *Appl. Phys. Lett.* **88**, 241108 (2006).

94) J. K. Jeong, J-H. Choi, H. J. Kim, H-C. Seo, H. J. Kim, E. Yoon, C. S. Hwang, H. J. Kim, *J.Cryst.growth* **276,** 407 (2005).

95) T.M.Barnes, K.Olson and C.A.Wolden, *Appl.Phys.Lett.* **86** 112112 (2005).

96) K. Minegishi, Y. Koiwai, Y. Kikuchi, K. Yano, M. Kasuga and A. Shimizu, *Japan. J. Appl. Phys.* **36** L1453 (1997).

97) Y.R. Ryu, T.S.Lee and H.W.White, *Appl.Phys.Lett.* **83,** 87 (2003).

98) M. Bendahan, C.Jacolin, P.Lauque, J- L.Seguin and P.Knauth, *J.Phys.Chem.B* **105,** 8327 (2001).

99) P.Knauth and Y.Massiani, *J.Electroanal.Chem.* **442**, 229 (1998).

100) F.O.Lucas, P.J.McNally, S.Daniels and D.M.Taylor, *J.Mater. Sci: Mater Electro.* **20**, S144 (2009).

101) L.O'Reilly, A.Mitra, G.Natarajan, O.F.Lucas, P.J.McNally, S.Daniels, D.C.Camron, A.L.Bradley and A.Reader, *J.Cryst.Growth* **287,** 139 (2006).

102) R.Schmidt, A.Basu and A.W.Brinkman, J.Eur.Ceram.Soc. **24,** 1233 (2004).

103) S. Kondo, K. Mikami and T. Saito, *Opt. Mater.* **30, 473** (2008).

104) R. S. Bradley, D. C. Munro and P. N. Spencer, *Trans. Faraday. Soc.* **65,** 1912 (1969).

105) R. D. Shannon, *Acta Cryst.*, **A32,** 751 (1976).

106) M. Certier, C.Wecker, S.Nikitine, *J.Phys.Chem.Solids*, **30,** 2135 (1969).

107) N. Garro, A. Cantarero, M. Cardona, T. Ruf, A. Gobel, C. Lin, K. Reimann, K. Rtibenacke and M. Steube, *Solid State Commun.* **98**, 27 (1996).

108) O. Pages, H. Erguig, A. Lazreg, A. Katty, A. Lusson and O.Gorochov, *Mater. Sci.Eng. B*, **69,** 431 (2000).

109) K. H. Kim, K. C. Park and D. Y. Ma, *J. Appl. Phys.*, **81**, 7764 (1997).

110) T. Pisarkiewicz, K. Zakrzewska and E. Leja, *Thin Solid Films*, **174,** 217 (1989).

111) H. Fesefeldt, *Z. Phys.* **67**, 37 (1931).

112) E. G. Schneider and H. M. O'Bryan, *Phys. Rev.* **51**, 293 (1937).

113) W. F. Krolikowski, Ph. D. Thesis, Stanford University, 1967, unpublished.

114) S. Kono,T . Ishii, T. Sagawa and T. kobayashi, *Phys. Rev. B*, **8**, 795 (1973).

115) A. Goldmann, J. Tejeda, N. J. Shevchik and M. Cardona, *Solid State Commun.* **16**, 1093 (1974).

116) T. Ishii, S. Kono, T**.** Matsukawa, T. Sagawa and T. Kobayashi, *J. Electron Spectroscopy*, **5**, 559 (1974).

117) D. E. Eastman, W. D. Grobman, J. L. Freeouf and M. Erbudak, *Phys. Rev. B* **9**, 3473 (1974).

118) D. R. Williams, J. G. Jenkins, R. C. G. Leckey and J. Liesegang, *Phys. Letters A* **49**, 141 (1974).

119) T. Ishi, S. Sato, T. Matsukawa, Y. Sakisaka and T. Sagawa, *J. Phys. Soc. Japan* **32**, 1440 (1972).

120) C. Bonnelle, *J. Phys. (Paris)* **28**, C3-65 (1967).

121) C. Sugiura, *Phys. Rev. B*, **8**, 823 (1973).

122) G. Van der Laan, G. A. Sawatzky, C. Haas and H. W. Myron, *Phys. Rev. B* **20**, 4287 (1979).

123) T. Novakov, *Phys. Rev. B* **3**, 2693 (1971).

124) D. C. Frost, A. Ishitani and C. A. McDowell, *Mol. Phys.* **24**, 861 (1972).

125) T. Takahashi, T. Sato, S. Souma, T. Muranaka and J. Akimitsu, *Phys. Rev. Lett.* **86**, 4915 (2001).

126) K. V. Rajani, F. Olabanji Lucas, S. Daniels, D. Danieluk, A.L. Bradley, A. Cowley, M.M. Alam, P.J. McNally, *Thin Solid Films*, **519**, 6064 (2011).

127) N. J. C. Ingle, R. H. Hammond and M. R. Beasley, J. Appl. Phys., **91**, 6371 (2002).

128) J. C. Klein, D. M. Hercules, *J. Catal.* **82**, 424 (1983).

129) W. Sesselmann and T. J. Chuang, *Surface Science*, **176**, 32 (1986).

130) T. Novakov and Prins, *Solid State Commun.* **9**, 1975 (1971).

131) G. van der Laan, C. Westra, C. Haas and G. A. Sawatzky, *Phys. Rev. B* **23**, 4369 (1981).

132) K. Kishi and S. Ikeda, *J. Phys. Chem.* **78**, 107 (1974).

133) G. K. Wertheim, P. M. Th. M. van Attekum, H. J. Guggenheim and K. E. Clements, *Solid State Commun.*, **33**, 809 (1980).

134) R. P. Vasquez, M. C. Foote and B. D. Hunt, *J. Appl. Phys.* **66**, 4866 (1989).

135) F. Meseguer, J. C. Merle and M. Cardona, *Solid State Commun.* **43**, 511 (1982).

136) S. Villain, M. A. Desvals, G. Clugnet and P. Knauth, *Solid State Ionics*, **83**, 191 (1996).

137) M. A. Desvals and P. Knauth, *J. Phys. Chem. Solids*, **58**, 319 (1997).

138) R. Safadi, I. Riess and H.L. Tuller, *Solid State Ionics*, **57**, 125 (1992).

139) L. Tortet, P. Knauth, H. L. Tuller, *Solid State Ionics*, **146**, 423 (2002).

140) P. Knauth, Y. Massiani, M. Pasquinelli, H.L. Tuller, in: H. Yanagida, H.L. Tuller, (Eds.), *Electrically active ceramic interfaces*, 209 (1998).

141) JCPDS Card No. 06-292, International Centre for Diffraction, New York, (1997).

142) M. Cardona, *J. Phys. Chem. Solids*, **24**, 1543 (1963).

143) S. G. Lee, J. Y. Park, S. M. Lee, S. H. Sohn, *Mol. Cryst. Liq. Cryst.*, **513**, 277 S (2009).

144) C. C. Chen, K. F. Chiu, K. M. Lin, H. C. Lin, C. R. Yang and F. M. Wang, *J. Electrochem. Soc.*, **158**, A262 (2011).

145) S. Kondo, T. Saito and H. Nakagawa, *Phys. Lett. A*, **371,** 332 (2007).

146) T. H. Gfroerer, *Photoluminescence in Analysis of Surfaces and Interfaces*, John Wiley and Sons (2006).

147) V. Yu. Timoshenko, A. B. Petrenko, M. N. Stolyarov, Th. Dittrich, W. Fuessel and J. Rappich, *J. Appl. Phys.*, **85**, 4171 (1999).

148) B. L. Zhu and X. Z. Zhao, *Phys. Stat. Solidi A*, **208**, 91 (2011).

149) K. L. Chopra, P. D. Paulson,y and V. Dutta, Prog. Photovolt: Res. Appl. 12:69 (2004).

150) W. Zhang, Q. Meng, B. Lin, Z. Fu, Solar Energy Materials & Solar Cells, **92,** 949 (2008).

151) M. S. Tomar, Thin Solid Films, **164**, 295 (1988).

152) T. Unold and H.W. Schock, Annu. Rev. Mater. Res., 41:15.1 (2011).

153) T. Okamura, Y. Seki, S. Nagakari and H. Okushi, Jpn. J. Appli. Phys. **31**, L 762 (1992).

154) L. Li, C.X. Shan, B.H. Li, B. Yao, D.Z. Shen, B. Chu, and Y.M. Lu, Journal Of Electronic materials, **39**, 11(2010).

155) Z. W. Ying, Z. Sheng, S. L. Jie, F. Z. Xi, Chin. Phys. Lett., **25,** 1829 (2008).

156) S. Mridha and D. Basak, J. Appl. Phys.**101**, 083102 (2007).

157) H. Kobayashi, Y. Kogetsu, T. Ishida and Nakato, J. Appl. Phys. **74,** 4756 (1993).

158) H. Kobayashi, H. Mori, T. Ishida and Y. Nakato, J. Appl. Phys. **77**, 1301 (1995).

159) T. Minami, T. Miyata, K. Ihara, Y. Minamino, S. Tsukada, Thin Solid Films, **494,** 47 (2006).

160) S. M. Sze, Physics of Semiconductor Materials, second edition, John Wiley & Sons, New York, 819 (1981).

161) D. G. Baik and S. M. Cho, Thin Solid Films **354**, 227 (1999).

162) Y. Hagiwara, T. Nakada and A. Kunioka, Solar Energy Materials & Solar Cells 67 (2001) 267.

163) C. Hu and R. M. White, Solar cells from basic to advanced systems, McGraw- Hill, New York.

164) S. Krauter, Solar Electric Power Generation: Photovoltaic Energy Systems, Springer- Verlag, Berlin, 2006.

165) R. Levinson, P. Berdahl, H. Akbari, W. Miller, I. Joedicke, J. Reilly, Y. Suzuki, M. Vondran, Solar Energy Materials & Solar Cells, **91,** 304 (2007).

166) Z. Guo, D. Zhao, Y. Liu, D. Shen, J. Zhang and B. Li, Appl. Phys. Lett. **93**, 163501 (2008).

167) C. X. Wang, G. W. Yang, H. W. Liu, Y.H. Han, J. F. Luo, C. X. Gao and G. T. Zou, Appl. Phys. Lett., **84**, 2427 (2004).

168) C. T. Sah, R. N. Noyce and W. Shockley, Proc. IRE **45**, 1228 (1957).

169) P. Wang, N. Chen and Z. G. Yin, Appl. Phys. Lett. **88**, 152102 (2006).

170) I. Riedel, J. Parisi, V. Dyakonov, L. Lutsen, D. Vanderzande and J. C. Hummelen, Adv. Funct. Mater. **14**, 38 (2004).

171) F. O. Lucas, L. O'Reilly, G. Natarajan, P. J. McNally, S. Daniels, D. M. Taylor, S. William, D. C. Cameron, A. L. Bradley, A. Miltra, J. Cryst. Growth, **287**, 112 (2006).

172) C. G. Granqvist, *Solar Energy Materials & Solar Cells*, **91**, 1529 (2007).

173) P. P. Deimel, B. B. Heimhofer, G. Krotz, H. J. Lilienhof, J. Wind, G. Muller and E. Voges, *IEEE Photonic Technol. Lett.* **2**, 499 (1990).

174) T. J. Coutts, X. Li, W. Wanlass, K. A. Emery, and T. A. Cessert, *IEEE Electron. Lett.* **26**, 660 (1990).

175) S. Honda, M. Watamori, and K. Oura, *Thin Solid Films,* **281**, 206 (1996).

176) R. H. Bube, A. L. Fahrenbrunch, R. Sinclair, S. Anthony, C. Fortman, C. T. Lee, T. Thorpe, and T. Yamashita, *IEEE Trans. Electron Devices,* **31**, 528 (1989).

177) H. L. Hartnagel, A. L. Dawar, A. K. Jain and C. Jagadish, *Semiconducting Transparent Thin Films,*Institute of Physics, Philadelphia (1995).

178) A. R. Schlatmann, D. W. Floet, A. Hillberer, F. Garten, P. J. M. Smulders, T. M. Klapwijk, and G. Hadziioannou, *Appl. Phys. Lett.* **69**, 1764 (1996).

179) J. C. Scott, J. H. Kaufman, P. J. Brock, R. Dipietro, J. Salem and J. A. Goitia, *J. Appl. Phys.* **79**, 2745 (1996).

180) A. Andersson, N. Johansson, P. Broms, N. Yu, D. Lupo, and W. R. Salaneck, *Adv. Mater.* (Weinheim, Ger.) , **10**, 859 (1999).

181) D. S. Ghosh, L. Martinez, S. Giurgola, P. Vergani, and V. Pruneri, *Optics Letters,* **34**(3), 325 (2009).

182) H. Klauk, J. R. Huang, J. A. Nichols, and T.N. Jackson, *Thin Solid Film,s* **366,** 272 (2000).

183) S. Giurgola, A. Rodrigues, L. Martinez, P. Vergani, F. Lucchi, S. Benchabane and V. Pruneri, *J Mater Sci: Mater Electron,* **20,** S181 (2007).

184) H. Bartzsch, P. Frach, and K. Goedicke, *Surface & Coating Technology,* **132,** 244 (2000).

185) K. Fuchs, *Proc. Cambridge Phil. Soc.* **34**, 100 (1938).

186) E. H. Sondheimer, *Adv. Phys.* **1**, 1 (1952).

187) W. J. Lee, K. Fang, J. J. Ho, C. Y. Chen, S. F. Chen, R. Y. Tsai, D. Huang and F. C. Ho, *J .Mater Sci: Mater Electron* **13,** 751 (2002).

188) S. H. Seo, J. H. In, H. Y. Chang and J. G. Han, *Appl .Phys. Lett.* **86**, 262103 (2005).

189) A. I. Rogozin, M. V. Vinnichenko, A. Kolitsch, and W. Moller, *J. Vac. Sci.Technol* A, **22** (2), 349 (2004).

190) M. S. Hwang, H. J. Lee, H. S. Jeong, Y. W. Seo and S. J. Kwon, *Surface & Coating Technology,* **171**, 29 (2003).